Aero-Thermal-Mechanical Interactions in Ultra High-Speed Micro Gas Turbines

by

Aniwat Tiralap

B.E., Chulalongkorn University (2010)
S.M., Massachusetts Institute of Technology (2015)

Submitted to the Department of Mechanical Engineering
in partial fulfillment of the requirements for the degree of

Doctor of Philosophy

at the

MASSACHUSETTS INSTITUTE OF TECHNOLOGY

February 2020

Signature redacted

Author .....
Department of Mechanical Engineering
January 10, 2020

Signature redacted

Certified by .....
Choon Sooi Tan
Senior Research Engineer, Department of Aeronautics and Astronautics
Thesis Supervisor

Signature redacted

Certified by .....
John G. Brisson
Professor of Mechanical Engineering
Chairman, Thesis Committee

Signature redacted

Accepted by .....
Nicolas G. Hadjiconstantinou
Professor of Mechanical Engineering
Chairman, Department Committee on Graduate Theses

Aero-Thermal-Mechanical Interactions in Ultra High-Speed Micro Gas Turbines

by

Aniwat Tiralap

Submitted to the Department of Mechanical Engineering
on January 10, 2020, in partial fulfillment of the
requirements for the degree of
Doctor of Philosophy

Abstract

Aero-thermal induced mechanical response of engine components in an ultra high-speed micro gas turbine engine system is assessed. Scaling down gas turbine engines for high performance requirement dictates substantial thermal-induced effects on engine operation due to high temperature gradient relative to that in conventional large gas turbine engines. Experiments indicate that the sustainable operation is limited by mechanical response of shaft-bearing housing system. It is hypothesized that this is due to thermal-induced mechanical deformation of shaft-bearing housing that results in bearing clearance variation that differs from the design intent. An unsteady CFD conjugate heat transfer computation of flow and temperature distribution in the engine system is first implemented; this is followed by determining the corresponding mechanical deformation of engine components based on finite element analysis. The computed result shows that at the beginning of the engine start-up process, radial expansion of the shaft is larger than that of the bearing housing, resulting in a smaller bearing clearance. Toward steady-state operation, a larger bearing clearance is observed. The computed results and experimental observation are in agreement thus confirming the hypothesis. The key controlling non-dimensional parameters characterizing the aerothermal-mechanical interaction and response are identified using a reduced order model that yields thermal-induced mechanical deformation in agreement with the unsteady computations. For geometrically similar engine system, the controlling thermal and structural parameters consist of: (1) shaft fin parameter, (2) housing fin parameter, (3) ratio of heat diffusivity of housing to that of shaft, (4) 3 cooling flow parameters, and (5) ratio of coefficient of thermal expansion of the housing to that of shaft. The non-dimensional parameters serve as a guideline for developing strategies for controlling bearing clearance under the acceptable margin, including selecting shaft and housing materials with appropriate properties as well as tailoring the cooling flow. An approximate scaling rule for thermal-induced shaft-bearing housing clearance variation in engine of various sizing is formulated.

Thesis Supervisor: Choon Sooi Tan
Title: Senior Research Engineer, Department of Aeronautics and Astronautics

Acknowledgments

First of all, I would like to express my deep gratitude to my advisor, Dr. Choon Tan, for believing in me. His guidance and support throughout the PhD journey has provided me confidence to deal with numerous challenges over years of the research. It has been a great pleasure to work with him and this work would not be possible without his support. I would like to also thank Dr. Kousuke Isomura for sponsoring the research program, which provides me the opportunity to work with real-world challenges. His expertise in micro gas turbine development brings in insightful perspectives. Discussions with him have broaden my horizon.

Furthermore, I am indebted to my thesis committee. Professor John Brisson, chairman of the committee, always brings interesting questions, and provides different perspectives and constructive feedback on my work. I would like to thank Professor John Hart for his expertise in additive manufacturing. I would like to thank Dr. Tian Tian and Professor Wai Cheng for attending my thesis defense.

I am grateful to Professor Kripa Varanasi, Professor Wai Cheng, Professor Anthony Patera, Professor Jacopo Buongiorno, Professor Irmgard Bischofberger, and Professor Asegun Henry for giving me the opportunity to be a teaching assistant. Sharing my passion for thermofluids with other students has brought joy into my life. I appreciate financial support during the last summer semester from Professor Evelyn Wang, Mechanical Engineering Department Head. I would like thank Leslie Regan and Una Sheehan for keeping things running smoothly and sorting out various unanticipated issues.

I was fortunate to be surrounded by outstanding labmates at the Gas Turbine Laboratory, who have provided me great support and made time at MIT unique and enjoyable experience. I would like to especially thank Jinwook Lee, Laurens Voet, and Thomas Hubschman for their friendship and countless entertaining discussions. I would like to thank many friends at MIT for their warm friendship throughout my studies here, especially for those from TSMIT. Last but not least, I am totally indebted to my family for their constant love and support, motivating me through

endless obstacles toward my goal. This achievement is as much yours as it is mine.

This research has been supported by IHI under contract "Agrmt Dated January 11, 2016".

Nomenclature

A = Area

B = Thickness

c = Specific heat capacity

Fo = Fourier number (non-dimensional time)

k = Thermal conductivity

h = Heat transfer coefficient

L = Length

P = Perimeter

r = Radial location

R = Radius

t = Time

T = Temperature

u = Structural deformation

x = Axial location

α = Coefficient of thermal expansion

κ = Thermal diffusivity

ρ = Density

θ = Non-dimensional temperature

υ = Poisson's ratio

$\mathcal{R}$ = Non-dimensional radial location

χ = Non-dimensional axial location

Subscripts

i = Initial

in = Inner

eff = Effective

TIT = Turbine inlet temperature

h = Housing

out = Outer

r = Radial

s = Shaft

x = X-direction

y = Y-direction

z = Z-direction

∞ = Cooling flow

Supercripts

$(\dot{})$ = per unit time

Abbreviation

CFD = Computational fluid dynamics

CHT = Conjugate heat transfer

CTE = Coefficient of thermal expansion

FE = Finite element

ROM = Reduced order model

SAS = Secondary air system

URANS = Unsteady Reynolds-averaged Navier-Stokes

Contents

List of Figures

List of Tables

Chapter 1

Introduction and Research Questions

1.1 Background

Gas turbines are used in a wide variety of applications, including aircraft propulsion, power generation, etc. As there are numerous applications of gas turbines, the power output of gas turbines varies significantly. On one end of the spectrum, land-based industrial gas turbines for power generation can have power output as large as 519 MW and larger [5]. Gas turbines used in powering commercial aircraft can produce power output in the order of 10-100 MW. On the other end of the spectrum, micro gas turbines, which provide much smaller output, have recently received more attention.

Micro gas turbines can be utilized in applications that require a portable power generation source such as robots and UAVs. Designs of micro gas turbines can be tailored to serve a wide range of performance metrics such as compactness, efficiency, energy density, power density, system operating costs, and robustness. For example, in power generation application, micro gas turbines can offer higher energy density output than batteries do [6]. For propulsion application, micro gas turbines can offer robustness and require less maintenance than internal combustion engines [7]. Although micro gas turbines are considered more portable, their size still varies greatly

with applications. Currently, micro gas turbines for power generation are available in the market with power output in the range of 30-330 kW [8, 9]. There are attempts by numerous groups of engineers and researchers to design and develop micro gas turbines with the power output in the order of 1-10 kW [7, 10–15]. The most notable one is the button-shirt size micro gas turbine developed during the 2000s at the Gas Turbine Laboratory, MIT [6]; however, the program ended before a fully integrated engine could be demonstrated to be fully functional.

In general, micro gas turbines in the power range of 10 kW and smaller tend to have a single-stage centrifugal compressor and radial inflow turbine [6, 7, 10–13, 15, 16]. The radial turbomachines offer high-pressure ratio at small mass flow rate with a compact engine size. The pressure ratio range is usually set to be between 2 and 4. The small engine size introduces new technical challenges. Heat flux, which scales with temperature difference and the inverse of length scale, becomes higher due to the smaller size of the engine, given a similar temperature difference in the engine. The change in the length scale affects the Biot number (Bi), which is a ratio of internal thermal resistance and external thermal resistance. For the engine structures, the internal thermal resistance is the resistance of conduction heat transfer and the external thermal resistance is the resistance of convection heat transfer.

It can be inferred that Biot number of small engines is smaller than that of large engines based on similar heat transfer coefficient and thermal conductivity. For small Biot number, the internal thermal resistance is smaller and conduction heat transfer becomes more important relative to convection heat transfer. As such, conduction heat transfer in small engines is not negligible. It has been shown by Sirakov et al. that heat transfer between the turbomachines results in performance reduction of the compressor and the turbine [17]. An adiabatic assumption usually employed in a large gas turbine design is no longer applicable in this case and micro gas turbines should be designed to accommodate consequences of this additional heat transfer effect.

In addition, because the diameter of the turbomachines is significantly smaller (relative to that in large conventional gas turbines), the rotational speed of the engine has to be increased proportionally to achieve a high rotor tip velocity similar to that

in large gas turbines. For example, at ONERA, a micro gas turbine was developed to provide power output of 50 – 100 Watts [16]. The nominal speed is 840,000 rpm. In Belgium, Piers et al. developed micro gas turbines with power output of approximately 1 kW at the rotational speed of 500,000 rpm [10]. In Korea, Seo et al. developed a 500W micro gas turbine with the rotational speed of 400,000 rpm [11].

The high rotational speed entails a set of distinctly different bearing design requirements. The design of the shaft has to ensure that the bearing is able to keep the shaft in the stable operating range. At high speed, gas bearings are more suitable than ball bearings because gas bearings allow high speed operation with low friction. Gas foil bearings are used in micro gas turbines as gas foil bearings provide improved damping and stability characteristics compared to those of rigid gas bearings [18]. In addition, gas foil bearings do not require additional lubrication system hence reducing the overall system size, and maintenance required for the gas bearing is relatively lower.

Additional challenges in developing micro gas turbines arise because of the use of gas foil bearings in micro gas turbines to accommodate the compact engine size and the high engine speed. Operation of bearings must be carefully controlled to be within its operating envelope. The bearing clearance size must be controlled to avoid operability issue. This bearing clearance change can be driven by differential expansion between the rotor and the bearing housing due to mechanical and thermal expansion. Radil et al. showed that when the bearing clearance size of a foil bearing is smaller than the optimum value, the bearing has a higher risk of thermal runaway and bearing seizure. On the other hand, when the bearing clearance size is larger than the optimum value, the bearing has lower stiffness and lower damping coefficients [19]. The lower stiffness and lower damping coefficients can introduce whirl instabilities during the operation.

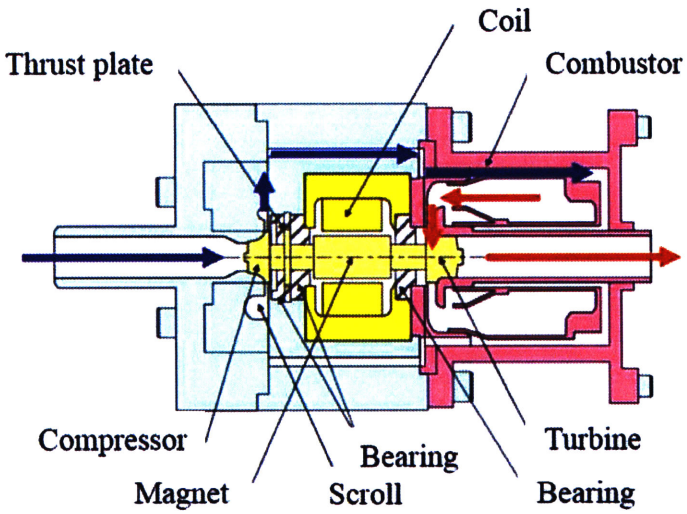

Figure 1-1: Schematic structure of a generic micro gas turbine (adapted from [1]). This generic micro gas turbine has a single shaft with a single-stage centrifugal compressor and a single-stage radial-inflow turbine on the shaft ends.

1.2 Challenges in Development of Micro Gas Turbines

A representative micro gas turbine engine has been designed and constructed for research and development. The schematic layout of the engine configuration is shown in Figure 1-1. The engine has a single shaft with a centrifugal compressor and a radial inflow turbine mounted on the shaft. This configuration is similar to that of several micro gas turbines [6,7,10,13,15,16]. The current configuration is designed to have a generator magnet at the center of the shaft between the compressor and the turbine. The current thermal management system is able to keep the magnet temperature below the Curie temperature. Key unique features of this engine include its high energy density and power density due to its light weight. A bearing configuration that could sustain rotational speed up to 770,000 rpm has been designed, built and integrated into the engine [20]. However, occasional shaft-bearing operability issue has been detected in the current engine. The engine occasionally exhibited whirl instabilities at high-speed operation when the bearing clearance size is set to be relatively large for avoiding the thermal runaway and bearing seizure during the

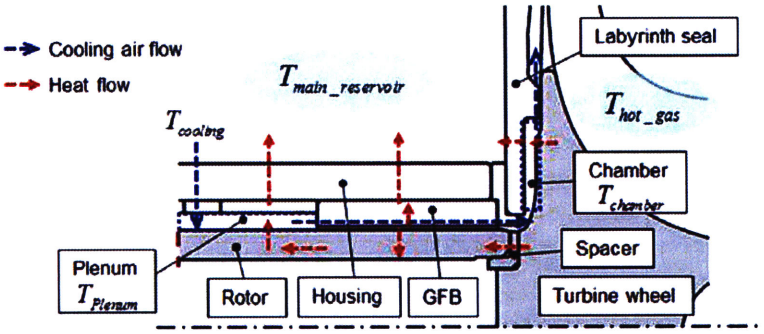

Figure 1-2: Spatial scope of thermal system analysis carried out by Lee et al. [2] . Heat transfer from the turbine rotor to the compressor was not included in the analysis. Heat transfer flow and cooling air flow inside the analyzed section are shown by red and blue arrows, respectively.

start-up process. On the other hand, when the bearing clearance is set to be relatively tight for avoiding whirl instabilities at high speed operation, the thermal runaway and bearing seizure occur during the start-up process.

The cause of the operability issue was hypothesized to be from thermal expansion mismatch between the shaft and the bearing during engine acceleration. This operability issue associated to shaft-bearing system introduces another challenge for micro gas turbine design. It is anticipated that other ultra high-speed micro gas turbines with a compact single-shaft configuration could encounter the same issue as well. Although the severity of the issue is likely to be a function of the engine size, there are, at this stage, no obvious controlling parameters that can be utilized to indicate if the issue is present in any given engine. In order to rectify the operability issue in the representative engine, an adequate thermal management of both the secondary air system (SAS) and thermal flow needs to be devised for the representative engine.

The availability of a thermal management system design is rather limited in the open literature; the literature on the design process of micro gas turbines has the usual focus on the aerodynamic performance of compressor and turbine, combustion characteristics, and bearing designs. One study is from Lee et al., who showed a thermal management design for a micro gas turbine rig with power output of 120 kW and the maximum rotational speed of 47,500 rpm [2]. Their thermal management system utilized compressed air from the compressor outlet to cool a gas foil bearing

(GFB) close to the turbine. Their analysis on the thermal management design was carried out to determine the steady-state temperature variation of the cooling flow near the gas foil bearing on the turbine side. Figure 1-2 shows the spatial scope of their analysis, which covers the right end of the rotor up to the solid turbine blade. Heat transfer from the turbine rotor to the compressor was not included in the analysis. The boundary conditions on the turbine blade used in their calculations were provided from experiments. No thermal behavior or instabilities were observed over the operating range. However, it should be noted that the representative engine, which has the power output approximately 2 orders of magnitude smaller than that of the engine studied by Lee et al., would be more likely to encounter operational challenges from relatively larger heat transfer effects.

Another tool for analyzing a thermal management system of a micro gas turbine was developed by Tanaka et al. [21]. They developed a thermal resistance network analysis mainly to support the development of the representative micro gas turbine. The model provided an estimation of the steady-state temperature distribution throughout the engine, including where temperature measurement could not be made. The model also ensured that the generator magnet temperature was controlled under the limit. This resistance network model was developed in MATLAB and it was capable of solving conduction heat transfer in solid and convection heat transfer at solid-fluid interfaces with use of empirical correlations. Because the number of nodes used in the model was in the order of 100 nodes, the model promptly provided numerical results with minimal demand on computational resources. The thermal resistance network model was successful in assisting the design process, which required short assessment cycles; however, transient thermal behavior and structural response aspects of the engine have not been included in the model. The bearing clearance variation during the engine start-up process cannot be quantified because of the lack of transient thermal-structural behavior.

In order to address and solve the operability issue in the representative micro turbine, there is a need to obtain quantitative data on how the current engine operates. Measurement data from experiments should provide the insight on how the engine

behaves and how heat transfer affects the operation of the engine; however, the small size of the engine allows measurement devices to be installed in a limited number of locations. The data is thus of low resolution and can neither clearly elucidate the operability issue of the engine nor provide quantitative data to assess the hypothesized causes (the radial expansion mismatch between the shaft and the bearing housing).

There is thus a need to formulate an integrated thermal-fluid-structural computational approach that is capable of quantifying engine operating characteristics based on engine design and engine operating conditions. This computational approach is proposed to enable an engineering resolution to the operability issue in the representative micro gas turbine, ensuring the robust operation of the engine.

In summary, investigation of the operability issue appears to be challenging from experiments primarily due to limitation in measurements. As such, computational approaches are proposed for providing the cooling flow field and the operation of the engine. A suitable thermal-fluid computational approach needs to be formulated and discussions on the selection are provided.

1.3 Research Questions

The key goal of the research is to quantify aero-thermal-mechanical interactions of micro gas turbines as the interactions impact mechanical integrity of the shaft-bearing housing system and hence robust operation of the gas foil bearings. The starting point of the research is the operability issue encountered in the current micro gas turbine engine. The insights into the underlying mechanisms of the issue would serve as a foundation to formulate a solution to undesirable thermal-mechanical interactions causing the operability issue.

The research questions that need to be addressed for accomplishing the goal of the thesis are delineated as follows.

1. What constitutes an adequate research tool that is capable of characterizing the operation of the thermal management system and the thermal-mechanical mismatch issue and of the representative engine?

2. Does the hypothesized thermal-mechanical mismatch, which limits robust operation of the representative engine, occur in the engine?

3. How should a reduced order model be constructed to provide insights into flow/thermal processes that are responsible for the current thermal-mechanical mismatch and to serve as an approximate model during the design process?

4. What are essential non-dimensional parameters controlling structural response in micro gas turbine engines of different size?

5. What are technically viable solutions to the operability issue with a minimal engine redesign and minimal impact on engine performance?

1.4 Contributions

1. The hypothesis that thermal-induced mechanical deformation of shaft-bearing housing system limits sustainable operation of the representative micro gas turbine engine is proven. An unsteady CFD conjugate heat transfer computation of flow and temperature distribution in the entire engine system is first implemented for engine startup to steady state operation; this is then followed by determining the corresponding mechanical deformation of engine components based on finite element analysis. The computed result demonstrates the temporal evolution of the thermal expansion mismatch between the shaft and the bearing housing from the start-up toward the steady-state condition. At the beginning of the engine start-up process, radial expansion of the shaft is larger than that of the bearing housing at any axial location, resulting in a smaller shaft-bearing housing clearance at any axial location. At the end of the start-up process, the computed trend (in radial expansion of shaft and bearing housing) reverses so that there is an increase in the clearance. These bearing clearance changes can result in thermal rubbing and rotordynamic issues, respectively.

2. The governing non-dimensional parameters are categorized in 7 groups: (1) 3 non-dimensional temperatures, (2) 2 non-dimensional structural thermal expansions,

(3) 2 non-dimensional location parameters, (4) 1 non-dimensional time parameter, (5) 9 non-dimensional geometric parameters, (6) 6 non-dimensional thermal parameters, and (7) 1 non-dimensional structural parameter. The non-dimensional thermal parameters consist of: (1) shaft fin parameter, (2) housing fin parameter, (3) ratio of heat diffusivity of housing to that of shaft, (4) ratio of energy storage in cooling flow to that in shaft, (5) ratio of advection in fluid to heat diffusion in shaft, (6) ratio of heat conduction in housing to that in shaft. The only controlling structural parameter is the ratio of coefficient of thermal expansion of the housing to that of the shaft. The non-dimensional parameters serve as a guideline for selecting shaft and bearing housing materials with appropriate properties as well as tailoring the coolant flow to limit and control the variation in the bearing clearance during the transient process and the steady-state condition.

3. A reduced order model consisting of conduction heat transfer and convection heat transfer as set by the solid structures and cooling flow is formulated. Reduced-order model results are in accord with transient results from the CFD and FE model. The reduced order framework as well as its use for identifying characterizing parameters and formulation of scaling rule can be generalized for assessing thermal-induced mechanical response of other engine components such as turbomachinery tip clearances and mechanical seal system. The reduced order model provides an enabler to determine the critical Fourier number (i.e. the time instant) for the occurrence of minimum bearing clearance and the bound on clearance variation. This leads to a potential mean to develop a strategy for controlling bearing clearance under the bearing operating envelope. In addition, the reduced order model is used to formulate an approximate scaling rule of thermal-induced shaft-bearing housing clearance variation in engine of various sizing.

4. A first of a kind of computational model consisting of use of 3D URANS coupled with conjugate heat transfer and finite element method has been formulated to

determine: (1) fluid flow and heat flow in the entire engine system from the engine start-up to the steady-state operation and (2) the corresponding engine component mechanical response that include structural deformation and stress distribution.

1.5 Thesis Organization

Chapter 2 outlines the research scope and the key assumptions utilized in the research. Use of 3D conjugate heat transfer CFD and finite element tools is discussed. The computational domain of the representative micro gas turbine engine is illustrated. In Chapter 3, fluid-thermal flow processes in the representative engine are assessed for their impact on mechanical-structural deformation. Fluid-thermal flow processes responsible for elevated temperature of the turbine bearing housing are identified. The change in the bearing clearance size of the foil bearing during a steady-state operation is quantified. Chapter 4 investigates the elevated temperature of the turbine bearing housing and the temporal variation of the bearing clearance during the engine start-up process. Chapter 5 formulates a reduced order model to capture essential heat transfer processes governing the thermal expansion mismatch. Non-dimensional parameters governing the expansion mismatch issue are provided. A scaling rule of the thermal expansion mismatch is derived for a simplified case. Chapter 6 utilizes the non-dimensional parameters and the reduced order model as a basis for proposing solutions to the thermal expansion mismatch issue. Proposed solutions include the use of materials with different thermal diffusivity and coefficient of thermal expansion. Discussions are provided for selecting suitable thermal properties of a candidate material. Finally, all key findings are summarized and future work is proposed in Chapter 7.

Chapter 2

Research Approach

This chapter presents the framework of approach for addressing the research questions and for assessing the hypothesis posed in Chapter 1. This chapter provides discussions on the research scope and selection of several computational models implemented for the research. Specifically, the key goal is to quantify the differential expansion mismatch in the engine-shaft bearing housing configuration that is hypothesized to determine the engine operability and sustainable operation (see Chapter 1). The research scope and several key assumptions are first delineated. Computations of the fluid and thermal flow field as well as the attending structural-mechanical response in the representative engine are obtained. The use of CFD and the structural model constitutes an adequate technical tool to assess the hypothesis.

2.1 Research Scope

Literature review in Chapter 1 shows that there has been substantial research on operation of foil bearings but there is limited work done on thermal management system of micro gas turbines. For this reason, this thesis will focus on the engine level to analyze characteristics of the thermal management system instead of focusing at operation of foil bearings with boundary conditions provided from the engine operations.

The main focus of the research is controlling changes in the bearing clearance within its operating envelope, which is provided by the bearing manufacturer. The bearing clearance change is caused by the differential expansion between the stationary and rotating components. Proposed solutions to the differential expansion are formulated around controlling fluid-thermal interactions through use of the thermal management system. In other words, this thesis focuses on setting an environment in which foil bearings can operate under their operational requirement.

The effect of bearing operation on engine stability is not considered (i.e. rotordynamics is beyond the scope of this thesis); with this assumption/approximation, foil bearings are not physically included in the model and the following assumptions will be utilized in the research:

1. Foil bearings do not affect the thermal-fluid flow on the engine level.
2. Structural deformation of the foil bearing (top foil and bump foil) itself is negligible.
3. Structural deformation has negligible impacts on fluid and thermal flow field.

Based on these assumptions, the actual bearing clearance size is not calculated in this thesis; a change in the bearing clearance is inferred from the difference in expansion of the bearing housing and the shaft instead of a small clearance between the bearing top foil and the shaft. However, the bearing clearance size can be estimated from a measured bearing clearance from experiments and a bearing clearance change provided by the computational model.

The thesis starts with characterization of fluid-thermal interactions in the engine based on the current thermal management system. Assessment of thermal-induced behavior of structural components follows based on the temperature distribution of the engine. Based on the lesson learns, a reduced order model will be formulated for developing solutions to the differential expansion mismatch issue and assessing issues in engines with different sizes. These computational models utilized in different stages of the research are described in the following sections.

Table 2.1: Operating conditions utilized in CFD calculations

Parameters	Value
Operating speed	190,000 RPM
Turbine inlet temperature	800 °C
Total pressure loss in combustor	7%
Ambient pressure and temperature	Ambient conditions at sea level

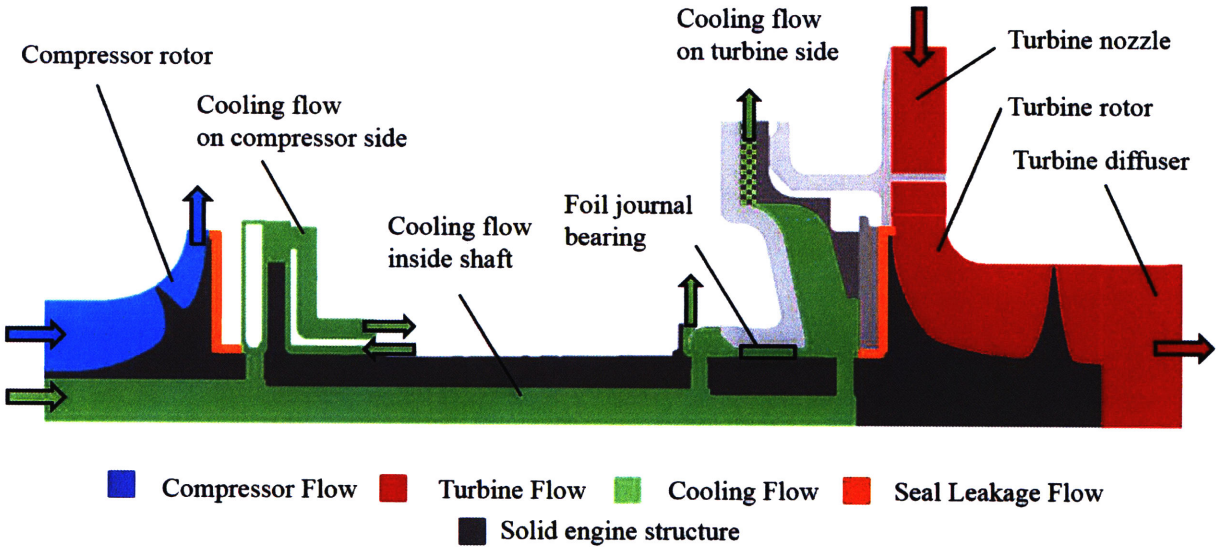

Figure 2-1: Overall computational domain. The main gas flow path includes flow in compressor rotor, turbine nozzle, turbine rotor, and downstream turbine diffuser. The secondary flow path includes flow inside the shaft, cooling chambers, and leakage flow through seals. The secondary flow path acts as a thermal management system to keep temperature of the engine under a limit.

2.2 Computational Domain for Representative Micro Gas Turbine Engine

The representative engine has a single shaft with a single-stage centrifugal compressor and radial inflow turbine. The rated power output is in order of 1 kW and the maximum rotating speed is 250,000 RPM. The engine has a secondary air system for cooling the generator and the foil bearings, and minimizing heat transfer into the compressor. Operating conditions used in CFD calculations are listed in Table 2.1.

A computational domain for CFD is constructed to capture key heat transfer

Table 2.2: Thermal and structural properties of engine structures of the representative engine

Parameters	Value
Ratio of thermal conductivity of shaft and stationary structures	0.7
Ratio of thermal diffusivity of shaft and stationary structures	0.7
Ratio of coefficient of thermal expansion of shaft and stationary structures	0.7

paths from the hot section of the engine to the cold section. The heat transfer paths include the shaft, bearing housing, and turbine nozzle. The overall computational domain is shown in Figure 2-1. The main gas flow path includes flow in compressor rotor, turbine rotor, turbine rotor, and downstream turbine diffuser. The secondary flow path includes flow inside the shaft, cooling chambers, and leakage flow through seals. The location of a foil journal bearing on the engine hot side is shown in Figure 2-1. It should be noted that another foil journal bearing and two additional thrust bearings are not shown in the figure. The material of the shaft is different from that of the stationary components (e.g. bearing housing, turbine nozzle). Table 2.2 shows thermal and structural properties of the engine structures, which control the thermal-structural characteristics of the engine.

The computational domain is separated into two parts to handle different flow timescales. The primary computational domain consists of fluid and thermal flow field in the compressor, cooling flow, turbine, and engine structures. The secondary computational domain consists of compressor leakage flow and turbine leakage, which escape the main flow path and enter the cooling flow path. The primary and secondary computational domains are iteratively coupled to obtain consistent boundary conditions between the two domains in steady-state CFD calculations. Inlet and outlet boundary conditions for the overall CFD domain are shown in Figure 2-2. The inlet boundary conditions of the compressor and the cooling flow is ambient conditions at the sea level. The outlet boundary conditions of the compressor is related to the inlet boundary conditions of the turbine through the pressure drop constraint. The outlet of the cooling flow path and the turbine is also the ambient conditions at the sea level.

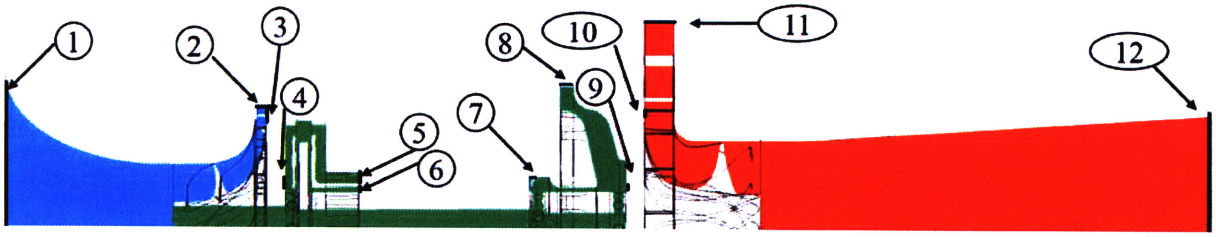

Compressor
Cooling flow
Turbine

1	Compressor inlet	7	Cooling flow outlet 2
2	Compressor rotor outlet	8	Cooling flow outlet 3
3	Compressor seal flow inlet	9	Turbine seal flow outlet
4	Compressor seal flow outlet	10	Turbine seal flow inlet
5	Cooling flow outlet 1	11	Turbine nozzle inlet
6	Cooling flow inlet 1	12	Turbine diffuser outlet

Figure 2-2: Boundaries of the primary CFD domain. The inlet boundary conditions of the compressor flow and the cooling flow are the ambient conditions at the sea level. The outlet boundary condition of the cooling flow and the turbine flow is pressure at the ambient conditions. The outlet boundary conditions of the compressor flow and the inlet boundary conditions of the turbine flow are coupled through pressure drop in the combustor. The inlet and outlet boundary conditions of the seal leakage flow are obtained from the secondary CFD domain.

2.3 Fluid-Thermal Computational Model

Three-dimensional URANS CFD with a conjugate heat transfer (CHT) module has been proposed as the main thermal-fluid computational tool in lieu of the thermal resistance network developed by Tanaka et al. [21]. An advantage of using CFD is that behavior of a cooling flow, including detailed distribution of mass flow rate, temperature, and pressure, can be resolved in the computational domain from known boundary conditions. A resistance network model that is capable of doing the same task would require correlations that are generally unavailable or might need to be obtained from experiments. The use of CFD would reduce the uncertainties associated with using empirical correlations based on experimental data unrelated to relatively small engine scale.

A requirement of utilizing CFD as the main research tool is the need for large computational resources. Obtaining high-fidelity computational results unavoidably requires a large number of computational nodes in the model. However, the required

computational time and resources can be adjusted to satisfy the required accuracy during different phases of the research without substantial recoding the modeling tool. As a micro gas turbine generally has a single stage compressor and turbine (in contrast to a multistage compressor and turbine in large gas turbines), the computational requirements for a micro gas turbine are thus smaller and the flow field in the engine can be solved with manageable computational resources.

ANSYS CFX, which is a commercial 3D finite-volume solver, is selected as the CFD solver for fluid flow in the engine system. CFD solvers with a CHT capability have been successfully utilized by a number of researchers in analyzing steady-state and transient behavior of a SAS of gas turbines [22–26]. Assessments of computed results against experimental data have shown the adequacy and utility of the tool. Effects of mesh resolution and turbulence modeling have been quantified and the best practice has been developed for implementing the computational aspects of flow through the engine (primary and secondary) flow paths.

2.4 Thermal-Structural Computational Model

As the operability issue is hypothesized to be the result of a change in the bearing clearance size, there is a need to quantify the bearing clearance size change from the operation. There are several numerical approaches to compute the bearing clearance. On the high-fidelity end, a two-way coupling CFD and finite element (FE) solver could be implemented to compute the flow field of the fluid, the stress and strain distribution in the solid components. This approach inevitably requires high computational resources but it elucidates interactions between changes in the geometry of the components and the fluid flow field. An example of an interaction between the fluid flow field and the structural response is that if the bearing clearance size is vanishingly small during operation, the model would predict large local heat generation at the bearing, which results in further expansion of the shaft and a decrease of bearing clearance. This example appears to be an extreme and unlikely situation during normal operation.

The thermal-structural model used in this research is a one-way coupled model of 3D CFD and a 3D finite element solver to assess the fluid-structural interactions. The utilized structural model does not account for impacts of change in the geometry of the components on the fluid flow field. It is assumed that under a proper thermal management system, changes in the component geometry should not affect the operation of the engine and the fluid flow field. The structural aspect of the engine and its implication on the thermal expansion mismatch will be analyzed based on a structural model supported by data from CFD computations. The use of CFD and the structural model thus constitute an adequate technical tool to assess the hypothesis.

The chosen 3D finite element solver is ANSYS Mechanical. The temperature field obtained from CFD results is then imported to the FE solver to determine the change in the engine structure, hence the associated change in shaft-bearing clearance size distribution. Discrepancy can be assessed and additional computations can be performed if necessary with the newly computed engine shaft-bearing clearance size. Thus, computed results from the FE solver that include distribution of stress and deformation, should enable analyzing and assessing the engine operability issue and also future design iterations of the engine.

2.5 Reduced Order Model for Sensitivity and Scaling Analysis

A reduced order model is to be formulated and developed using quantitative insights obtained from the CFD and FE results. The reduced order model should capture key physics governing the transient operation of the thermal management system and the engine. With its low computational cost, the reduced order model can also be utilized for trade-off studies for assessing thermal management system design and development. The reduced order models are useful during a preliminary engine design in which several parameters need to be determined. The model also offers opportunities to design a new engine at a different scale based on the previous engine

with a similar geometry.

Results from trade-off assessments based on the reduced order model are particularly useful for exploration of a design space. In other words, the results can suggest which flow processes and engine components need to be altered or re-designed. The design space for the thermal management system could be broadened further with the emerging 3D printing technology as it would allow fabrication of fluid and thermal flow paths not achievable by conventional manufacturing techniques; smaller and complicated flow paths could result in higher heat transfer coefficients and desired structural characteristics.

2.6 Summary

Investigation of the potential cause of the operability issue and the bearing clearance change appears to be challenging from experiments primarily due to limitation in measurements. As such, computational approaches are proposed as the main tool for providing the cooling flow field and the operation of the engine. The main focus of the research is controlling the bearing clearance variation under the operating envelop of the bearing. Controlling the bearing clearance variation, which is caused by the differential expansion between the stationary and rotating components, is achieved through a proper thermal management system. In other words, this thesis focuses on setting an environment in which foil bearings can operate under their operation requirement. With this high level approach, foil bearings are not physically included in the model. As a result, a change in the bearing clearance is inferred from the difference in expansion of the bearing housing and the shaft instead of the actual small clearance between the bearing top foil and the shaft.

The representative micro gas turbine engine has a single shaft with a single stage centrifugal compressor and radial inflow turbine. These characteristics are shared with many micro gas turbines under development. The representative engine has the rated power output in order of 1 kW and the maximum rotating speed of 250,000 RPM. The engine has a secondary air system for cooling the generator and foil bearings,

and minimizing heat transfer into the compressor.

Three-dimensional URANS with a conjugate heat transfer (CHT) module has been proposed as the main thermal-fluid computational tool. The use of CFD would minimize the uncertainties associated with using empirical correlations based on experimental data unrelated to relatively small engine scale.

The thermal-structural model used in this research is a one-way couple model of 3D CFD and a 3D finite element solver. The utilized structural model does not account for impacts of change in the geometry of the components on the fluid flow field. The structural aspect of the engine and its implication on the thermal expansion mismatch will be analyzed based on a structural model supported by data from CFD computations. The use of CFD and the structural model thus constitute an adequate technical tool to assess the hypothesis.

A reduced order models is to be formulated and developed using quantitative insights obtained from the CFD results. The reduced order model should capture key physics governing the operation of the thermal management system and the engine. With its low computational cost, the reduced order model can also be utilized for trade-off studies, assessing thermal management system design and development, and exploration of a design space.

Chapter 3

Differential Expansion in Shaft-Bearing Housing Clearance under Steady-State Operation

In this chapter, fluid-thermal flow processes in the representative engine are assessed for their impact on mechanical-structural deformation/response. Specifically, the results from the computational framework elaborated in Chapter 2 are post processed and interrogated to: (1) identify the specific fluid-thermal flow processes responsible for elevated temperature of the turbine bearing housing that give rise to changes in shaft-bearing housing system; and (2) quantify the change in the bearing clearance size of the foil bearing during steady-state operation.

3.1 Governing Thermal-Fluid Processes during Steady-State Operation

As previously mentioned in Chapter 1, for micro gas turbines, heat flux between the turbine and the compressor is anticipated to increase as the scale of the engine reduces. The thermal management system is utilized to prevent excessive heat transfer from the

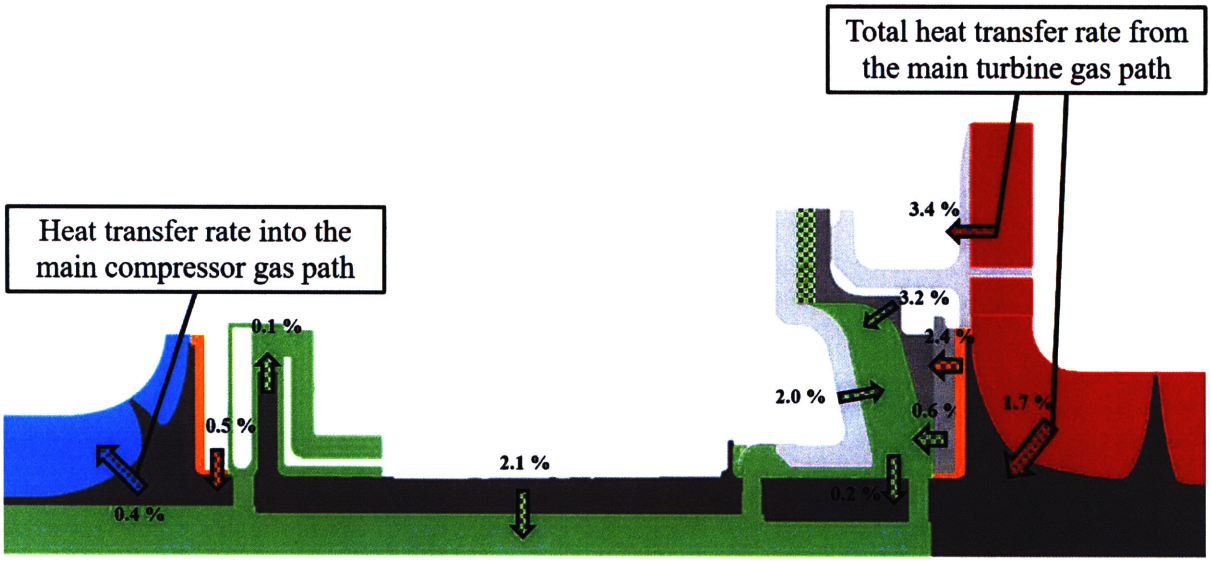

Figure 3-1: Convection heat transfer distribution in the representative engine. Convection heat transfer rate is normalized relative to the turbine power output. 67% of the total heat transfer rate is through the turbine nozzle and 33% of the total heat transfer rate is through the turbine rotor. Compressor operation is practically adiabatic due to negligible heat transfer into the compressor.

hot section toward the compressor and to maintain temperature within an acceptable margin. Steady 3D CFD with a CHT module is used to carry out calculations to assess the performance of the thermal management system and identify the heat transfer paths in the engine.

3.1.1 Engine Temperature and Heat Flux Distribution

CFD calculations are carried out to determine heat transfer distribution in response to the boundary conditions delineated in Chapter 2. Figure 3-1 shows the magnitude and the direction of convection heat transfer between different sections of the engine. The convection heat transfer at various locations is normalized respective to the turbine power output. Heat transfer through the turbine nozzle accounts for 67 % of the total heat transfer from the turbine; this results in a small drop of total temperature across the turbine nozzle ($T_{0,\text{outlet}}/T_{0,\text{inlet}} \approx 0.994$). Heat transfer through the shaft accounts for the remaining 33 %. It can be seen that the direction of heat transfer is toward the cold section of the engine as anticipated.

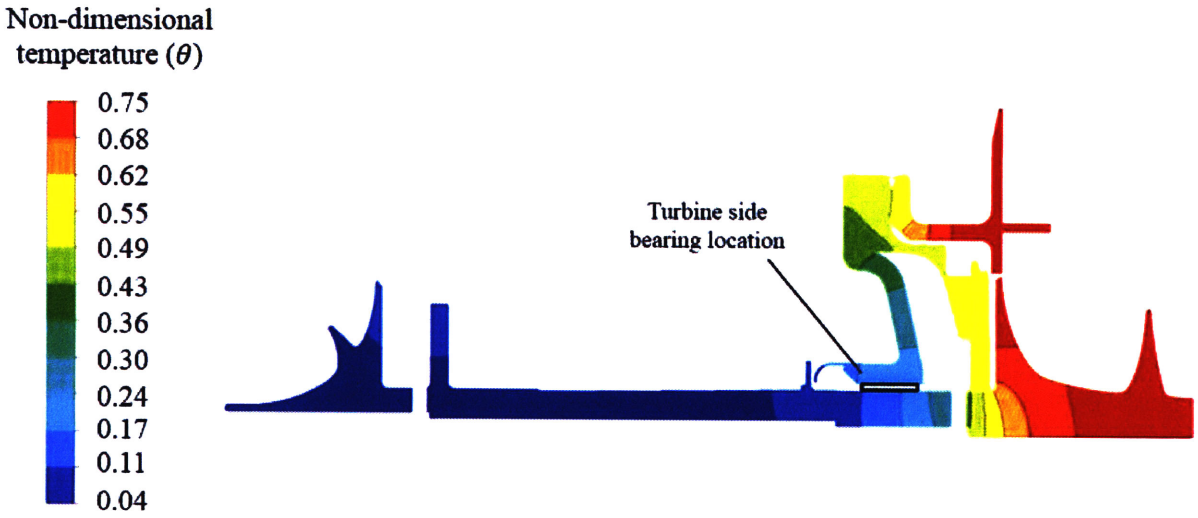

Figure 3-2: Temperature distribution in the shaft and the stationary structures of the representative engine. The location of the radial bearing on the turbine side is identified. The cooling flow through the bearing location flows from the compressor side toward the turbine side of the engine. Higher temperature on the turbine side and lower temperature on the compressor side suggests heat transfer toward the cold section of the engine.

On the compressor side, Figure 3-1 shows that heat transfer between the shaft and flow in the compressor impeller is only 0.4% of the turbine power output (8% of the total heat transfer from the turbine). This convection heat transfer is equivalent to 0.7 % of the compressor power. The heat transfer is negligible and the operation of the compressor impeller can practically be assumed to be adiabatic. This suggests that the current thermal management system provides adequate cooling air and proper heat transfer path to prevent performance deterioration of the compressor from excessive heat transfer.

Temperature distribution in the engine under steady-state operation is shown in Figure 3-2. The temperature distribution is non-dimensionalized as shown in Equation 3.1.

$$\theta = \frac{T - T_i}{T_{TIT} - T_i}, \tag{3.1}$$

where θ is the non-dimensional temperature, T temperature, T_i the initial temperature, and T_{TIT} the turbine inlet temperature.

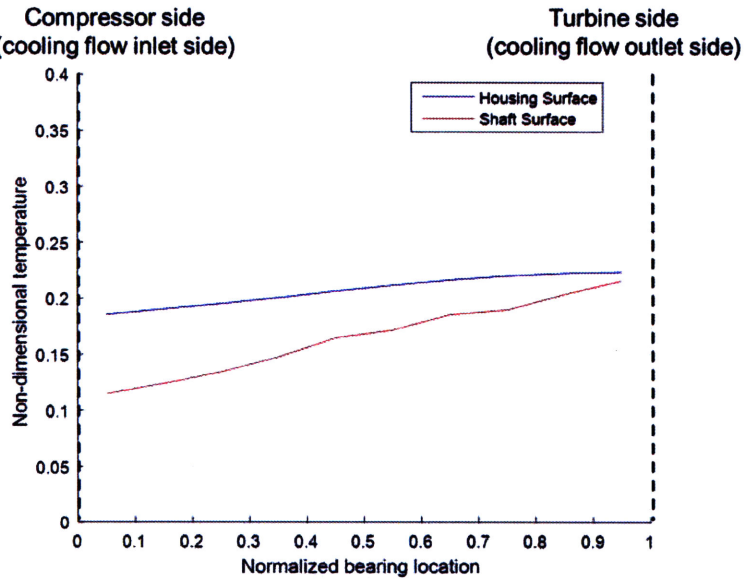

Figure 3-3: Axial temperature distribution of the housing surface and the shaft surface within the turbine side bearing. Temperature of the shaft and the housing is higher on the turbine side of the bearing. The location of the turbine side bearing is shown in Figure 3-2. The axial bearing location is normalized with respect to the axial length of the bearing.

The temperature of the turbine housing is controlled by heat transfer at its boundaries. Figure 3-1 shows that heat transfer out of the bearing housing is by convection heat transfer to the cooling flow. This convection heat transfer is balanced by conduction heat transfer into the bearing housing. The conduction heat transfer is primarily from the turbine nozzle and it flows through stationary engine components and heats up the bearing housing. These conduction and convection heat transfer processes are the key heat transfer processes, which govern the temperature of the turbine bearing housing.

As the turbine housing becomes an important path of heat transfer, its temperature is higher than that of the cooling flow in the vicinity. The temperature of the shaft is high on the turbine side but rapidly drops where cooling flow is able to absorb heat transfer from the hot part. Figure 3-3 shows that at the turbine bearing location, the non-dimensional temperature of the housing is higher than the non-dimensional temperature of the shaft by approximately 0.04. It can be inferred that the thermal expansion of the housing would be greater than that of the shaft, given the two

structures share the same material. The temperature distribution will be used in the thermal-structural model to quantify the differential expansion of the turbine housing and the shaft.

3.2 Structural Expansion of Shaft and Bearing Housing

The source of the operability issue (see Chapter 1) during the engine operation of the representative engine is hypothesized to be from the differential thermal expansion of engine structures, resulting in a change of bearing clearance. It was hypothesized that at the steady-state operation, the thermal expansion mismatch results in an increased bearing clearance size. The increased bearing clearance size could be detrimental to robust operation of the engine. This section addresses the hypothesis by developing link between the temperature field of the engine structure and the thermal deformation of the engine structures.

Mechanical and thermal loads generated during engine operation cause stress and strain (deformation) in engine structures. Mechanical loads are from force and pressure applied at boundaries of a certain component and body force due to centrifugal effect. For thermal loads, temperature change from the initial temperature causes thermal deformation. Stress-free thermal expansion occurs only when temperature distribution is uniform or varies linearly. However, these two conditions are hardly met during engine operation. Therefore, there will be thermal stress introduced by thermal loads.

3D finite element model is utilized to compute stress and deformation caused by the rotational effect and thermal effect in the engine. The radial expansion of the engine components is non-dimensionalized as shown in Equation 3.2.

$$u^* = \frac{u}{\alpha_{\text{shaft}} R_{\text{shaft}} (T_{TIT} - T_i)}, \tag{3.2}$$

where u^* is non-dimensional radial expansion, u dimensional radial expansion, α_{shaft}

the coefficient of thermal expansion of the shaft, R_{shaft} , the radius of the shaft at the bearing location, T_i the initial temperature, and T_{TIT} the turbine inlet temperature.

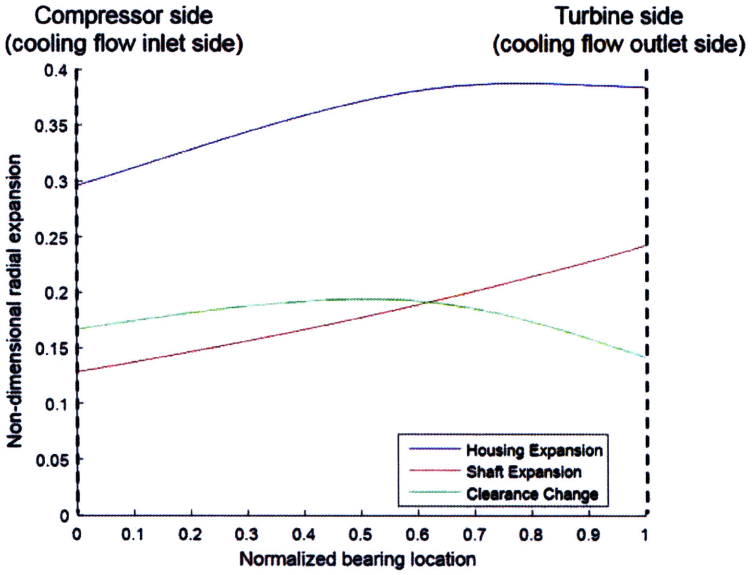

Figure 3-4: Radial expansion of the engine shaft and the bearing housing at the bearing location under steady-state operation. The maximum expansion of both components exists on the hot side of the bearing, where the temperature is higher. Change in bearing clearance is estimated from relative expansion of the two components. The radial expansion of the housing is larger than that of the shaft, causing an increased in the bearing clearance.

Under the rotating and thermal effects, radial expansion of the shaft and the bearing housing is shown in Figure 3-4. The radial expansion of the bearing housing is larger than that of the shaft at any axial location, leading to an increase in the bearing clearance. The radial expansion mismatch can be computed from Equation 3.3.

$$\Delta u^*(\chi) = u_h^*(\chi) - u_s^*(\chi), \tag{3.3}$$

where $\Delta u^*(\chi)$ is the radial expansion mismatch, $u_h^*(\chi)$ the radial expansion of the housing, and $u_s^*(\chi)$ the radial expansion of the shaft. Positive radial expansion mismatch indicates an increase in the bearing clearance. On the other hand, negative radial expansion mismatch indicates a reduction in the bearing clearance. The radial expansion mismatch of 1 means that the size of the radial expansion mismatch would

be equivalent to the stress-free radial thermal expansion of the shaft under the turbine inlet temperature.

The axial average of the non-dimensional radial expansion mismatch is approximately 0.19. The maximum expansion of both components exists on the hot side of the bearing. This is consistent with the temperature distribution shown earlier in Figure 3-3 as high local temperature drives larger thermal expansion. The largest radial expansion mismatch occurs near the axial center of the bearing and the smallest (but not negative) radial expansion mismatch occurs at the hot end of the bearing.

From the computed result presented in the above, the hypothesized differential expansion at the bearing location is confirmed. As literature review suggests linkage between an increase in bearing clearance size and reduction in stiffness and damping coefficients of bearings, the operability issue (whirl instability) observed in the representative engine could be caused by the net increase in the bearing clearance. The increase in the axial-average bearing clearance will be treated as the key characteristic and it needs to be adjusted into the acceptable range. As such, computed results and experimental observation are qualitatively in good accord.

In addition, the deformation of the engine shaft is assessed under the rotational effect only. The non-dimensional radial deformation of the shaft at the turbine bearing location due to only the rotational effect is approximately 0.017 (approximately 10% of the total radial deformation). Therefore, it can be inferred that the rotational effect does not significantly affect the change in the bearing clearance operation and the thermal effect is more significant during steady-state operation.

3.3 Summary

Fluid-thermal flow processes in the representative engine are first investigated. Steady 3D CFD with a CHT module is used to carry out calculations to assess the performance of the thermal management system and show heat transfer paths in the engine. Most of the heat transfer from the turbine is absorbed by the cooling flow. On the compressor side, heat transfer between the shaft and flow in the compressor impeller is

negligible and the operation of the compressor impeller remains practically adiabatic. Heat transfer toward the bearing housing is conduction heat transfer primarily from the turbine. Heat transfer out of the bearing housing is by convection heat transfer to the cooling flow. These conduction and convection heat transfer processes are the key heat transfer processes, which govern the temperature of the turbine bearing housing.

The temperature of the shaft is high on the turbine side but rapidly drops where cooling flow is able to absorb heat transfer from the hot part. At the turbine bearing location, the non-dimensional temperature of the housing is higher than the non-dimensional temperature of the shaft by approximately 0.04 on a non-dimensional basis.

Connection between temperature field of the engine structure and the thermal deformation of the engine structure is developed. 3D finite element model is utilized to compute stress and deformation caused by rotational effect and thermal effect in the engine. Computed result shows that the rotational effect does not significantly affect the radial expansion of the shaft and the thermal effect is more significant. The radial deformation of the bearing housing is larger than that of the shaft at any axial location. There is a net increase in the bearing clearance and the axial average of the non-dimensional radial expansion mismatch is approximately 0.19. The computed result confirms the hypothesized differential expansion mismatch. The operability issue (whirl instability) observed during the high-speed operation in the representative engine could be caused by the net increase in the bearing clearance as literature review suggests. As such, computed results and experimental observation are in accord.

Chapter 4

Differential Expansion in Shaft-Bearing Housing Clearance during Engine Start-Up Process

It was observed in experiments that attempts to reduce the bearing clearance size during the steady-state operation caused thermal rubbing between the engine shaft and the bearing top foil during an engine start-up process. This experimental observation suggests that a change in the bearing clearance is negative during the early phrase of the engine starting-up process and becomes positive as the start-up process continues. Therefore, transient 3D CHT CFD and 3D FE are utilized to assess this thermal-structural behavior of the bearing during an engine start-up process. Insights from the computed results will be used as foundation of an engineering root cause analysis (see Appendix A) for formulating solutions to the differential expansion mismatch issue.

4.1 Governing Thermal-Fluid Processes during Engine Start-Up Process

An engine start-up process is simplified for simulation through a transient 3D CHT CFD solver. The engine speed is set to be 190,000 RPM at the beginning of the start-up process. It is assumed that time timescale of the fluid flow to achieve a steady state is much shorter than that of the heat transfer in the solid. In other words, the fluid flow is quasi-steady relative to the heat transfer flow in the solid. As such, the main fluid flow is obtained from another set of calculation where the boundary conditions between the fluid flow and the solid are treated as adiabatic. The initial temperature of the engine structures is the ambient temperature. The boundary conditions of the main flow path, including the compressor, the turbine, and the leakage flow are similar to those from steady-state calculations and treated as time-invariant. The difference between the initial temperature and the turbine temperature causes heat diffusion in the engine structures and introduces temperature variation in time.

Computed result is used to indicate a pattern of heat diffusion from the main flow path to the turbine bearing location. Figure 4-1 shows temperature distribution on a cross-section of the engine from the beginning of the start-up process to the steady-state operation. Time is represented in a non-dimensional manner as Fourier number (Fo) based on the shaft length (L_s) and its thermal diffusivity (κ_s). Equation 4.1 shows the relation between time and Fourier number.

$$Fo = \frac{\kappa_s t}{L_s^2} \tag{4.1}$$

As time increases, heat diffuses from the turbine to the shaft and the bearing housing. It can be seen that the heat transfer path from the turbine to the bearing location on the bearing housing side is longer than that on the shaft side. Figure 4-2 shows the temperature trend over time at the bearing location on the housing side and the shaft side. Temperature at the bearing location on the shaft side is higher than that on the turbine housing side at the start of the process. At Fourier

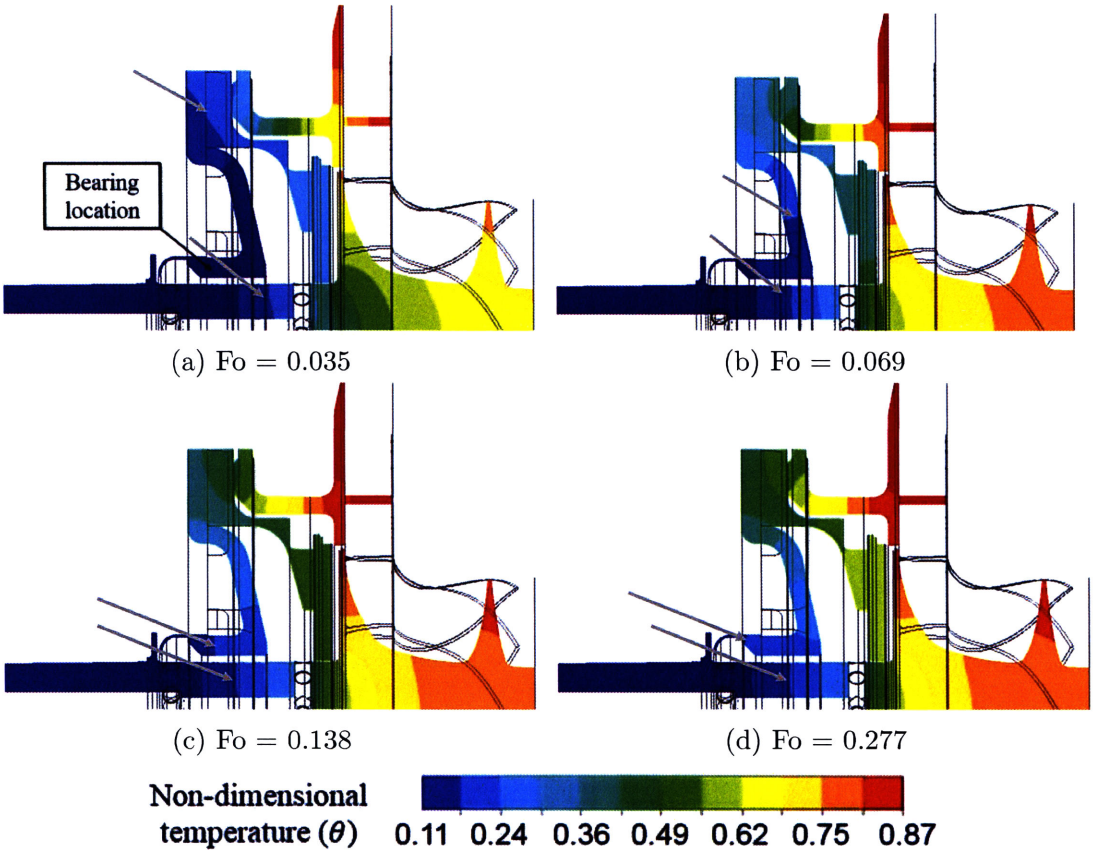

Figure 4-1: Temporal evolution of temperature distribution in engine structures near the bearing location due to heat transfers from the turbine. Temperature at the bearing location during the same time period is provided in Figure 4-2. The grey arrows keep track of how far conduction heat transfer from the turbine penetrates to the bearing location. Because the heat transfer path on the shaft side is shorter than that on the housing side, the heat transfer is able to reach the bearing location on the shaft side faster, causing a higher shaft temperature at the beginning of the start-up process. After the heat transfer reaches the bearing location on the housing side, the housing temperature becomes higher than the shaft temperature.

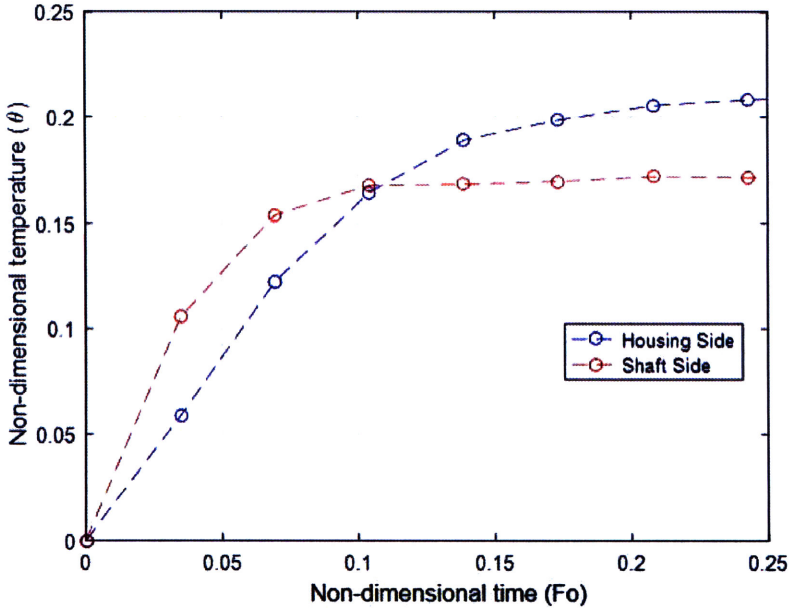

Figure 4-2: Increasing temperature of the housing and shaft surface at the turbine bearing location. Temperature on the shaft side is higher than that on the turbine housing side from the start of the process up to Fourier number of 0.11. Under steady-state operation, temperature on the bearing side is higher than that on the shaft side. This infers bearing clearance variation over time due to the changes in the temperature of the two components.

number of 0.1, the temperature at the same location on the bearing housing side still increases and surpasses its counterpart on the other side. The temperature at the two locations eventually reaches equilibrium temperature as shown in the previous chapter. This temperature trend suggests that thermal radial expansion of the shaft could be larger than that of the turbine housing during an earlier part of the start-up process. The differential radial expansion will be quantified in the next section with effect of thermal stress and material properties.

4.2 Structural Expansion of Shaft and Bearing Housing

Transient structural deformation is calculated with the 3D finite element tool based on the transient temperature distribution. Figure 4-3 shows axial variation of radial deformation of the shaft and the bearing housing at the bearing location. It can be seen that radial expansion of the shaft is larger than that of the housing at any axial location up to Fourier number of 0.021. From Fourier number of 0.028 to Fourier number of 0.035, radial expansion of the shaft is smaller than that of the housing on the colder end of the bearing (i.e. there is a net increase in radial clearance relative to the initial clearance size) and vice versa on the hot end of the bearing. At Fourier number of 0.035, the largest local non-dimensional radial expansion mismatch is observed to be negative 0.05 at the hot side of the bearing. The expansion mismatch at Fourier number of 0.035 supports the experimental observation, where thermal rubbing can occur during a start-up process if the bearing clearance is tightened. If the initial non-dimensional bearing clearance were smaller than 0.05, there would be a risk of thermal rubbing between the shaft and the top foil at this time unless the compliancy of the foil bearing helps mitigate the reduced clearance. Experimental attempts to reduce the bearing clearance confirms the reduced bearing clearance size during the start-up process. Because when the initial bearing clearance is reduced under a certain threshold, thermal rubbing between the shaft and the bearing top foil

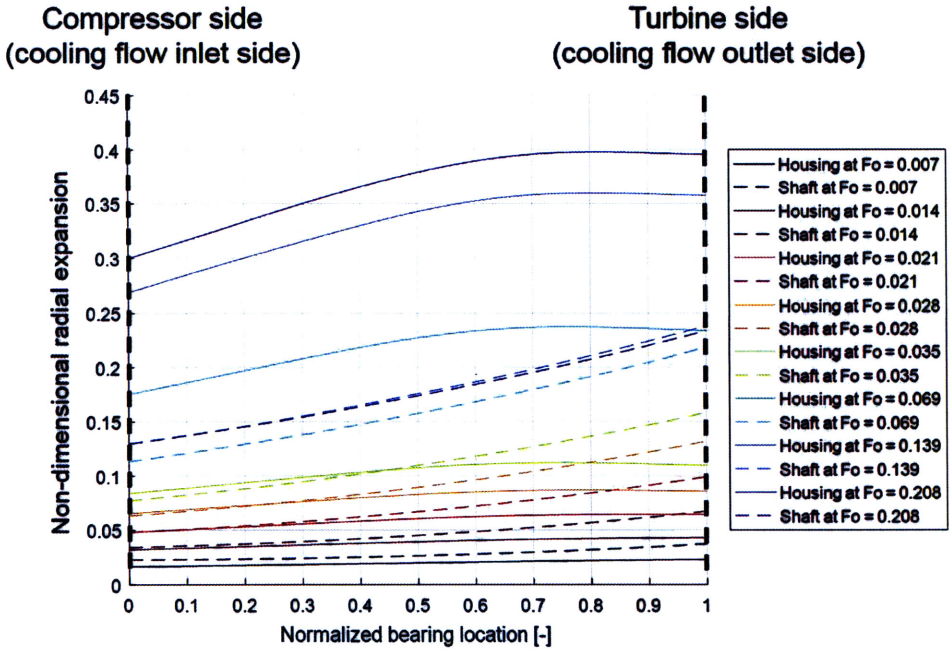

Figure 4-3: Axial variation of radial deformation of the engine shaft and the bearing housing at the bearing location during the engine start-up process. The axial average of the radial deformation during the same duration is provided in Figure 4-4. The radial expansion of the shaft and housing is larger on the turbine side of the bearing where temperature is higher. The radial expansion of the shaft is larger than that of the housing at any axial location up to Fourier number of 0.021 (i.e. there is a net reduction in the bearing clearance). After Fourier number of 0.069, radial expansion of the housing is larger than that of the shaft at any axial location (i.e. there is a net increase in the bearing clearance).

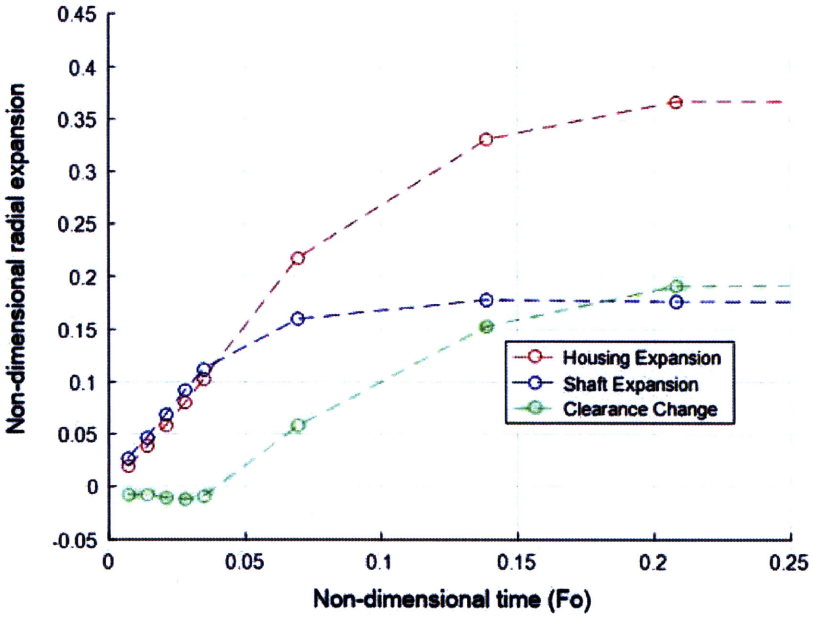

Figure 4-4: Axial average radial expansion of the shaft and the bearing housing at the bearing location during the engine start-up process. The negative clearance change indicates a reduction in the bearing clearance and the positive clearance change indicates an increase in the bearing clearance. The bearing clearance size reduces at the beginning of the start-up process and increases toward steady-state operation.

occurs during the start-up process. After Fourier number of 0.069, radial expansion of the housing is larger than that of the shaft at any axial location and there is a net increase in the bearing clearance.

The axial average radial expansion of the shaft and the bearing housing is shown as a function of time in Figure 4-4. The axial average radial expansion is assumed to be representative of the bearing clearance. As previously discussed in Chapter 3, the substantial increase in the bearing clearance could pose the risk of the whirl instability. The axial average radial thermal expansion can be used as the key metric to represent this issue. The positive radial expansion mismatch represents an increase in radial bearing clearance. The negative axial-average non-dimensional radial expansion is approximately 0.017 up to approximately Fourier number of 0.035. After Fourier number of 0.035, the differential axial-average radial expansion increases and reaches the largest value at the equilibrium state. It should be noted that the time at which

the bearing surface of bearing housing radially outgrows that of the shaft is different from the time at which temperature of the bearing surface on the bearing housing side becomes higher than its counterpart. This behavior occurs because the radial temperature gradient, which has higher temperature on the outer side, pulls the inner part of the structure radially outward. In addition, the coefficient of thermal expansion of the turbine bearing housing material is higher than that of the shaft, causing larger radial thermal expansion at the same temperature.

In addition, at Fourier number of 0.208, the radial expansion starts to converge to the steady-state expansion. The large net increase in non-dimensional bearing clearance of approximately 0.19 is similar to that previously computed from the steady-state calculation. This substantial increase in the bearing clearance could be a cause of a whirl instability observed in experiments as previously mentioned in Chapter 1. The reduced bearing clearance size during the start-up process suggests that the initial bearing clearance cannot be substantially reduced to mitigate the large increased bearing clearance at the steady state because there would be a risk of thermal rubbing between the shaft and the bearing during the start-up process. Therefore, in order to improve the engine operability, the radial expansion mismatch must be controlled under the acceptable limit of the bearing operation during the start-up process toward the steady-state operation. In other words, the shaft-bearing system that could provide temporally invariant bearing clearance during the start-up process is the ideal system for mitigating the whirl instability and for avoiding thermal rubbing.

4.3 Summary

Transient 3D CHT CFD and 3D FE are carried out to assess thermal-structural behavior of the engine at the bearing location during an engine start-up process. The computed result indicates the temperature trend over the engine start-up process. At the beginning of the engine start-up process, temperature at the bearing location on the shaft side is higher than that on the turbine housing side. After Fourier number of

0.1, the temperature on the housing side still increases and surpasses its counterpart on the other side. At Fourier number of 0.208, the temperature of the shaft and the housing reaches their equilibrium values.

Transient structural deformation is calculated with the 3D finite element tool based on the transient temperature distribution. From the initial condition to Fourier number of 0.021, radial expansion of the shaft is larger than that of the housing at any axial location, resulting in a smaller bearing clearance at any axial location. At Fourier number of 0.035, the largest local differential non-dimensional expansion mismatch is observed to be 0.05 at the hot side of the bearing. After Fourier number of 0.069, radial expansion of the housing is larger than that of the shaft at any axial location. At the end of the start-up process, a large increase in non-dimensional bearing clearance of approximately 0.19 is observed. This large increased bearing clearance could be a cause of a whirl instability observed in experiments as previously shown under the steady-state operation.

The reduced bearing clearance size during the start-up process suggests that the initial bearing clearance cannot be substantially reduced to mitigate the large increased bearing clearance at the steady state because there would be a risk of thermal rubbing between the shaft and the bearing during the start-up process. Therefore, in order to improve the engine operability, the radial expansion mismatch must be controlled under the acceptable limit of the bearing operation during the start-up process toward the steady-state operation.

Chapter 5

Reduced Order Model and Non-Dimensional Parameters

The goal of this chapter is to formulate a set of non-dimensional parameters that describe the relative importance of each heat transfer process in setting up the transient temperature distribution and the attending transient mechanical deformation in the shaft-bearing housing system. This will in turn provide an estimate on how the thermal induced effects (such as the changes in the bearing clearance resulting from the attending differential mechanical deformation in the shaft and the bearing housing) scale with the design/operational characteristics; this will also provide an enabler to establish the criteria for which the bearing clearance becoming vanishingly small.

This chapter is organized as follows. We first propose and develop a transient reduced order model that provides an adequate physical representation of the shaft-bearing housing system. The adequacy of the model is determined by assessing the results from the implementation of the reduced order model against those from the transient 3D CHT CFD model presented in the previous chapters. Non-dimensional parameters governing the transient operation of the shaft-bearing housing system are formulated based on the reduced order model. The functional dependence of the normalized thermal-induced differential mechanical deformation of the shaft-bearing

housing system is developed. A set of non-dimensional parameters is then used to establish controlling parametric trend in the differential thermal expansion mismatch of the shaft-bearing housing system. In particular, a criteria for which the bearing clearance becoming vanishingly small is derived and a scaling for the differential mechanical deformation is proposed.

5.1 Reduced Order Model

The use of transient 3D CHT CFD and finite element model enables incorporating complexities of fluid-thermal flow paths of the engine in determining the fluid flow, heat transfer, and any attending mechanical deformation. While such computations at substantially high cost in terms of resources are useful, they make the tasks of identifying the key parameters and scoping out the controlling parametric trend challenging.

To obtain key non-dimensional parameters and to provide a basis for mitigation of the thermal expansion mismatch issue, transient thermal characteristics of the engine are approximated with a reduced order model; the reduced order model, elaborated below, seeks only to retain the key geometric features and physical processes that are of pertinence to the thermal-induced mechanical deformation. In Chapter 4, transient temperature distribution from the CFD results shows substantial heat conduction from the turbine to the bearing housing through engine components. At the same time, the cooling flow keeps the temperature of the housing under the limit through convection heat transfer. This convection heat transfer also occurs on the surface of the shaft and other stationary engine components. These two heat transfer processes are proposed as the essential heat transfer processes in the reduced order model, which can adequately describe the thermal expansion mismatch in the engine.

The analyzed engine structure is simplified to reduce geometric complexities in the reduced order model. Figure 5-1 shows the generic engine structure for the reduced order model. The generic engine contains adequate features that allow heat transfer to flow from the turbine to the compressor. The configuration for this scenario is a

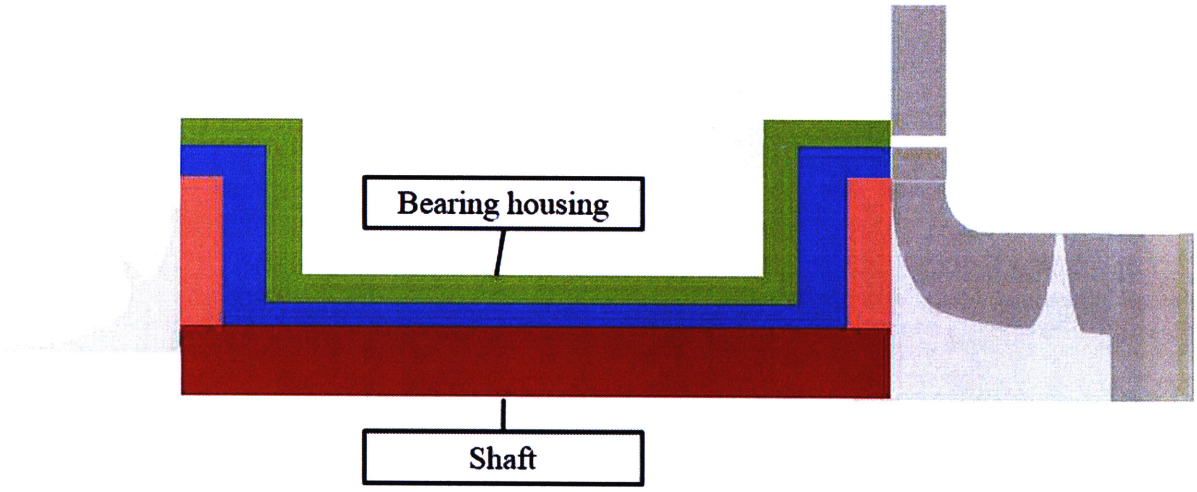

Figure 5-1: A cross-sectional view of the structure of the proposed generic micro gas turbine. The red region indicates the shaft. The blue region indicates the cooling flow. The green region indicates the housing. This proposed generic structure allows heat transfer from the turbine flowing toward the bearing location and the compressor.

solid shaft at the center and a bearing housing at a larger radius. The cross-sectional area of the shaft is constant in the axial direction. The housing has a larger radius at the compressor and the turbine end. The radius of the housing is smaller at the middle section, where journal bearings are located. The thickness of the housing is constant throughout. The cooling flow is between the two structures and absorbs heat flowing from the turbine side. The direction of the cooling flow is from the compressor side to the turbine side.

For the housing, convection heat transfer occurs on the inner surface from the compressor side to the turbine side and 1-D conduction heat transfer occurs inside the housing. For the shaft, convection heat transfer occurs on the middle part. The surface of the shaft near the compressor and the turbine is treated as adiabatic; 1-D conduction heat transfer occurs throughout the shaft. For modelling purpose, the housing is separated into 5 smaller domains and the shaft is separated into 3 smaller domains as shown in Figure 5-2. The governing equations controlling the temperature distribution are the conservation of energy, which accounts for conduction heat transfer and convection heat transfer. Figure 5-3 shows geometric parameters of the proposed generic micro gas turbine. These geometric parameters appear in the governing

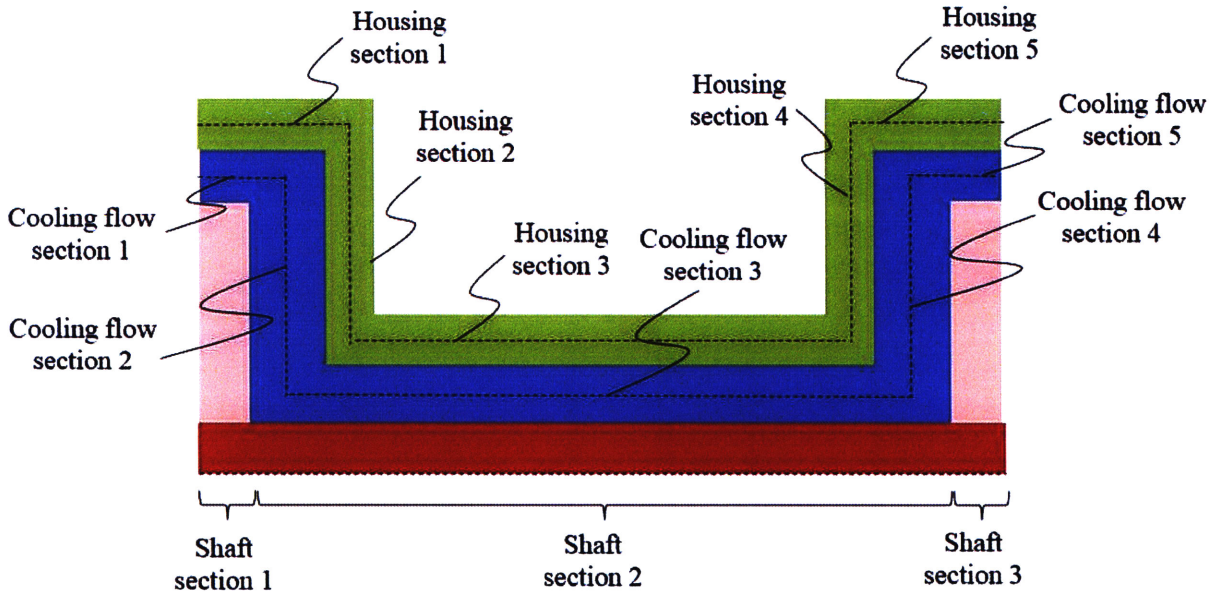

Figure 5-2: Breakdown of sections of each modelling component in the generic micro gas turbine. These sections are represented by their respective governing equations, which account for various heat transfer modes and directions of heat transfer.

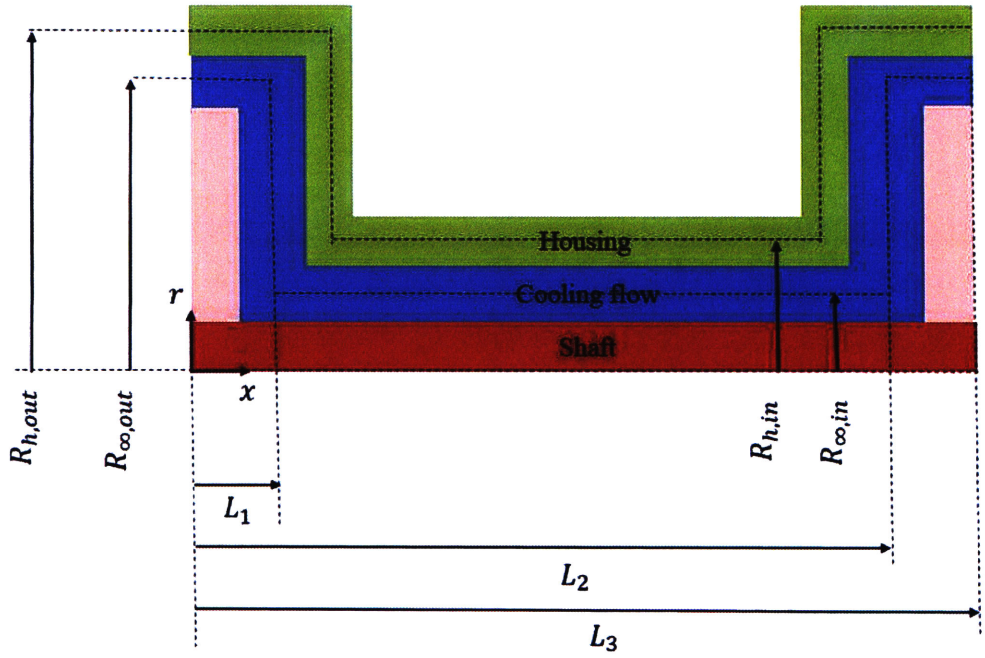

Figure 5-3: Geometric parameters of the proposed generic micro gas turbine. These geometric parameters appear in the governing equations and also control thermal expansion characteristics of the engine.

equations. A set of governing equations for the shaft, the housing, and the cooling flow is shown in Equation 5.1 - 5.8. It should be noted that with these two heat transfer modes, the nature of the governing equations of the housing and the shaft is essentially a 1-D transient fin equation.

The governing equations for the shaft are as follows.

For shaft section 1 ($0 \leq x \leq L_1$) and for shaft section 3 ($L_2 \leq x \leq L_3$),

$$\rho_s c_s A_s \frac{\partial T_s}{\partial t} = k_s A_s \frac{\partial^2 T_s}{\partial x^2}. \tag{5.1}$$

For shaft section 2 ($L_1 \leq x \leq L_2$),

$$\rho_s c_s A_s \frac{\partial T_s}{\partial t} = k_s A_s \frac{\partial^2 T_s}{\partial x^2} - h_s P_s \left(T_s - T_\infty\right), \tag{5.2}$$

where ρ_s is the density of the shaft material, c_s the specific heat capacity, A_s the cross-sectional area, t time, T_s temperature of the shaft, T_∞ temperature of the cooling flow, k_s the thermal conductivity, x the axial location, h_s the heat transfer coefficient, P_s the wetted perimeter.

For housing section 1 ($0 \leq x \leq L_1, r = R_{h,out}$) and for housing section 5 ($L_2 \leq x \leq L_3, r = R_{h,\text{out}}$)

$$\rho_h c_h A_{h,out} \frac{\partial T_h}{\partial t} = k_h A_{h,out} \frac{\partial^2 T_h}{\partial x^2} - h_h P_{h,out} \left(T_h - T_\infty\right). \tag{5.3}$$

For housing section 2 ($x = L_1, R_{h,\text{ in}} \leq r \leq R_{h,\text{ out}}$) and for housing section 4 ($x = L_2, R_{h,in} \leq r \leq R_{h,out}$),

$$\rho_h c_h \left(2\pi r B_h\right) \frac{\partial T_h}{\partial t} = k_h \left(2\pi r B_h\right) \frac{1}{r} \frac{\partial}{\partial r} \left(r \frac{\partial T_h}{\partial r}\right) - h_h (2\pi r) \left(T_h - T_\infty\right). \tag{5.4}$$

For housing section 3 ($L_1 \leq x \leq L_2, r = R_{h,in}$),

$$\rho_h c_h A_{h,in} \frac{\partial T_h}{\partial t} = k_h A_{h,in} \frac{\partial^2 T_h}{\partial x^2} - h_h P_{h,in} \left(T_h - T_\infty\right), \tag{5.5}$$

where ρ_h is the density of the housing material, c_h the specific heat capacity, $A_{h,\text{out}}$ the cross-sectional area at the outer radius, $A_{h,in}$ the cross-sectional area at the inner radius, B_h the thickness of the housing, t time, T_h temperature of the housing, T_∞ temperature of the cooling flow, k_h the thermal conductivity, x the axial location, r the radial location, h_h the heat transfer coefficient, $P_{h,\text{out}}$ the wetted perimeter at the outer radius, and $P_{h,in}$ the wetted perimeter at the inner radius.

For cooling flow section 1 $(0 \leq x \leq L_1, r = R_{h,out})$ and for cooling flow section 5 $(L_2 \leq x \leq L_3, r = R_{h,out})$,

$$\rho_\infty c_\infty A_{\infty,out} \frac{\partial T_\infty}{\partial t} = -\dot{m}_\infty c_\infty \left(\frac{\partial T_\infty}{\partial x} \right) + h_h P_{h,out} \left(T_h - T_\infty \right). \tag{5.6}$$

For cooling flow section 2 $(x = L_1, R_{h,in} \leq r \leq R_{h,out})$ and for cooling flow section 4 $(x = L_2, R_{h,in} \leq r \leq R_{h,out})$,

$$\rho_\infty c_\infty \left(2\pi r B_\infty \right) \frac{\partial T_\infty}{\partial t} = -\dot{m}_\infty c_\infty \left(\frac{\partial T_\infty}{\partial r} \right) + h_h (2\pi r) \left(T_h - T_\infty \right). \tag{5.7}$$

For cooling flow section 3 $(L_1 \leq x \leq L_2, r = R_{h,in})$,

$$\rho_\infty c_\infty A_{\infty,in} \frac{\partial T_\infty}{\partial t} = -\dot{m}_\infty c_\infty \left(\frac{\partial T_\infty}{\partial x} \right) + h_h P_{h,in} \left(T_h - T_\infty \right) + h_s P_s \left(T_s - T_\infty \right), \tag{5.8}$$

where ρ_∞ is the density of the cooling flow, c_∞ the specific heat capacity, $A_{\infty,\text{ out}}$ the cross-sectional area at the outer radius, $A_{\infty,in}$ the cross-sectional area at the inner radius, B_∞ the width of the cooling flow path, t time, T_h temperature of the housing, T_s temperature of the shaft, T_∞ temperature of the cooling flow, x the axial location, r the radial location, h_h the heat transfer coefficient of the housing side, h_s the heat transfer coefficient of the shaft side, $P_{h,\text{ out}}$ the wetted perimeter at the outer radius of the housing, $P_{h,in}$ the wetted perimeter at the inner radius of the housing, P_s the wetted perimeter of the shaft.

The elevated temperature in the engine is a physical driver for the thermal expansion in the engine. In general, thermal expansion and thermal stresses of solid bodies can

be determined through a thermoelastic problem. The thermoelastic problem can be represented with a displacement formulation, which is a combination of equilibrium relations and stress-strain relations. The displacement formulation without body forces is shown in Equation 5.9.

$$\begin{aligned}
&\left(\frac{v(3-2v)}{2(1+v)(1-2v)}\right)\frac{\partial}{\partial x}\left(\frac{\partial u_x}{\partial x}+\frac{\partial u_y}{\partial y}+\frac{\partial u_z}{\partial z}\right)+\left(\frac{v}{2(1+v)}\right)\nabla^2 u_x \\
&\qquad -\left(\frac{2v(2-v)}{(1+v)(1-2v)}\right)\alpha\frac{\partial T}{\partial x}=0, \\
&\left(\frac{v(3-2v)}{2(1+v)(1-2v)}\right)\frac{\partial}{\partial y}\left(\frac{\partial u_x}{\partial x}+\frac{\partial u_y}{\partial y}+\frac{\partial u_z}{\partial z}\right)+\left(\frac{v}{2(1+v)}\right)\nabla^2 u_y \\
&\qquad -\left(\frac{2v(2-v)}{(1+v)(1-2v)}\right)\alpha\frac{\partial T}{\partial y}=0, \\
&\left(\frac{v(3-2v)}{2(1+v)(1-2v)}\right)\frac{\partial}{\partial z}\left(\frac{\partial u_x}{\partial x}+\frac{\partial u_y}{\partial y}+\frac{\partial u_z}{\partial z}\right)+\left(\frac{v}{2(1+v)}\right)\nabla^2 u_z \\
&\qquad -\left(\frac{2v(2-v)}{(1+v)(1-2v)}\right)\alpha\frac{\partial T}{\partial z}=0,
\end{aligned} \tag{5.9}$$

where u_x is thermal expansion in the x-direction, u_y thermal expansion in the y-direction, u_z thermal expansion in the z-direction, v Poisson coefficient, and α coefficient of thermal expansion of the material.

A special case of the thermoelastic problem is when temperature is uniform in space and no forces or stresses are applied at the boundaries. Under this special case, a solid body is under a stress-free condition. The thermal expansion under this stress-free condition can be computed from Equations 5.10 .

$$\begin{aligned}
u_x &= \alpha x\,(T-T_i)\,, \\
u_y &= \alpha y\,(T-T_i)\,, \\
u_z &= \alpha z\,(T-T_i)\,.
\end{aligned} \tag{5.10}$$

To simplify the governing equations of the thermal-structural characteristics of the micro gas turbine, the structural expansion of the engine components is estimated based on a stress-free thermal expansion condition. The radial thermal expansion of the shaft and the housing at the bearing location is calculated from Equations 5.11.

$$u_{\text{radial},h} = \alpha_h R_{h,\text{in}} \left(T_h - T_i\right), \qquad u_{\text{radial},s} = \alpha_s R_s \left(T_s - T_i\right), \tag{5.11}$$

where $u_{\text{radial},h}$ is thermal expansion of the housing in the radial direction, $u_{\text{radial},s}$ the thermal expansion of the shaft in the radial direction, α_h coefficient of thermal expansion of the housing material, α_s coefficient of thermal expansion of the shaft material, $R_{h,in}$ the inner of the bearing housing, R_s the radius of the shaft, T_h temperature of the housing, T_s temperature of the shaft, and T_i the initial temperature of the engine.

In the next section, the key controlling non-dimensional parameters based on the proposed reduced order model are determined.

5.2 Non-Dimensional Parameters

Non-dimensional parameters are derived in this section to provide a framework for characterizing the thermal and structural behavior of the engine. Equations 5.12 - 5.19. are a non-dimensional form of Equations 5.1 - 5.8.

For shaft section 1 ($0 \leq \chi \leq L_1/L_{ref}$) and for shaft section 3 ($L_2/L_{ref} \leq \chi \leq L_3/L_{ref}$),

$$\frac{\partial \theta_s}{\partial \left(\kappa_s t/L_{ref}^2\right)} = \frac{\partial^2 \theta_s}{\partial \chi^2}. \tag{5.12}$$

For shaft section 2 ($L_1/L_{ref} \leq \chi \leq L_2/L_{ref}$),

$$\frac{\partial \theta_s}{\partial \left(\kappa_s t/L_{ref}^2\right)} = \frac{\partial^2 \theta_s}{\partial \chi^2} - \left(\frac{h_s P_s}{k_s A_s} L_{ref}^2\right)\left(\theta_s - \theta_\infty\right), \tag{5.13}$$

where $\theta_s = \left(T_s - T_i\right) / \left(T_{TIT} - T_i\right)$ is non-dimensional temperature of the shaft, $\theta_\infty = \left(T_\infty - T_i\right) / \left(T_{TIT} - T_i\right)$ non-dimensional temperature of the cooling flow, κ_s thermal diffusivity of the shaft material, and χ normalized axial location.

For housing section 1 ($0 \leq \chi \leq L_1/L_{\text{ref}}, \mathcal{R} = R_{\text{h,out}}/R_{\text{ref}}$) and for housing section 5 ($L_2/L_{ref} \leq \chi \leq L_3/L_{ref}, \mathcal{R} = R_{h,out}/R_{ref}$),

$$\frac{\partial \theta_h}{\partial \left(\kappa_s t / L_{ref}^2\right)} = \left(\frac{\kappa_h}{\kappa_s}\right)\left[\frac{\partial^2 \theta_h}{\partial \chi^2} - \left(\frac{h_h}{k_h B_h} L_{ref}^2\right)\left(\theta_h - \theta_\infty\right)\right]. \tag{5.14}$$

For housing section 2 ($x = L_1/L_{\text{ref}}, R_{\text{hin}}/R_{\text{ref}} \leq \mathcal{R} \leq R_{\text{hout}}/R_{\text{ref}}$) and for housing section 4 ($\chi = L_2/L_{ref}, R_{h,in}/R_{ref} \leq \mathcal{R} \leq R_{h,out}/R_{ref}$),

$$\frac{\partial \theta_h}{\partial \left(\kappa_s t / L_{ref}^2\right)} = \left(\frac{\kappa_h}{\kappa_s}\right)\left[\left(\frac{L_{ref}}{R_{ref}}\right)^2\left(\frac{1}{\mathcal{R}}\right)\frac{\partial}{\partial \mathcal{R}}\left(\mathcal{R}\frac{\partial \theta_h}{\partial \mathcal{R}}\right) - \left(\frac{h_h}{k_h B_h} L_{ref}^2\right)\left(\theta_h - \theta_\infty\right)\right]. \tag{5.15}$$

For housing section 3 ($L_1/L_{ref} \leq \chi \leq L_2/L_{ref}, \mathcal{R} = R_{h,in}/R_{ref}$),

$$\frac{\partial \theta_h}{\partial \left(\kappa_s t / L_{ref}^2\right)} = \left(\frac{\kappa_h}{\kappa_s}\right)\left[\frac{\partial^2 \theta_h}{\partial \chi^2} - \left(\frac{h_h}{k_h B_h} L_{ref}^2\right)\left(\theta_h - \theta_\infty\right)\right], \tag{5.16}$$

where $\theta_h = \left(T_h - T_i\right) / \left(T_{TIT} - T_i\right)$ is non-dimensional temperature of the housing, $\theta_\infty = \left(T_\infty - T_i\right) / \left(T_{TIT} - T_i\right)$ non-dimensional temperature of the cooling flow, κ_h thermal diffusivity of the housing material, κ_s thermal diffusivity of the shaft material, χ normalized axial location, and $\mathcal{R}$ normalized radial location.

For cooling flow section 1 ($0 \leq \chi \leq L_1/L_{ref}, \mathcal{R} = R_{h,out}/R_{ref}$) and for cooling flow section 5 ($L_2/L_{ref} \leq \chi \leq L_3/L_{ref}, \mathcal{R} = R_{h,out}/R_{ref}$),

$$\begin{aligned}\frac{\partial \theta_\infty}{\partial \left(\kappa_s t / L_{ref}^2\right)} = &- \left(\frac{\dot{m}_\infty L_{ref}}{\rho_\infty A_{\infty,out} \kappa_s}\right)\left(\frac{\partial \theta_\infty}{\partial \chi}\right) \\ &+ \left(\frac{\rho_s c_s A_s}{\rho_\infty c_\infty A_{\infty,out}}\right)\left[\left(\frac{h_h}{k_h B_h} L_{ref}^2\right)\left(\frac{k_h A_{h,out}}{k_s A_s}\right)\left(\theta_h - \theta_\infty\right)\right].\end{aligned} \tag{5.17}$$

For cooling flow section 2 ($\chi = L_1/L_{ref}, R_{h,in}/R_{ref} \leq \mathcal{R} \leq R_{h,\text{out}}/R_{ref}$) and for cooling flow section 4 ($\chi = L_2/L_{ref}, R_{h,in}/R_{ref} \leq \mathcal{R} \leq R_{h,out}/R_{ref}$),

$$\frac{\partial\theta_\infty}{\partial\left(\kappa_s t/L_{ref}^2\right)} = -\left(\frac{\dot{m}_\infty L_{ref}}{\rho_\infty A_{\infty,\text{out}}\kappa_s}\right)\left(\frac{R_{\infty,\text{out}}}{R_{\text{ref}}}\right)\left(\frac{L_{\text{ref}}}{R_{\text{ref}}}\right)\left(\frac{1}{\mathcal{R}}\right)\left(\frac{\partial\theta_\infty}{\partial\mathcal{R}}\right) + \left(\frac{\rho_s c_s A_s}{\rho_\infty c_\infty A_{\infty,\text{out}}}\right)\left[\left(\frac{h_h}{k_h B_h}L_{\text{ref}}^2\right)\left(\frac{k_h A_{\text{h,out}}}{k_s A_s}\right)\left(\frac{R_{\infty,\text{out}}}{R_{h,\text{out}}}\right)(\theta_h - \theta_\infty)\right]. \tag{5.18}$$

For cooling flow section 3 ($L_1/L_{ref} \leq \chi \leq L_2/L_{ref}, \mathcal{R} = R_{h,in}/R_{ref}$),

$$\frac{\partial\theta_\infty}{\partial\left(\kappa_s t/L_{ref}^2\right)} = -\left(\frac{\dot{m}_\infty L_{ref}}{\rho_\infty A_{\infty,out}\kappa_s}\right)\left(\frac{R_{\infty,\text{out}}}{R_{\infty,in}}\right)\left(\frac{\partial\theta_\infty}{\partial\chi}\right) + \left(\frac{\rho_s c_s A_s}{\rho_\infty c_\infty A_{\infty,out}}\right)\left(\frac{R_{\infty,\text{out}}}{R_{\infty,in}}\right)\left[\left(\frac{h_h}{k_h B_h}L_{ref}^2\right)\left(\frac{k_h A_{h,out}}{k_s A_s}\right)\left(\frac{R_{h,in}}{R_{h,out}}\right)(\theta_h - \theta_\infty) + \left(\frac{h_s P_s}{k_s A_s}L^2\right)(\theta_s - \theta_\infty)\right]. \tag{5.19}$$

The displacement formulation of the thermoelastic problem without body forces can also be represented in a non-dimensional form as shown in Equations 5.20.

$$\begin{aligned}
\left(\frac{(3-2v)}{(1-2v)}\right)\frac{\partial}{\partial x^*}\left(\frac{\partial u_x^*}{\partial x^*}+\frac{\partial u_y^*}{\partial y^*}+\frac{\partial u_z^*}{\partial z^*}\right)+\left(\frac{\partial^2 u_x^*}{\partial x^{*2}}+\frac{\partial^2 u_x^*}{\partial y^{*2}}+\frac{\partial^2 u_x^*}{\partial z^{*2}}\right)-\left(\frac{4(2-v)}{(1-2v)}\right)\frac{\partial\theta}{\partial x^*}=0,\\
\left(\frac{(3-2v)}{(1-2v)}\right)\frac{\partial}{\partial y^*}\left(\frac{\partial u_x^*}{\partial x^*}+\frac{\partial u_y^*}{\partial y^*}+\frac{\partial u_z^*}{\partial z^*}\right)+\left(\frac{\partial^2 u_y^*}{\partial x^{*2}}+\frac{\partial^2 u_y^*}{\partial y^{*2}}+\frac{\partial^2 u_y^*}{\partial z^{*2}}\right)-\left(\frac{4(2-v)}{(1-2v)}\right)\frac{\partial\theta}{\partial y^*}=0,\\
\left(\frac{(3-2v)}{(1-2v)}\right)\frac{\partial}{\partial z^*}\left(\frac{\partial u_x^*}{\partial x^*}+\frac{\partial u_y^*}{\partial y^*}+\frac{\partial u_z^*}{\partial z^*}\right)+\left(\frac{\partial^2 u_z^*}{\partial x^{*2}}+\frac{\partial^2 u_z^*}{\partial y^{*2}}+\frac{\partial^2 u_z^*}{\partial z^{*2}}\right)-\left(\frac{4(2-v)}{(1-2v)}\right)\frac{\partial\theta}{\partial z^*}=0,
\end{aligned} \tag{5.20}$$

where $u^* = u/\left(\alpha\left(T_{TIT}-T_i\right)R_{ref}\right)$ is non-dimensional thermal expansion in the respective direction, $\theta = \left(T-T_i\right)/\left(T_{TIT}-T_i\right)$ non-dimensional temperature, x^* on-dimensional location in the x-direction, y^* non-dimensional location in the y-direction, z^* non-dimensional location in the z-direction, and v Poisson coefficient.

This equation suggests that non-dimensional thermal expansion of the structure is a function of non-dimensional temperature, Poisson coefficient, and non-dimensional location.

Using the stress-free approximation, thermal expansion in the radial direction of

the housing and the shaft is approximated from Equation 5.21. The ratio of coefficient of thermal expansion of the housing to that of the shaft will be referred to as Π_5

$$\begin{aligned} u^*_{r,h} &= \frac{u_{r,h}}{\alpha_s R_{ref}\left(T_{TIT} - T_i\right)} = \left(\frac{\alpha_h}{\alpha_s}\right)\left(\frac{R_{h,in}}{R_{ref}}\right)\theta_h, \\ u^*_{r,s} &= \frac{u_{r,s}}{\alpha_s R_{ref}\left(T_{TIT} - T_i\right)} = \left(\frac{R_s}{R_{ref}}\right)\theta_s. \end{aligned} \tag{5.21}$$

From the non-dimensional equations, the non-dimensional parameters are categorized in 7 groups as follows.

1. 3 non-dimensional temperatures
   (a) Non-dimensional shaft temperature θ_s
   (b) Non-dimensional housing temperature θ_h
   (c) Non-dimensional cooling flow temperature θ_∞
2. 2 non-dimensional radial thermal expansions
   (a) Non-dimensional radial thermal expansion of shaft $u^*_{r,s}$
   (b) Non-dimensional radial thermal expansion of housing $u^*_{r,h}$
3. 2 non-dimensional location parameters
   (a) Normalized axial location χ
   (b) Normalized radial location $\mathcal{R}$
4. 1 non-dimensional time parameter
   (a) Fourier number
   $$Fo = \kappa_s t / L^2_{ref}$$
5. 9 non-dimensional geometric parameters
   (a) 1 aspect ratio of engine (length to radius)
   $$\Psi_1 = L_{ref}/R_{ref}$$

(b) 3 axial length ratios of housing

$$\Psi_2 = L_1/L_{ref}$$
$$\Psi_3 = L_2/L_{ref}$$
$$\Psi_4 = L_3/L_{ref}$$

(c) 2 radius ratios of housing

$$\Psi_5 = R_{h,in}/R_{ref}$$
$$\Psi_6 = R_{h,out}/R_{ref}$$

(d) 2 radius ratios of cooling flow path

$$\Psi_7 = R_{\infty,in}/R_{ref}$$
$$\Psi_8 = R_{\infty,in}/R_{ref}$$

(e) 1 radius ratio of shaft

$$\Psi_9 = R_s/R_{ref}$$

6. 6 non-dimensional thermal parameters

(a) Shaft fin parameter

$$N_s = \sqrt{\frac{h_s P_s}{k_s A_s}} L_{ref}$$

(b) Housing fin parameter

$$N_h = \sqrt{\frac{h_h}{k_h B_h}} L_{ref}$$

(c) Relative heat diffusivity in housing and shaft

$$\Pi_1 = \frac{\kappa_h}{\kappa_s}$$

(d) Relative energy storage in fluid and shaft

$$\Pi_2 = \frac{\rho_s c_s A_s}{\rho_\infty c_\infty A_{\infty,out}}$$

(e) Relative advection in fluid and heat diffusion in shaft

$$\Pi_3 = \frac{\dot{m}_\infty L_{ref}}{\rho_\infty A_{\infty,out} \kappa_s}$$

(f) Relative heat conduction in housing and shaft

$$\Pi_4 = \frac{k_h A_{h,out}}{k_s A_s}$$

7. 1 non-dimensional structural parameter

(a) Ratio of coefficient thermal expansion of the housing to that of the shaft

$$\Pi_5 = \alpha_h / \alpha_s$$

In this thesis, the reference length (L_{ref}) and reference radius (R_{ref}) are chosen to be the shaft length (L_s) and the shaft radius (R_s), respectively. This choice of the reference length scales is consistent with the definition of Fourier number and non-dimensional radial expansion shown previously.

In summary, Equations 5.22 and 5.23 show the functional form of the non-dimensional temperatures as a function of the location, geometric, and thermal parameters during transient and steady-state operation, respectively. The functional dependence of the thermal expansion in the housing and the shaft can be represented in terms of the input parameters to the thermal problem as shown in Equations 5.24 and 5.25 during transient and steady-state operation, respectively.

$$\begin{aligned} \theta_h(\chi, \mathcal{R}, Fo) &= f_h\left(\Psi_1, \ldots, \Psi_9, N_s, N_h, \Pi_1, \Pi_2, \Pi_3, \Pi_4\right), \\ \theta_s(\chi, \mathcal{R}, Fo) &= f_s\left(\Psi_1, \ldots, \Psi_9, N_s, N_h, \Pi_1, \Pi_2, \Pi_3, \Pi_4\right). \end{aligned} \tag{5.22}$$

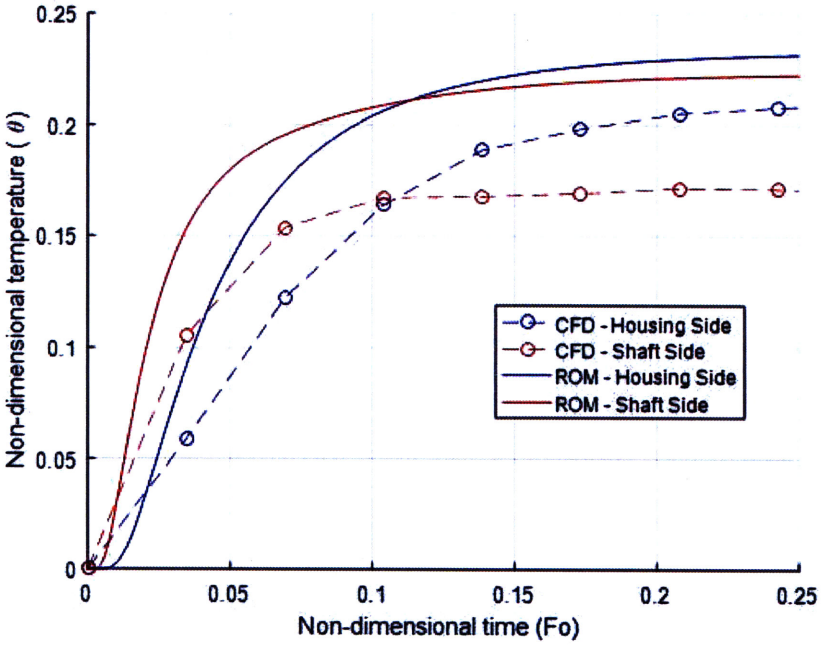

Figure 5-4: Temperature at the bearing location of the housing and shaft surface computed from the CFD model and the reduced order model (ROM). The ROM result is in accord with the CFD result as the shaft temperature is higher than the housing temperature at the beginning and the housing temperature is higher than the shaft temperature under steady-state operation.

$$\begin{aligned} \theta_h(\chi, \mathcal{R}, Fo \to \infty) &= f_h\left(\Psi_1, \ldots, \Psi_9, N_s, N_h, \Pi_2, \Pi_3, \Pi_4\right), \\ \theta_s(\chi, \mathcal{R}, Fo \to \infty) &= f_s\left(\Psi_1, \ldots, \Psi_9, N_s, N_h, \Pi_2, \Pi_3, \Pi_4\right). \end{aligned} \tag{5.23}$$

$$\begin{aligned} u^*_{r,h}(\chi, \mathcal{R}, Fo) &= f_h\left(\Psi_1, \ldots, \Psi_9, N_s, N_h, \Pi_1, \Pi_2, \Pi_3, \Pi_4, \Pi_5\right), \\ u^*_{r,s}(\chi, \mathcal{R}, Fo) &= f_s\left(\Psi_1, \ldots, \Psi_9, N_s, N_h, \Pi_1, \Pi_2, \Pi_3, \Pi_4\right). \end{aligned} \tag{5.24}$$

$$\begin{aligned} u^*_{r,h}(\chi, \mathcal{R}, Fo \to \infty) &= f_h\left(\Psi_1, \ldots, \Psi_9, N_s, N_h, \Pi_2, \Pi_3, \Pi_4, \Pi_5\right), \\ u^*_{r,s}(\chi, \mathcal{R}, Fo \to \infty) &= f_s\left(\Psi_1, \ldots, \Psi_9, N_s, N_h, \Pi_2, \Pi_3, \Pi_4\right). \end{aligned} \tag{5.25}$$

5.3 Assessment of Model Against CFD Data

Computed results from the reduced order model are assessed against the CFD results, which were shown in Chapter 4. Figure 5-4 shows temperature at the bearing location

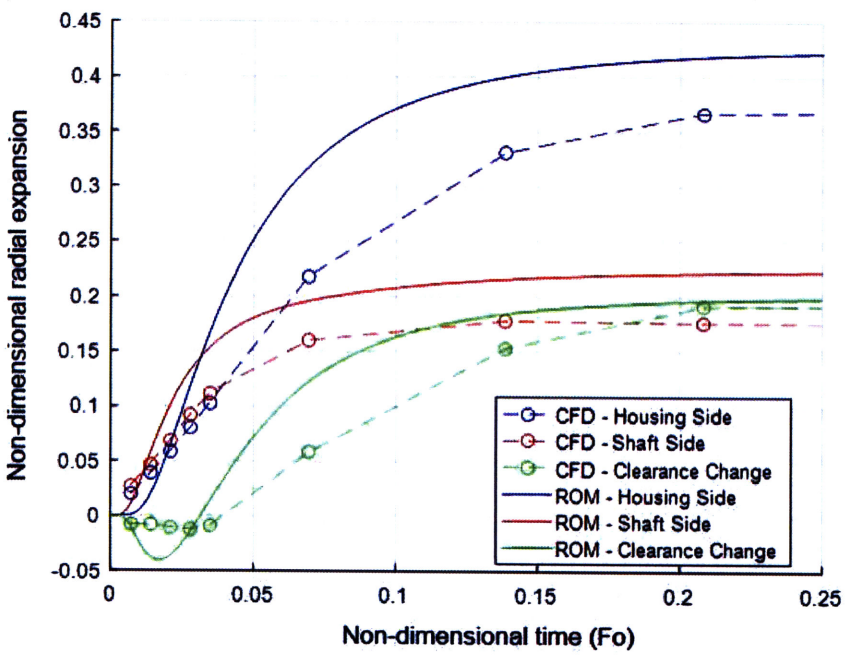

Figure 5-5: Radial thermal expansion at the bearing location of the housing and shaft surface computed from the CFD and FE model, and the reduced order model (ROM). The ROM result is in accord with the CFD and FE result. The shaft expansion is larger than the housing expansion at the beginning, causing a reduced bearing clearance. The housing expansion is larger than the shaft expansion under steady-state operation, causing an increased bearing clearance. The ROM tends to overestimate the shaft and housing expansion but the clearance change appears to be in good agreement.

computed from the reduced order model and the CFD model during the start-up process. The results from both the reduced order model and the CFD model shows similar trends; at the bearing location, the temperature on the shaft side is higher than that of the housing up to Fourier number of approximately 0.12. However, the steady-state temperature computed from the reduced order model is higher than that computed from the CFD model. This could be due to the lack of convection resistance between the hot gas and the hot engine structures on the turbine side and also the heat transfer path on the turbine side, which is more convoluted in the CFD model.

Structural deformation at the bearing location and the change in the bearing clearance size are shown in Figure 5-5. The reduced order model and the CFD model provide similar trends. Initially, the shaft expands at a faster rate than the housing,

resulting in a net reduction of the bearing clearance size. The largest reduction in the bearing clearance occurs at Fo $\approx$ 0.02 in the reduced order model and Fo $\approx$ 0.03 in the CFD model. The change in the bearing clearance is neutral at approximately Fo $\approx$ 0.04 for both models. Subsequently, the housing still radially expands at a faster rate and the bearing clearance size increases further. The reduced order model and the CFD model provide similar results, where the thermal expansion of the housing is larger than that of the shaft. At the steady-state, the thermal expansion of the housing and the shaft computed from the reduced order model is slightly larger than that computed from the CFD model. This is partly due to the higher steady-state temperatures. However, the discrepancy of the steady-state change in the bearing clearance computed from the reduced order model result and the CFD result is negligible. The assessment suggests that the reduced order model provides a reasonable estimate of the thermal-structural characteristics of the engine.

5.4 Approximate Analytical Solutions to Reduced Order Model

It is proposed that solutions to the reduced order model can be approximately represented as analytical solutions. The conservation of energy equation for the housing and the shaft, which is shown in Equation 5.12 - 5.16, is similar to a conventional transient fin equation, which is shown in Equation 5.26.

$$\frac{\partial \theta}{\partial Fo} = \frac{\partial^2 \theta}{\partial \chi^2} - N^2 \theta \tag{5.26}$$

The key difference between the fin equation in the reduced order model and the conventional fin equation is that the temperature of the fluid is not constant in the reduced order model while it is constant in the conventional fin model. In the reduced order model, the temperature of the fluid increases as the cooling flow flows from the compressor side to the turbine side. As a result, convective heat transfer is smaller in the reduced order model compared to that in the fin equation with uniform cooling

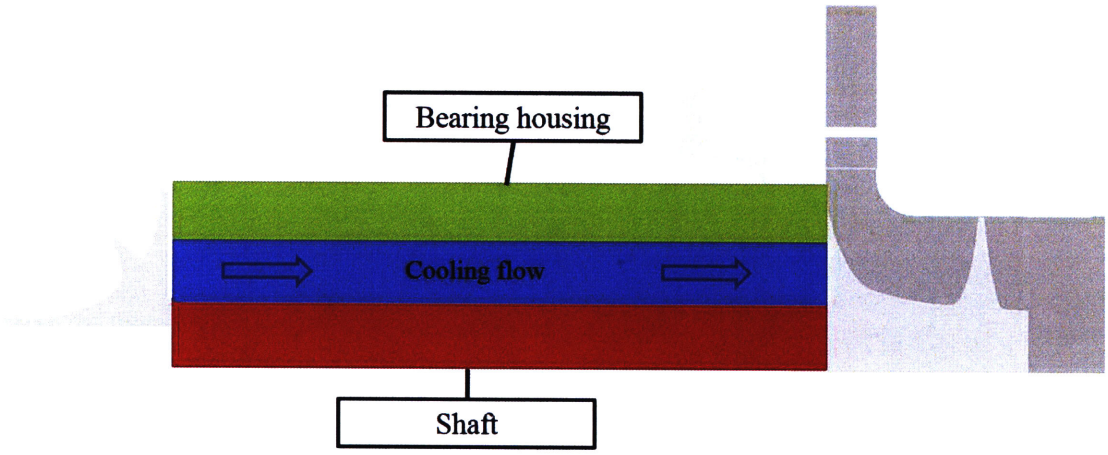

Figure 5-6: Simplified geometry of the bearing housing and the shaft for estimating effective fin parameter as a function of non-dimensional cooling flow parameters.

flow temperature. This smaller ratio of convection heat transfer to conduction heat transfer can be interpreted as the system having a smaller fin parameter as shown in Equation 5.27. This smaller fin parameter is referred to as an effective fin parameter. This effective fin parameter is approximated to be constant throughout the fin.

$$\begin{aligned} \frac{\partial\theta}{\partial Fo} &= \frac{\partial^2\theta}{\partial\chi^2} - N^2\left(\theta-\theta_\infty\right), \\ \frac{\partial\theta}{\partial Fo} &= \frac{\partial^2\theta}{\partial\chi^2} - \left[N^2\left(\frac{\theta-\theta_\infty}{\theta}\right)\right]\theta, \\ \frac{\partial\theta}{\partial Fo} &\approx \frac{\partial^2\theta}{\partial\chi^2} - N_{eff}^2\theta. \end{aligned} \tag{5.27}$$

The effective fin parameter is the same as the fin parameter when the temperature of the cooling flow is constant. On the other hand, the effective fin parameter is zero when the temperature of the structure is the same as the temperature of the cooling flow. Therefore, the effective fin parameter is bounded between 0 and the fin parameter.

The functional form of the ratio of the effective fin parameter to the fin parameter (effective fin parameter ratio) is estimated from a simplified case where cooling flow flows through a channel between an axial shaft and an axial housing. The simplified geometry is shown in Figure 5-6. This simplified case can be represented by Equations 5.28.

$$\frac{\partial\theta_s}{\partial\left(\kappa_s t/L_{ref}^2\right)} = \frac{\partial^2\theta_s}{\partial\chi^2} - \left(\frac{h_s P_s}{k_s A_s} L_{ref}^2\right)\left(\theta_s - \theta_\infty\right),$$

$$\frac{\partial\theta_h}{\partial\left(\kappa_s t/L_{ref}^2\right)} = \left(\frac{\kappa_h}{\kappa_s}\right)\left[\frac{\partial^2\theta_h}{\partial\chi^2} - \left(\frac{h_h}{k_h B_h} L_{ref}^2\right)\left(\theta_h - \theta_\infty\right)\right],$$

$$\frac{\partial\theta_\infty}{\partial\left(\kappa_s t/L_{ref}^2\right)} = -\left(\frac{\dot{m}_\infty L_{ref}}{\rho_\infty A_\infty \kappa_s}\right)\left(\frac{\partial\theta_\infty}{\partial\chi}\right)$$

$$+\left(\frac{\rho_s c_s A_s}{\rho_\infty c_\infty A_\infty}\right)\left[\left(\frac{h_h}{k_h B_h} L_{ref}^2\right)\left(\frac{k_h A_h}{k_s A_s}\right)\left(\theta_h - \theta_\infty\right) + \left(\frac{h_s P_s}{k_s A_s} L_{ref}^2\right)\left(\theta_s - \theta_\infty\right)\right]. \tag{5.28}$$

The effective fin parameter ratio ($\epsilon = N_{eff}/N$) is proposed to be a function of Π_2, Π_3, and Π_4, as shown in Equation 5.29 .

$$\epsilon = N_{eff}/N = f\left(\Pi_2 = \frac{\rho_s c_s A_s}{\rho_\infty c_\infty A_\infty}, \Pi_3 = \frac{\dot{m}_\infty L_{ref}}{\rho_\infty A_\infty \kappa_s}, \Pi_4 = \frac{k_h A_h}{k_s A_s}\right) \tag{5.29}$$

The minimum effective fin parameter ratio is 0 when convection heat transfer is negligible and cooling flow is not able to absorb heat flux from the solid structures. On the other hand, the maximum effective fin ratio is 1 when the temperature of the cooling flow is constant throughout the cooling flow path. The capability of the cooling flow to absorb heat is primarily controlled by the heat capacity of the cooling flow and mass flow rate of the cooling flow. It can be seen from Equations 5.28 that when Π_2 approaches 0 or Π_3 approaches infinity, the temperature of the cooling flow remains constant in the cooling flow path. However, when Π_2 approaches infinity or Π_3 approaches 0, the temperature of the cooling flow is close to the temperature of the solid. From Equations 5.28, Π_4 increases the effect of convection heat transfer on the cooling flow temperature. For Π_4 approaching 0, there is still convection heat transfer between the solid and the fluid; under this condition, the temperature of the cooling flow is not the same as the solid temperature and the effective fin parameter ratio is larger than 0. When Π_4 approaches infinity, the temperature of the cooling flow approaches the solid temperature and the effective fin parameter ratio approaches 0.

Based on these limiting cases, the functional form of the relation is proposed in

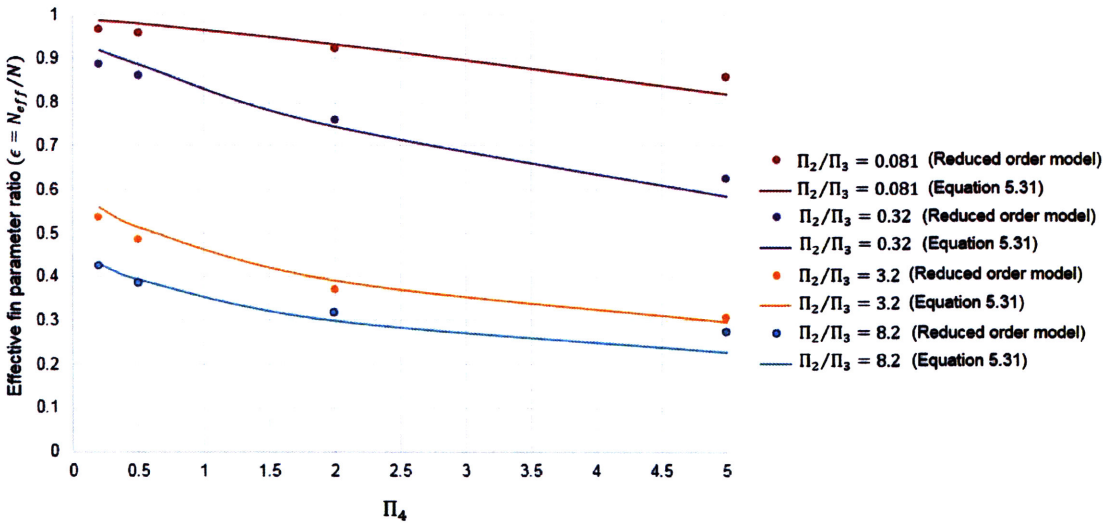

Figure 5-7: Parametric trend of effective fin ratio as a function of non-dimensional parameters of the cooling flow. The effective ratio is computed from the reduced order model (shown as discrete points) and estimated with Equation 5.31 (shown as solid lines). The functional dependence of the effective fin ratio is utilized in estimating effects of cooling flow on the transient temperature distribution.

Equation 5.30. The constants and exponents in Equation 5.30 are conjectured from the form of the equation describing the temperature of the cooling flow. Results from the reduced order model are used in addition to set the exponents and the constants in Equation 5.30.

$$\epsilon \approx \left(\frac{1}{C_1 \left(\Pi_2^{n_1} / \Pi_3^{n_2} \right) \left(1 + C_2 \Pi_4^{n_4} \right)^{n_5} + 1} \right)^{n_3} \tag{5.30}$$

For the fin parameter close to 1, the approximate effective fin parameter ratio is shown in Equation 5.31.

$$\epsilon = \frac{N_{h,eff}}{N_h} = \frac{N_{s,eff}}{N_s} \approx \left(\frac{1}{2 \left(\Pi_2 / \Pi_3 \right)^{(3/2)} \left(1 + \Pi_4 \right)^2 + 1} \right)^{(1/5)} \tag{5.31}$$

Figure 5-7 shows fin effective parameter ratio estimated based on Equation 5.31 against fin effective parameter computed directly from the temperature distribution. Discrepancy between the proposed functional form and the numerical result is approximately 10% throughout the range investigated. This functional form will be used as a

foundation to incorporate effects of cooling flow on temperature distribution of the cooling flow.

5.5 Scaling Rule of Thermal Expansion Mismatch of Shaft-Bearing Housing System

Scaling rule controlling the maximum change in the bearing clearance is developed in this section. Two required conditions for the maximum negative bearing clearance change to exist are shown in Equation 5.32 and 5.33.

$$\frac{\partial\left(u_h^* - u_s^*\right)}{\partial\left(Fo\right)} = 0 \tag{5.32}$$

$$\frac{\partial^2\left(u_h^* - u_s^*\right)}{\partial(Fo)^2} > 0 \tag{5.33}$$

The first condition requires the first order time derivative of the relative thermal expansion of the two structures to be zero. The second condition requires the second order time derivative of the relative thermal expansion of the two structures to be positive. The time at which the maximum negative thermal expansion mismatch occurs is referred to as the critical Fourier number ($Fo_{critical}$) as shown in Figure 5-8.

The radial thermal expansion of the shaft and the housing can be estimated as a function of temperature and coefficient of thermal expansion of the material as shown in Equation 5.21. Under this approximation, the two required conditions for the maximum negative thermal mismatch to exist can also be approximated as shown in Equation 5.34 and 5.35.

$$\frac{\alpha_h R_h}{\alpha_s R_s}\frac{\partial\theta_h}{\partial Fo} - \frac{\partial\theta_s}{\partial Fo} = 0 \tag{5.34}$$

$$\frac{\alpha_h R_h}{\alpha_s R_s}\frac{\partial^2\theta_h}{\partial Fo^2} - \frac{\partial^2\theta_s}{\partial Fo^2} > 0 \tag{5.35}$$

To develop a closed-form solution for the scaling, the geometry of the engine

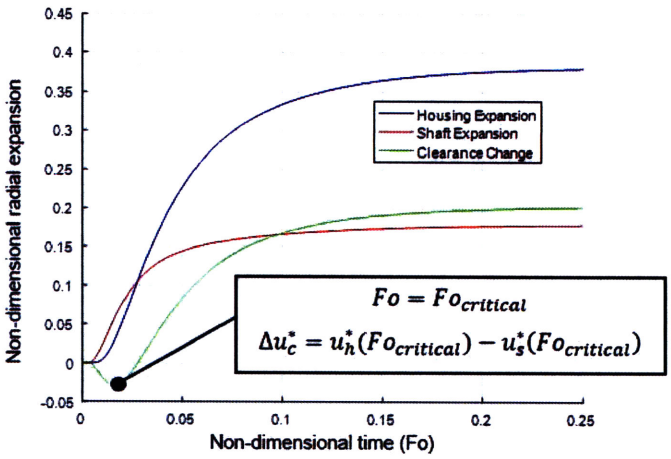

Figure 5-8: Maximum negative thermal expansion mismatch (the smallest bearing clearance) at the critical Fourier number.

model is further simplified. The geometry of the bearing housing is now a straight cylinder shell as shown in Figure 5-6. The functional form of transient temperature distribution required for calculating the maximum negative thermal expansion and the two associated conditions is approximated by Equation 5.36.

$$\theta(\chi, Fo) \approx \theta_{\text{steady}}(\chi)\left(1 - \exp\left(-\frac{5Fo}{Fo_{\text{steady}}}\right)\right) \tag{5.36}$$

This approximate transient temperature distribution is essentially scaled time response of steady-state temperature distribution. When the Fourier number is 0, the temperature distribution is the initial temperature distribution. When the Fourier number is Fo_{steady}, the transient temperature distribution is within approximately 1% of the steady-state distribution. Suryanarayana [27] provides Fo_{steady} for a transient fin with adiabatic tip under a step change in base temperature to be as

$$Fo_{steady} > \frac{1}{N^2 + \pi^2/4} \ln\left(\frac{100\pi \cosh N}{N^2 + \pi^2/4}\right).$$

However, transient temperature at different locations on the fin reaches 1% of the steady-state temperature at different times. For part of a fin that is closer to the boundary condition with a step change in temperature (the hot side of the fin), the

time required to reach to steady-state temperature is less than part of the fin that is away from the high temperature boundary condition (the cold side of the fin). Under this proposal, the steady-state Fourier number becomes a function of the location and it can be further approximated as

$$\mathrm{Fo}_{steady}(\chi) \approx \frac{1}{(1-\chi)^2}\left[\frac{1}{N^2+\pi^2/4}\ln\left(\frac{100\pi\cosh N}{N^2+\pi^2/4}\right)\right] \approx \frac{\mathrm{erfc}(\log(N))}{(1-\chi)^2}.$$

The steady-state Fourier number of the shaft and housing under the approximation are as follows. It should be noted that the ratio of thermal diffusivity appears in the steady-state Fourier number of the housing because the Fourier number is normalized with respect to the thermal diffusivity of the shaft.

$$Fo_{s,steady}(\chi) \approx \frac{\mathrm{erfc}\left(\log\left(N_{s,eff}\right)\right)}{(1-\chi)^2}.$$

$$Fo_{h,steady}(\chi) \approx \frac{\mathrm{erfc}\left(\log\left(N_{h,eff}\right)\right)}{(1-\chi)^2\left(\kappa_h/\kappa_s\right)} = \frac{\mathrm{erfc}\left(\log\left(N_{h,eff}\right)\right)}{(1-\chi)^2\Pi_1}.$$

Based on the approximate steady-state time scale, the full expression of the approximate transient temperature distribution of the shaft and housing can be written as in Equations 5.37. The approximate temperature distribution is treated as the solution to Equation 5.22 to obtain approximate scaling rule of thermal expansion mismatch in the engine.

$$\begin{aligned}
\theta_s(\chi, Fo) &\approx \theta_{s,steady}(\chi)\left(1-\exp\left(-\frac{5(1-\chi)^2 Fo}{\mathrm{erfc}\left(\log\left(N_{s,eff}\right)\right)}\right)\right), \\
\theta_h(\chi, Fo) &\approx \theta_{h,steady}(\chi)\left(1-\exp\left(-\frac{5(1-\chi)^2\Pi_1 Fo}{\mathrm{erfc}\left(\log\left(N_{h,eff}\right)\right)}\right)\right).
\end{aligned} \tag{5.37}$$

The scaling rule of thermal expansion mismatch in the engine is described by a set of equation as follows. Equation 5.38 describes the thermal expansion mismatch at the steady state operation. Equation 5.39 provides the critical Fourier number when the maximum negative thermal expansion (minimum bearing clearance) occurs if one should exist. Equation 5.40 provides a criterion whether the maximum negative

thermal expansion mismatch occurs at positive finite Fourier number or not. Equation 5.41 describes the maximum negative thermal expansion at the critical Fourier number.

$$\Delta u^*_{\text{steady}} = \left(\frac{\alpha_h}{\alpha_s}\right)\left(\frac{R_h}{R_s}\right)\theta_{\text{steady},h} - \theta_{\text{steady},s} \tag{5.38}$$

$$Fo_c = \frac{\left(\frac{Fo_{s,steady}}{5}\right)}{\left(\frac{Fo_{s,steady}}{Fo_{h,steady}}\right) - 1} \ln\left[\left(\frac{\alpha_h}{\alpha_s}\right)\left(\frac{R_h}{R_s}\right)\left(\frac{\theta_{h,steady}}{\theta_{s,steady}}\right)\left(\frac{Fo_{s,steady}}{Fo_{h,steady}}\right)\right] \tag{5.39}$$

$$\frac{Fo_{s,\text{steady}}}{Fo_{h,\text{steady}}} < 1 \tag{5.40}$$

$$\Delta u^*_c = \Delta u^*_{steady} - \left(\frac{Fo_{steady,s}}{Fo_{steady,h}} - 1\right)\theta_{steady,s} \exp\left(\frac{-5Fo_c}{Fo_{steady,s}}\right) \tag{5.41}$$

The result of the scaling is shown in Figure 5-9, Figure 5-10, and Figure 5-11 for a case where the boundary condition on the hot side (turbine side) is at constant temperature and the boundary condition on the cold side (compressor side) is adiabatic (i.e. there is no heat transfer into the compressor). The other thermal, structural, and geometric parameters of the case include: (1) $\Pi_1 = 0.4$,(2) $R_h/R_s = 1.2$,(3) $\Pi_5 = \alpha_h/\alpha_s = 1.2$,(4) $\chi = 0.8$.

Figure 5-9 shows Critical Fourier number (Fourier number at which the minimum bearing clearance occurs) as a function of effective housing fin parameter and effective shaft fin parameter. The color contour shows a regime in which the minimum bearing clearance can occur at positive and finite Critical Fourier number. Outside of the regime, the minimum bearing clearance can occur at steady-state when the effective housing parameter is substantially larger than the effective shaft fin parameter. On the other hand, the minimum bearing clearance occurs at the beginning (Critical Fourier number of 0) when the effective shaft fin parameter is substantially larger than the effective housing parameter.

Figure 5-10 shows bearing clearance change at Critical Fourier number as a function of effective housing fin parameter and effective shaft fin parameter. The bearing

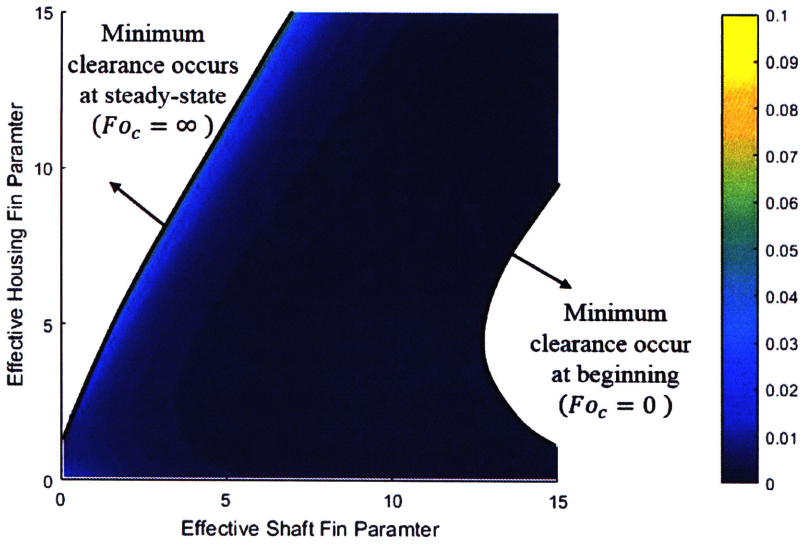

Figure 5-9: Critical Fourier number (Fourier number at which the minimum bearing clearance occurs) as a function of effective housing fin parameter and effective shaft fin parameter. The color regime shows when it is possible to have the minimum bearing clearance occurs at a positive and finite Fourier number.

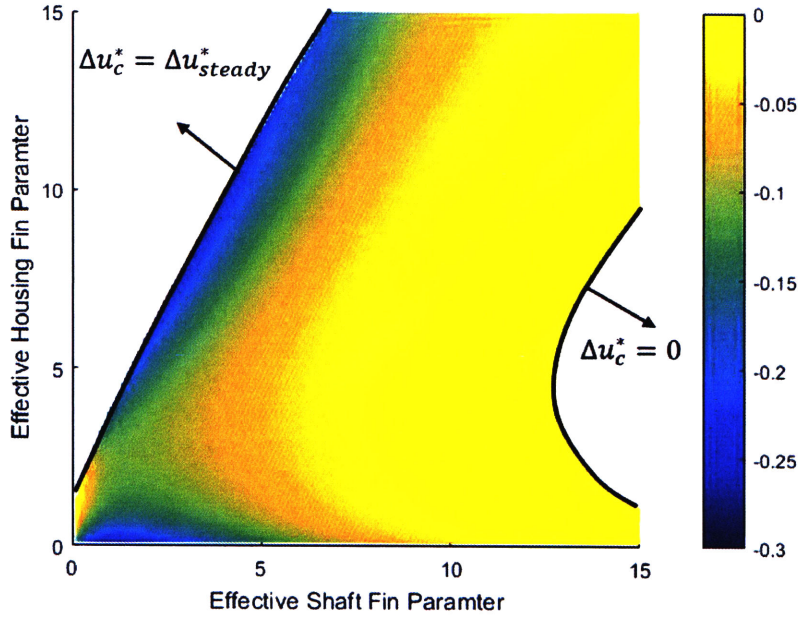

Figure 5-10: Bearing clearance change at Critical Fourier number. The minimum bearing clearance size occurs at this time instance and the bearing clearance change is negative. The color regime shows the bearing clearance change when the critical Fourier number is finite and positive.

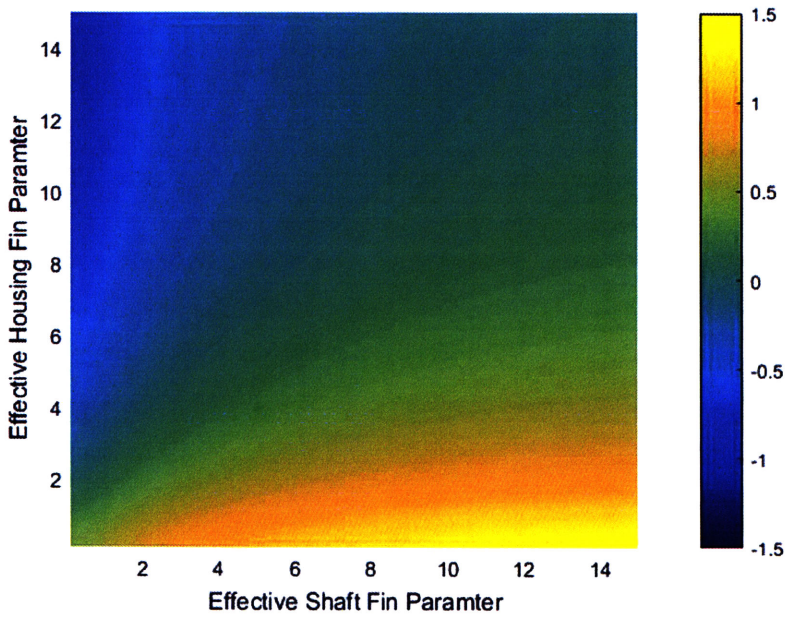

Figure 5-11: Bearing clearance change at steady-state as a function of effective housing fin parameter and effective shaft fin parameter. Positive bearing clearance change suggests an increased bearing clearance size. Negative bearing clearance change suggests a decreased bearing clearance size.

clearance change in this contour plot is negative because at Critical Fourier number, the bearing clearance is at its smallest size. If the minimum bearing clearance occurs at the steady-state, the minimum bearing clearance is equivalent to the steady-state bearing clearance. In addition, if the minimum bearing clearance occurs right at the beginning, the minimum clearance is equivalent to the initial clearance (i.e. there is no change in the clearance).

Figure 5-11 shows bearing clearance change at the steady-state condition as a function of effective housing fin parameter and effective shaft fin parameter. The change in the steady-state bearing clearance can be both negative and positive. When the effective shaft fin parameter is substantially larger than the effective housing fin parameter, the steady-state bearing clearance change is positive (i.e. the clearance increases). On the other hand, when the effective housing fin parameter is substantially larger than the effective shaft fin parameter, the steady-state bearing clearance change is negative (i.e. the clearance reduces). The steady-state bearing clearance change is

close to neutral when the effective housing fin parameter and the effective shaft fin parameter are similar.

Use of Figure 5-9, Figure 5-10, and Figure 5-11 together allow engine designers to determine the thermal expansion characteristics of the simplified engine on a direct basis. The engine could be modified to have desired thermal expansion characteristics by adjusting the effective shaft fin parameter, the effective housing fin parameter, the thermal diffusivity ratio (Π_1), the housing to shaft radius ratio (R_h/R_s), the coefficient of thermal expansion ratio (Π_5), and the location of the bearing. It should be noted that the two effective fin parameters represent the effect of the cooling flow. Therefore, adjusting the characteristics of the cooling flow (e.g. heat transfer coefficient, mass flow rate) would affect the two effective fin parameters and the overall thermal expansion characteristics as well.

The scaling rule is applied to the representative engine. The result from the scaling rule is assessed against that from the ROM. It should be noted that the bearing housing in the representative engine is not a straight cylinder (i.e. $R_{h,out}/R_{h,in} \neq 1$). Different length scales are used in the housing and shaft effective fin parameter. The thermal and structural parameters are similar to those in the ROM. Table 5.1 shows thermal expansion mismatch characteristics of the representative engine evaluated based from the scaling rule and the ROM. For this case, the scaling rule confirms that the minimum bearing clearance occurs and produces a similar bearing clearance variation trend. However, it underestimates the critical Fourier number. This is mainly due to the fact that the approximate temperature distribution does not properly account for the diffusion time from the turbine to the bearing location. An offset Fourier number ($Fo_{offset} \approx L^2_{turbine\,to\,bearing\,location}/L^2_{shaft} \approx 0.016$) can be added to reflect this additional diffusion time. The bearing clearance variations at the critical Fourier number and at steady-state are also underestimated as well. This result suggests that the scaling rule should be utilized as a preliminary tool for estimating thermal expansion mismatch characteristics and the ROM should be utilized for more accurate assessments.

Table 5.1: Thermal expansion mismatch characteristics of the representative engine estimated with various methods

Parameters	Scaling rule	ROM	CFD
Critical Fourier number (Fo_c)	1.4×10^{-3}	1.7×10^{-2}	2.8×10^{-2}
Adjusted Fourier number ($Fo_c + Fo_{offset}$)	1.7×10^{-2}	-	-
Non-dimensional thermal expansion mismatch at Fo_c (u_c^*)	-1.2×10^{-2}	-4.1×10^{-2}	-1.2×10^{-2}
Non-dimensional thermal expansion mismatch at steady-state (u_{steady}^*)	1.3×10^{-1}	2.0×10^{-1}	1.9×10^{-1}

5.6 Summary

A reduced order model is proposed for deriving the non-dimensional parameters and serving as the preliminary parametric assessment tool. The heat transfer processes in the reduced order model are the only essential processes that can adequately introduce the thermal expansion mismatch in the engine. This reduced order model will be used to formulate suggestions for the engine redesign to mitigate the thermal expansion mismatch issue.

In Chapter 4, transient temperature distribution from the CFD results shows substantial heat conduction from the turbine to the bearing housing through engine components. At the same time, the cooling flow keeps the temperature of the housing under the limit through convection heat transfer. This convection heat transfer also occurs on the surface of the shaft and other stationary engine components. These two heat transfer processes are proposed as the essential heat transfer processes in the reduced order model, which can adequately introduce the thermal expansion mismatch in the engine. The analyzed engine structure is simplified to reduce geometric parameters in the reduced order model. The simplified engine contains adequate features that allow heat transfer to flow from the turbine and the compressor.

The governing equations controlling the temperature distribution are the conservation of energy, which accounts for conduction heat transfer and convection heat transfer. A set of governing equations for the shaft, the housing, and the cooling flow is proposed. The governing equations of the thermal-structural characteristics of the micro gas

turbine are simplified, and the structural expansion of the engine components is estimated based on a stress-free thermal expansion condition.

The non-dimensional parameters, which are derived from the governing equations, are categorized in 7 groups: (1) 3 non-dimensional temperatures, (2) 2 non-dimensional structural thermal expansions, (3) 2 non-dimensional location parameters, (4) 1 non-dimensional time parameter, (5) 9 non-dimensional geometric parameters, (6) 6 non-dimensional thermal parameters, and (7) 1 non-dimensional structural parameter. The non-dimensional thermal parameters consist of: (1) shaft fin parameter, (2) housing fin parameter, (3) ratio of heat diffusivity of housing to that of shaft, (4) ratio of energy storage in cooling flow to that in shaft, (5) ratio of advection in fluid to heat diffusion in shaft, (6) ratio of heat conduction in housing to that in shaft. The only controlling structural parameter is the ratio of coefficient of thermal expansion of the housing to that of the shaft.

Computed results from the reduced order model are assessed against the CFD results. The reduced order model and the CFD model provide similar trends. Initially, the shaft expands at a faster rate than the housing, resulting a net reduction of the bearing clearance size. At the steady-state condition, both models suggests that the thermal expansion of the housing is larger than that of the shaft.

A scaling rule controlling the maximum change in the bearing clearance is developed for a simplified engine geometry. The scaling rule provides a closed-form solution for: (1) the critical Fourier number when the maximum negative thermal expansion mismatch (i.e. the minimum bearing clearance) occurs, (2) the criterion determining whether the maximum negative thermal expansion occurs or not, (3) the maximum negative thermal expansion at the critical Fourier number, and (4) the thermal expansion mismatch at the steady-state operation. These thermal expansion mismatch characteristics are represented as a function of effective housing fin parameter and effective shaft fin parameter. The effective fin parameters account for effects of conduction heat transfer, convection heat transfer, and cooling flow. The use of the scaling rule allows engine designers to determine the thermal expansion characteristics of the simplified engine on a direct basis.

Chapter 6

Proposed Solutions for Mitigating Differential Thermal Expansion through Tailoring Material Properties

In this chapter, proposed solutions for mitigating differential thermal expansion mismatch are discussed. The thermal expansion mismatch observed in the representative engine is considered as a design example. The computed results show that the differential thermal expansion mismatch occurs during the start-up process and at the steady-state operating condition. The thermal expansion mismatch during the start-up process results in a reduced bearing clearance size while the thermal expansion mismatch at the steady condition results in an increased bearing clearance. These reduced and increased bearing clearance need to be mitigated and controlled within the bound of the bearing operating envelope.

Solutions to the thermal expansion mismatch issue are not unique and are proposed at different levels of available technologies as the choice of material usage and engine design depends on engine developers. The non-dimensional parameters derived from the reduced order model are used as the basis for suggesting various solutions. The

focus of the design example is on the selection of the engine materials and not the engine design. This approach is first utilized because changes in the engine design and architecture would constitute a major task requiring substantial resources. The approach to mitigate the thermal expansion mismatch issue in this chapter can be generalized for a broad class of engine sizes.

6.1 Use of Novel Materials with Low or Neutral Coefficient of Thermal Expansion

Materials with low coefficient of thermal expansion (CTE) have been used for precision measuring devices to prevent thermal distortion in the devices [3]. Materials with lower CTE appear attractive as candidates to reduce the thermal expansion mismatch. Figure 6-1 shows CTE of various materials. Invar (FeNi36) is an example of materials with low CTE. However, the attribute of the materials might not be suitable for gas turbine applications. For example, if Invar is chosen as a new material choice of the engine, the use of Invar could be problematic for a gas turbine application because the maximum operating temperature of Invar (temperature at which Invar retains low coefficient of thermal expansion) is much lower than the operating temperature of a gas turbine. In addition, yield strength of Invar is approximately 500 MPa, which is relatively low compared to commonly used materials such as titanium alloys or nickel-based alloys, which have yield strength of approximately 1000 MPa. The lower yield strength of Invar requires structural integrity assessment of the rotational and structural engine components. If the original engine is designed in such a way that stress in the components is close to the yield strength of the material, an engine redesign is then required to redistribute and maintain stress under the material limit. This additional complication makes Invar unattractive as a candidate for the material choice for mitigating the thermal expansion mismatch issue.

Another approach to obtain materials with low or neutral coefficient of thermal expansion is through the use of mechanical metamaterials. Mechanical metamaterials

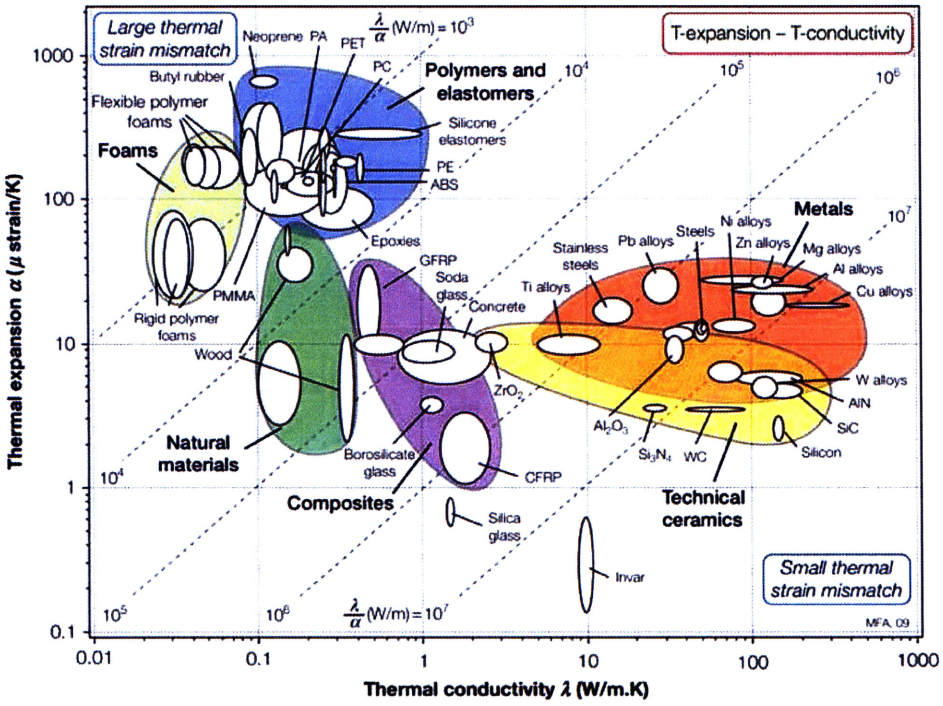

Figure 6-1: Thermal conductivity and coefficient of thermal expansion of various materials [3] Coefficient of thermal expansion (CTE) of engineering metals is in order of 10um/(m·K). Some materials such as Invar have CTE that is an order of magnitude lower than that of the engineering metals.

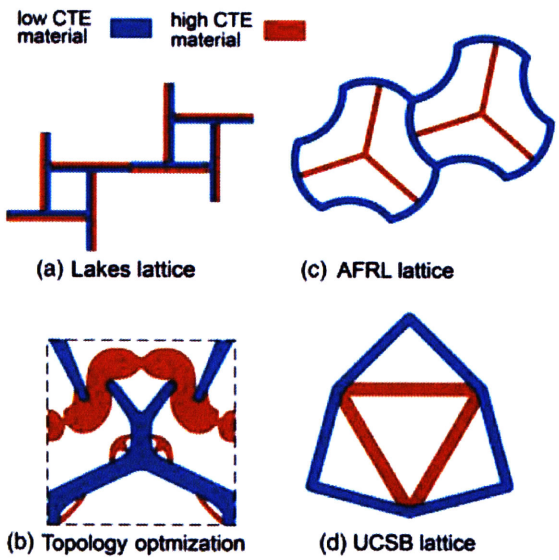

Figure 6-2: Cell/lattice designs of mechanical materials with tunable CTE [4]. Berger et al. suggests that only the UCSB lattice design is transversely isotropic while the other structures have anisotropic properties and desired thermal expansion is achieved only in certain directions.

are made of a combination of materials arranged in smaller blocks or cells. This allows mechanical metamaterials to exhibit bulk properties that are different from those of their constitutive materials. Cell designs of 2D metamaterials developed by several research groups are shown in Figure 6-2. Steeves et al. show that neutral bulk coefficient of thermal expansion of metamaterials can be achieved through a combination of thermal expansion ratio of the constitutive materials and structural design parameters [28]. The cell designs are essential factor in controlling structural behavior of the metamaterials. Berger et al. suggest that only the UCSB lattice design (Figure 6-2 (d)) is transversely isotropic while the other structures have anisotropic properties and desired thermal expansion is achieved only in certain directions [4]. Xu and Pasini suggest that 3D structures that have bend-dominated loading mechanism are structurally inefficient and have lower specific stiffness [29]. To overcome these limitations, they developed 3D stretch-dominated structures with high specific stiffness and tunable CTE, including neutral CTE. However, their work shows that the effective yield strength of the structures is approximately two orders of magnitude lower than

that of the constituent materials. With the limitation on the yield strength, the 3D mechanical metamaterials are not suitable candidate materials as of now.

6.2 Use of Materials with Different Thermal Diffusivity and Coefficient of Thermal Expansion

In this section, materials with different thermal diffusivity and CTE are considered as a substitute material. The thermal expansion mismatch issue in the representative engine is taken as a design example. For the representative engine, the thermal expansion mismatch causes a reduced bearing clearance during the engine start-up and an increased bearing clearance at the steady-state condition. In this design example, the shaft material remains unchanged and only the housing material is subject to change. This material selection process for the housing material can be reapplied for different shaft materials. Two groups of materials are investigated as a substitute for the housing materials.

6.2.1 Materials with Different Thermal Diffusivity and Coefficient of Thermal Expansion

The first group of candidate materials considered is a group of materials with constant thermal conductivity, varying volumetric specific heat capacity (ρc), hence varying thermal diffusivity, and varying CTE. From the reduced order model, changes in CTE and thermal diffusivity of the housing material would lead to changes in only two non-dimensional groups, namely, the ratio of heat diffusivity in the housing to the shaft ($\Pi_1 = \kappa_h/\kappa_s$) and the ratio of CTE of housing material to shaft material ($\Pi_5 = \alpha_h/\alpha_z$). Equations 5.25 suggest that the non-dimensional radial thermal expansion at the steady-state condition of the shaft is not a function of these two parameters and only the non-dimensional radial thermal expansion at the steady-state condition

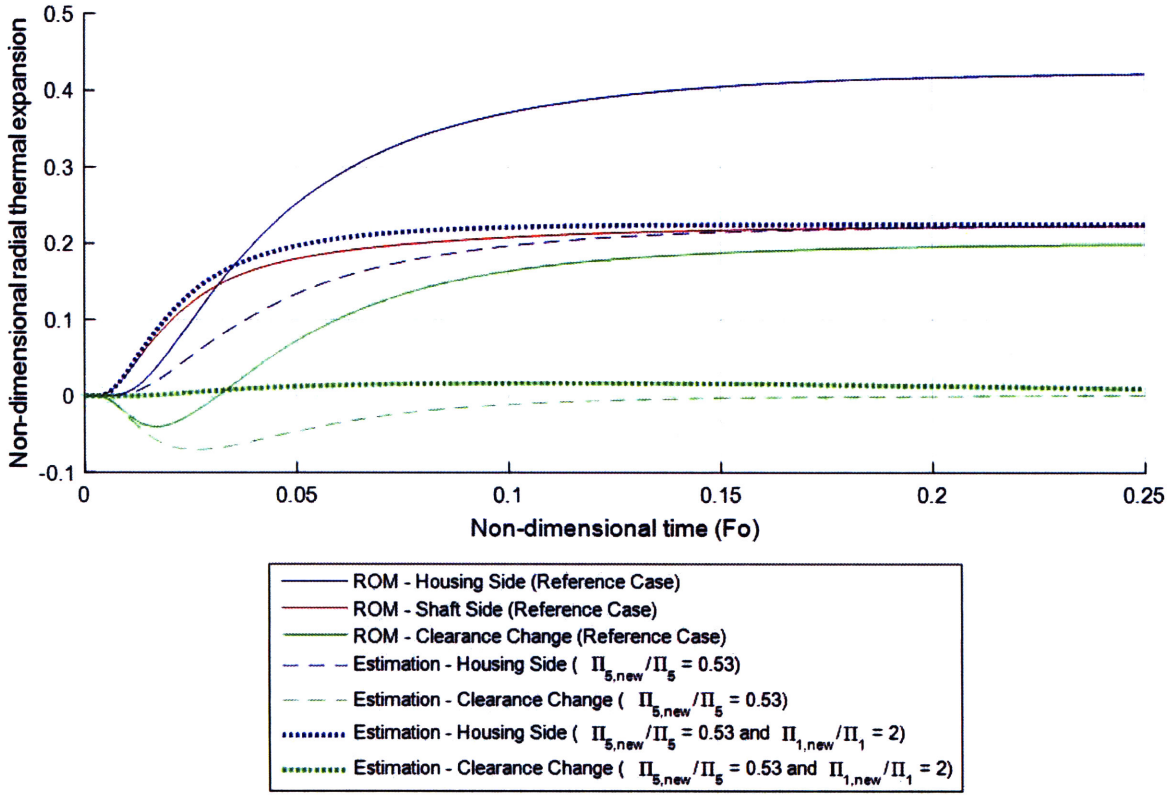

Figure 6-3: Estimated radial thermal expansion of the housing and estimated bearing clearance change at different ratio of thermal diffusivity (Π_1) and ratio of CTE (Π_5). The system with lower CTE ($\Pi_{5,\text{ new}}/\Pi_5 = 0.53$) has a small change in bearing clearance at steady-state but a large reduction in bearing clearance at the start-up process. The system with higher thermal diffusivity ($\Pi_{1,\text{ new}}/\Pi_1 = 2$) and lower CTE ($\Pi_{5,new}/\Pi_5 = 0.53$) does not have the drawback and is able to retain a small clearance variation over time.

of the housing is a function of Π_5. The transient radial thermal expansion during the start-up process is both a function of Π_1 and Π_5. With changes in only two non-dimensional groups, the material selection process is significantly simplified.

The first step in the material selection process is to adjust the radial thermal expansion of the housing at the steady-state condition. In the following example, the new radial thermal expansion of the housing is set to be similar to that of the shaft to minimize the thermal expansion mismatch at the steady-state condition. The new coefficient of thermal expansion of the housing material required in this case is calculated from Equation 6.1. The new ratio of CTE of housing and shaft material

($\Pi_{5,new}$) can be calculated from Equation 6.2. For the design example considered here, $\Pi_{5,\text{ new}}/\Pi_5$ is set to be 0.53. Figure 6-3 shows that ($\Pi_{5,new}$) is able to mitigate the increased bearing clearance at the steady state; however, this results in a larger reduced bearing clearance during the transient process at Fo $\approx$ 0.03.

$$\frac{\alpha_{h,new}}{\alpha_h} = \frac{u^*_{r,h,new}(\chi, \mathcal{R}, Fo \to \infty)}{u^*_{r,h}(\chi, \mathcal{R}, Fo \to \infty)} \tag{6.1}$$

$$\Pi_{5,new} = \Pi_5 \frac{\alpha_{h,new}}{\alpha_h} \tag{6.2}$$

The second step in the selection process is to mitigate the reduced transient bearing clearance by accelerating the radial thermal expansion of the housing during the transient process. It can be seen from Figure 6-3 that the radial thermal expansion of the housing based on the new CTE is smaller than that of the shaft from Fo = 0 to 0.2, resulting in a smaller bearing clearance. To reduce the thermal expansion mismatch during this period, the housing and the shaft should expand at similar rate. Figure 6-3 shows that the housing requires longer time to achieve steady-state temperature than that required by the shaft. Therefore, the thermal response of the housing is accelerated through by increasing thermal diffusivity of the housing material, hence increasing the ratio of heat diffusivity in the housing. The new thermal diffusivity ratio ($\Pi_{1,new}/\Pi_1$) is set to be 2. The effect of accelerated thermal response of the housing can be estimated by rescaling the Fourier number as shown in Equation 6.3.

$$u^*_{r,h,new}(x, \mathcal{R}, Fo) \approx u^*_{r,h}\left(x, \mathcal{R}, Fo \cdot (\Pi_{1,new}/\Pi_1)\right) \tag{6.3}$$

Figure 6-3 shows the estimated response of the housing under the new thermal diffusivity ratio ($\Pi_{1,\text{ new}}$) and the estimated bearing clearance change, which is calculated from the estimated response of the shaft. The estimated bearing clearance change indicates a smaller negative thermal expansion mismatch during the transient process as expected.

In order to confirm this estimate, the reduced order model is utilized to compute

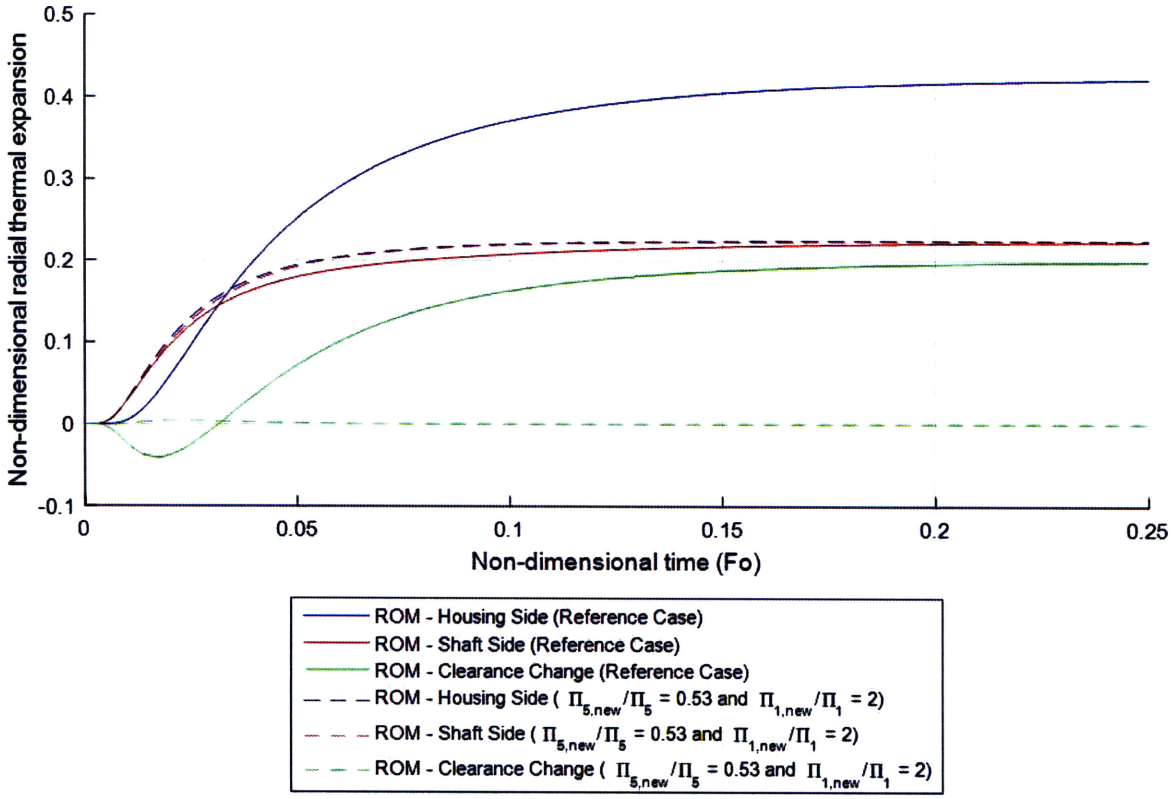

Figure 6-4: Mitigation of the reduced bearing clearance during a start-up process and the increased bearing clearance at the steady-state through higher ratio of thermal diffusivity (Π_1) and lower ratio of CTE (Π_5). The system with higher thermal diffusivity ($\Pi_{1,\text{ new}}/\Pi_1 = 2$) and lower ($\Pi_{5,new}/\Pi_5 = 0.53$) is demonstrated through the reduced order model to be able to retain an insignificant bearing clearance variation over the engine start-up process.

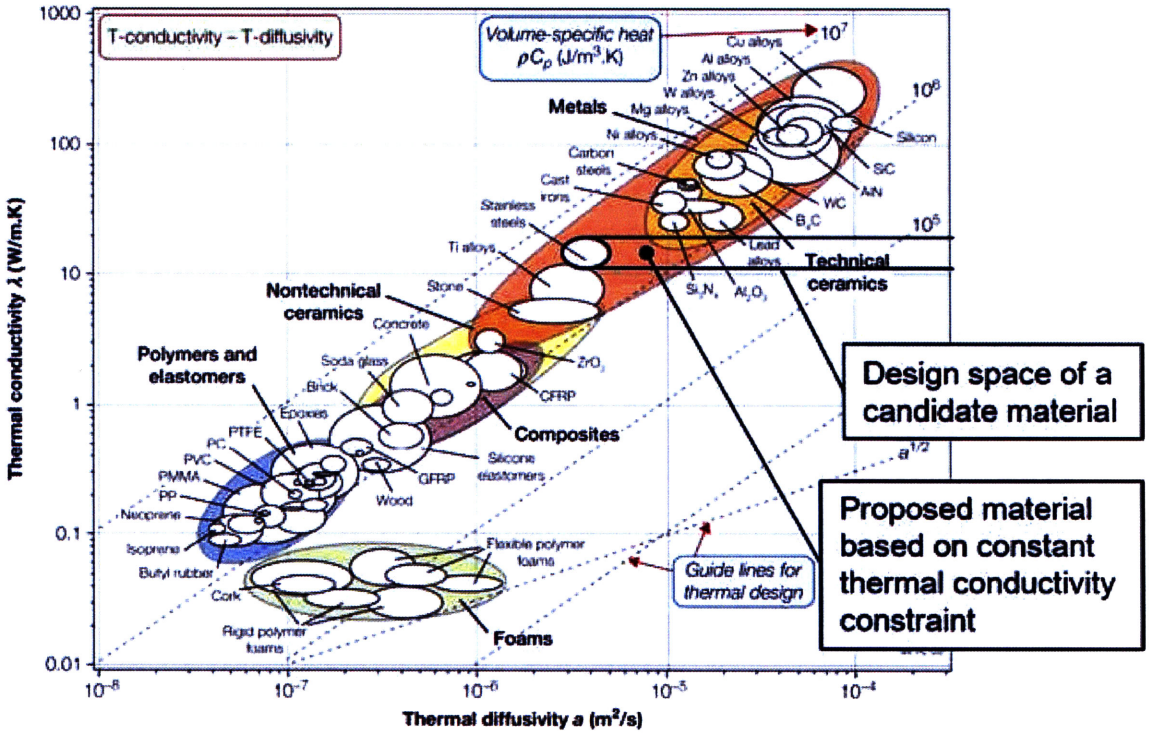

Figure 6-5: Limited selection space of a candidate material with different thermal diffusivity but similar thermal conductivity as that of the original material. For this design example, stainless steel is assumed to be the original material of the housing. There appears to be no conventional group of engineering materials that could be used in the design space (Modifed from Ashby [3]).

the radial thermal response of the shaft and the housing with the new ratio of thermal diffusivity and CTE. Figure 6-4 shows that the new transient thermal expansion mismatch is significantly smaller than the original value as previously estimated through Equation 6.3. This example demonstrates that the reduced transient bearing clearance during the start-up process and the increased bearing clearance during the steady-state can be mitigated through selection of materials with similar thermal conductivity as the original material but different volumetric heat capacity (ρc) (hence varying thermal diffusivity), and different CTE.

Despite the success of this simple material selection process, the main drawback of this process is the availability of the material choices. In this process, the thermal conductivity of the new material is chosen to be the same as that of the previous

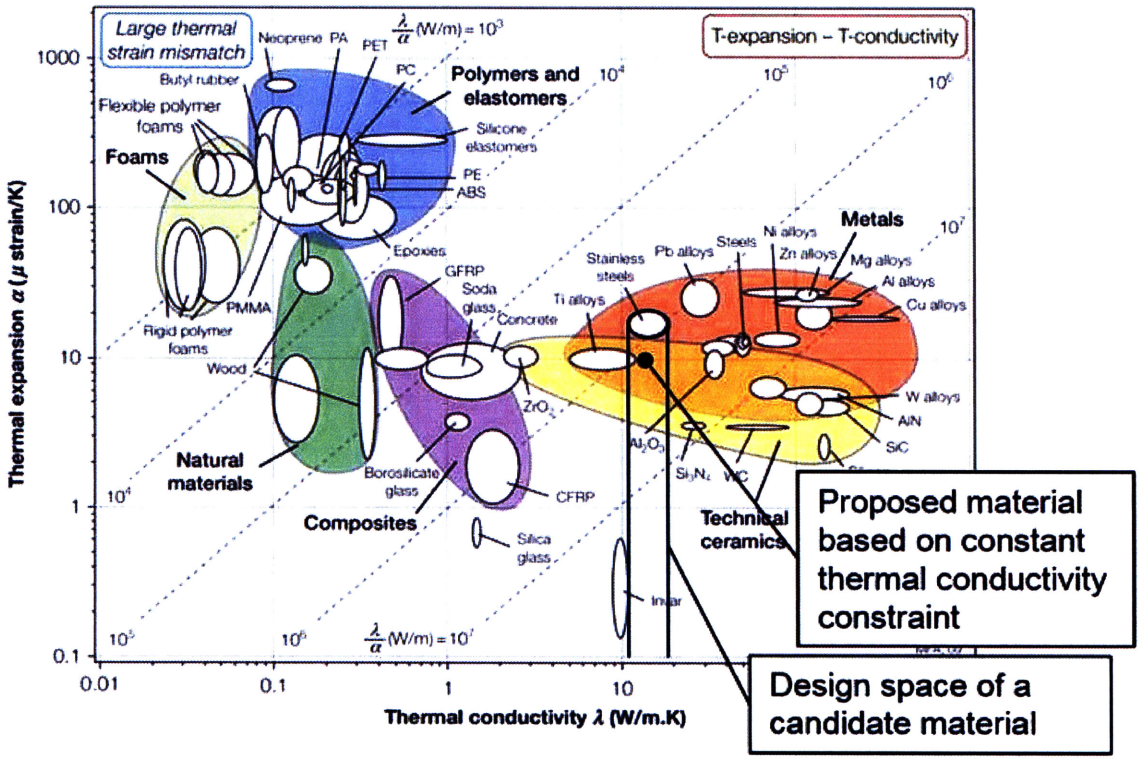

Figure 6-6: Limited selection space of a candidate material with different CTE but similar thermal conductivity as that the original material. For this design example, stainless steel is assumed to be the original material of the housing. There appears to be no conventional group of engineering materials that could be used in the design space (Modifed from Ashby [3]).

material. The adjusted thermal diffusivity is obtained through adjusted volumetric heat capacity. This poses challenges because generally volumetric specific heat of solid materials is approximately $3 \times 10^6\,\mathrm{J/m^3 - K}$ [3]. As a result, the design space of the new material is narrow because of the imposed constraint of the design process. The drawback of this selection process can be demonstrated if original housing were made of stainless steel because the new material must have thermal conductivity similar to that of stainless steel. Figure 6-5 shows the range of possible material diffusivities at constant thermal conductivity. Similarly, Figure 6-6 shows the range of possible material CTE at constant thermal conductivity. It can be seen from these two charts that there is no common group of metals exist in the design space. This introduces a new issue in acquiring the required material because the required material might not be widely available for the application. Despite the drawback of this material selection method, it provides a rough estimated adjustment of the housing material required to mitigate the thermal expansion mismatch issue.

6.2.2 Materials with Different Thermal Conductivity and Coefficient of Thermal Expansion

The second group of candidate materials considered here is materials with volumetric specific heat of $3 \times 10^6\,\mathrm{J/m^3 - K}$ with varying thermal conductivity and CTE. The constraint of the volumetric specific heat is obtained from the general trend of solid materials [3]. Under this constraint, thermal diffusivity of candidate materials varies linearly with its thermal conductivity. This varying thermal diffusivity changes the ratio of thermal diffusivity of the housing material to the shaft material (Π_1). The varying CTE changes the ratio of CTE of the housing material to the shaft material (Π_5). In addition, change in thermal conductivity of the housing material impacts the housing fin parameter $\left(N_s = \sqrt{h_s P_s / k_s A_s} \cdot L_{ref}\right)$ and the ratio of heat conduction in the housing to that in the shaft ($\Pi_4 = k_h A_h / k_s A_s$). In summary, change in thermal conductivity of the housing material at fixed volumetric specific heat results in change in 3 non-dimensional groups, including Π_1, Π_4, and N_s; the change in CTE of the

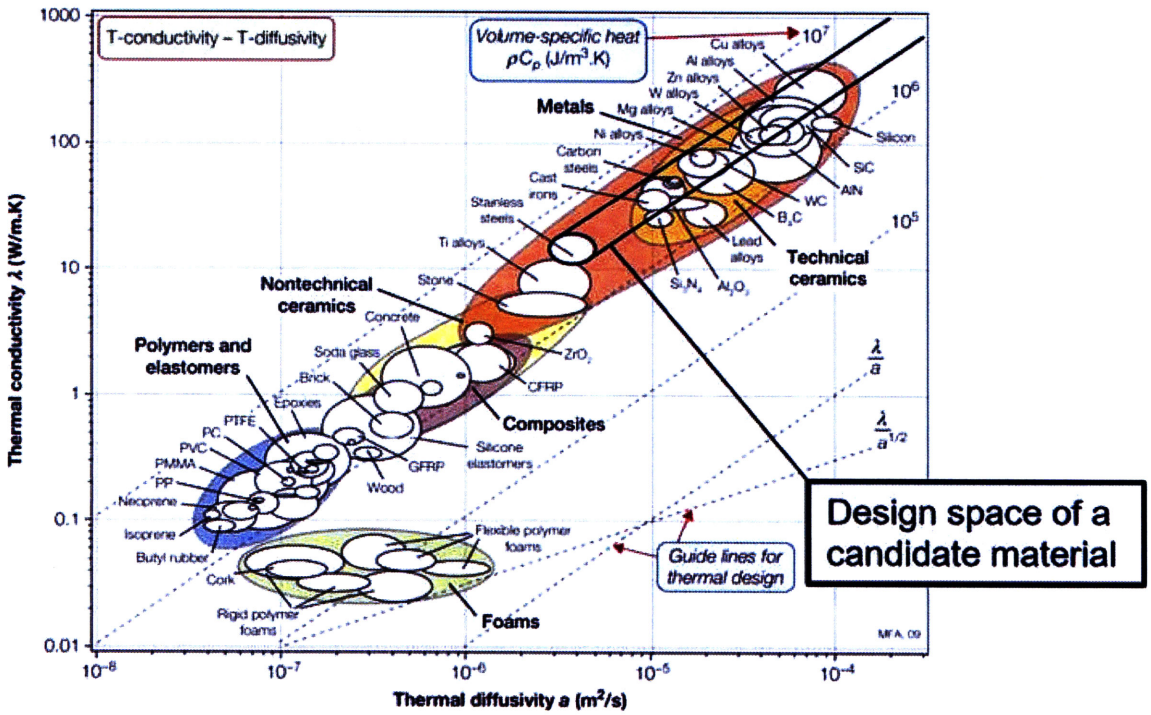

Figure 6-7: Selection space of a candidate material with different thermal conductivity but similar volumetric specific heat (Modifed from Ashby [3]). There are several conventional groups of engineering materials that could be used in the design space.

housing material results in change in Π_5.

For this design example, at the steady-state condition, the original radial thermal expansion of the housing is larger than that of the shaft. To minimize the increased bearing clearance, the CTE of the housing material needs to decrease, resulting in a smaller Π_5. As shown in the previous design example, a smaller Π_5 would cause a more severe reduced bearing clearance during the start-up process. To mitigate the observed reduced bearing clearance, the thermal response of the housing is accelerated with high thermal diffusivity of the housing material, resulting in a larger Π_1. Under the constraint of the volumetric specific heat, the higher thermal diffusivity is achieved through higher thermal conductivity, which leads to larger conduction heat transfer in the housing and an increase in Π_4 and N_s. It can be expected that at the same Π_1 (thermal diffusivity ratio), the required Π_5 (CTE ratio) will be smaller than that in the previous design example due to the fact that the larger conduction heat transfer

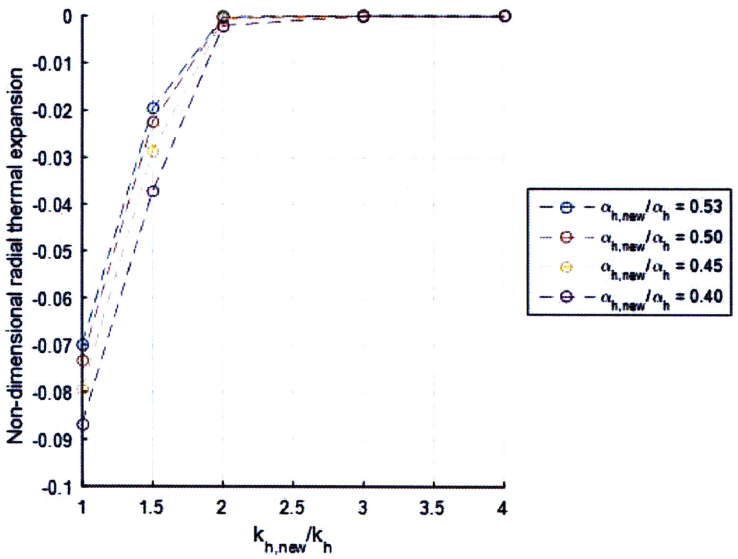

Figure 6-8: Largest negative bearing clearance size change during a start-up process based on candidate housing materials at different thermal conductivity ratio and CTE ratio. The reduced bearing clearance can be mitigated by increasing thermal conductivity and thermal diffusivity of the housing. Systems with lower CTE tend to have a larger reduction in the bearing clearance.

causes higher housing temperature. This intuition sets the limit for the design space of the candidate materials. For this design example, the housing is assumed to be made of stainless steel. Figure 6-7 shows the design space where potential candidates could exist. In this design space, several common materials exist. By contrast, the previous design space shown in Figure 6-5 has limitations in material selection.

The reduced order model is utilized for the parametric study in this example. The thermal conductivity and CTE of the housing are treated as independent inputs while other inputs remain constant. Figure 6-8 and Figure 6-9 show the largest negative bearing clearance size during the start-up process and the bearing clearance size at the steady-state condition, respectively, based on various thermal conductivity and CTE. For transient operation, the reduced bearing clearance can be mitigated by increasing thermal conductivity and thermal diffusivity of the housing. The use low CTE materials could lead to a larger reduction in the bearing clearance. For steady-state operation, the increased bearing clearance can be mitigated by decreasing CTE of the housing. Systems with higher thermal conductivity and thermal diffusivity

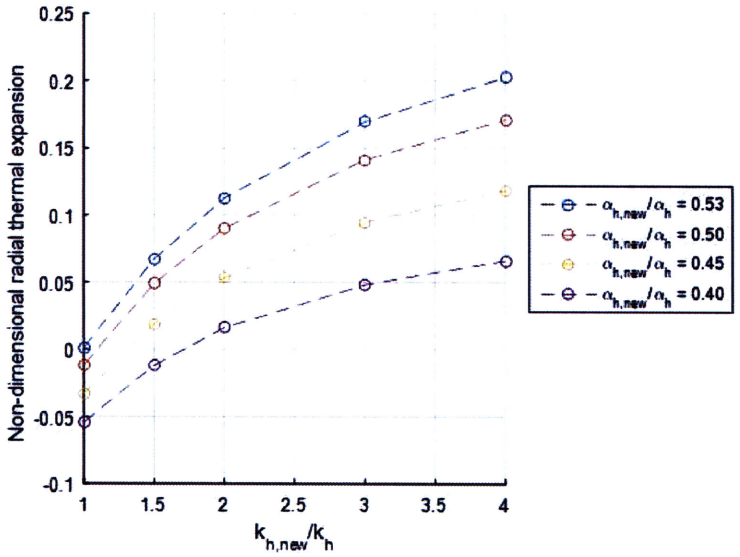

Figure 6-9: Bearing clearance size change at the steady-state condition based on candidate housing materials at different thermal conductivity ratio and CTE ratio. The increased bearing clearance can be mitigated by decreasing CTE of the housing. Systems with higher thermal conductivity and thermal diffusivity tend to have a larger increase in the bearing clearance.

tend to have a larger increase in the bearing clearance. To satisfy both transient and steady-state operation, CTE and thermal conductivity of the housing must be chosen appropriately.

The reduced order model result indicates that use of a candidate material with $k_{h,new}/k_h$ of 2 and $\alpha_{h,new}/\alpha_h$ of 0.4 yields small variation in the bearing clearance during the transient process and the steady-state condition. Figure 6-10 shows this selected candidate material in the material design space and the properties of the material appear to be similar to those of Alumina (Al_2O_3). In summary, the second group of candidate materials with the imposed constraint on volumetric specific heat appears to be satisfactory. The design example demonstrates that adjustment of thermal and structural characteristics through thermal conductivity and CTE of the housing material is adequate to yield a conventional material as the new housing material.

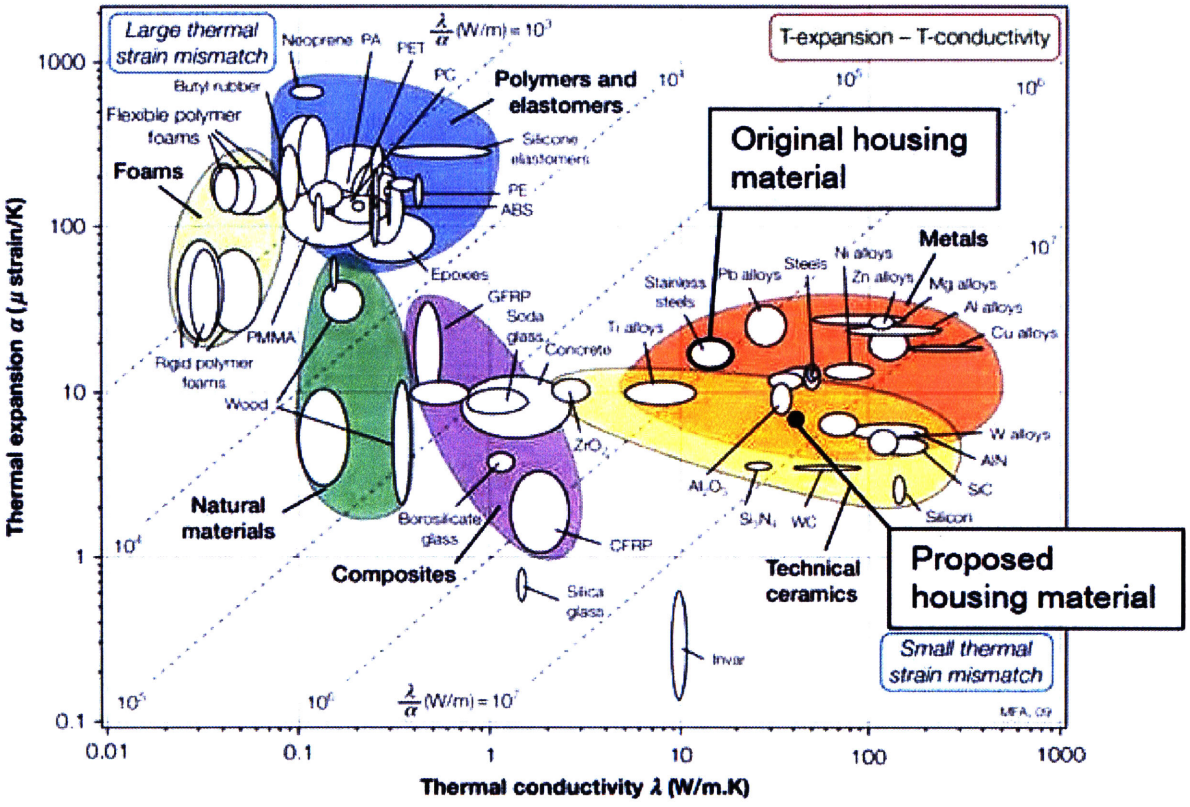

Figure 6-10: The location of the selected candidate material on the material chart. The properties of the selected candidate material are similar to those of Alumina (Al_2O_3). This suggests there could be conventional engineering materials that can be utilized for mitigating the thermal expansion mismatch issue (Modifed from Ashby [3]).

6.3 Summary

Proposed solutions for mitigating differential thermal expansion mismatch are discussed. The thermal expansion mismatch observed in the representative engine is considered as a design example. In this design example, the shaft material remains unchanged and only the housing material is subject to change. The non-dimensional parameters derived from the reduced order model are used as the basis for suggesting various solutions. The focus of the design example is on the selection of the engine materials and not an engine re-design.

One discussed solution is the use of materials with lower CTE such as Invar. The use of Invar could be problematic for a gas turbine application because the maximum operating temperature of Invar (temperature at which Invar retains low coefficient of thermal expansion) is much lower than the operating temperature of a gas turbine. In addition, yield strength of Invar is relatively low compared to commonly used materials such as titanium alloys or nickel-based alloys. This additional complication makes Invar unattractive as a candidate for the material choice. Another approach to obtain materials with low or neutral coefficient of thermal expansion is through the use of mechanical metamaterials. Current research shows that the effective yield strength of the 3D structures is nevertheless approximately two orders of magnitude lower than that of the constituent materials. With the limitation on the yield strength, the 3D mechanical metamaterials are not suitable candidate materials as of now. As a result, materials with different thermal diffusivity and CTE are considered as a substitute material. Two groups of materials are investigated as a substitute for the housing materials.

The first group of candidate materials considered is a group of materials with constant thermal conductivity, varying volumetric specific heat capacity, hence varying thermal diffusivity, and varying CTE. From the reduced order model, changes in CTE and thermal diffusivity of the housing material would lead to changes in only two non-dimensional groups, namely, the ratio of heat diffusivity in the housing to the shaft (Π_1) and the ratio of CTE of housing material to shaft material (Π_5). With changes

in only two non-dimensional groups, the material selection process is significantly simplified. The first step in the material selection process is to adjust the radial thermal expansion of the housing at the steady-steady state condition. The second step in the selection process is to mitigate the reduced transient bearing clearance by accelerating the radial thermal expansion of the housing during the transient process. The reduced order model result demonstrates that the reduced transient bearing clearance during the start-up process and the increased bearing clearance during the steady-state are mitigated as proposed. Despite the success of this simple material selection process, the main drawback of this process is the availability of the material choices. The adjusted thermal diffusivity is obtained through adjusted volumetric heat capacity. This poses challenges because generally volumetric specific heat of solid materials is approximately $3 \times 10^6\ \mathrm{J/m^3 - K}$ [3]. As a result, the design space of the new material is narrow because of the imposed constraint of the design process.

The second group of candidate materials considered here is materials with volumetric specific heat of $3 \times 10^6\ \mathrm{J/m^3 - K}$ with varying thermal conductivity and CTE. Under this constraint, thermal diffusivity of candidate materials varies linearly with its thermal conductivity. This varying thermal diffusivity changes the ratio of thermal diffusivity of the housing material to the shaft material (Π_1). The varying CTE changes the ratio of CTE of the housing material to the shaft material (Π_5). In addition, change in thermal conductivity of the housing material impacts the housing fin parameter $\left(N_s = \sqrt{h_s P_s / k_s A_s} \cdot L_{ref}\right)$ and the ratio of heat conduction in the housing to that in the shaft ($\Pi_4 = k_h A_h / k_s A_s$). The reduced model is utilized for the parametric study in this example. The reduced order model result indicates there is a material that can yield small variation in the bearing clearance during the transient process and the steady-state condition. The properties of the selected material appear to be similar to those of common materials.

In summary, the design example demonstrates that adjustment of thermal and structural characteristics through thermal conductivity and CTE of the housing material is adequate to yield a conventional material as the new housing material.

Chapter 7

Summary and Future Work

This chapter summarizes the objectives of the research and the research approach utilized to answer the research questions. It also includes the key research findings and recommendations for the future work.

7.1 Objectives and Approach

The overall goal of the research is to assess the impact of aero-thermal-mechanical interactions of micro gas turbines related to operations of gas bearings. This is motivated by the experimental observation that sustainable operation is limited by the shaft-bearing housing system that impact the engine operability; it is hypothesized that this is due to thermal-induced mechanical deformation of shaft-bearing housing that results in vanishing bearing clearance distribution. The research platform consists of a representative micro gas turbine engine that has a single shaft with a single stage centrifugal compressor and radial inflow turbine. These characteristics are shared with many micro gas turbines under development.

Computational approaches are proposed as the main tool for determining the cooling flow field and the operation of the engine. Three-dimensional URANS with a conjugate heat transfer (CHT) module has been used as the main thermal-fluid computational tool. The thermal-structural model used in this research will be a

one-way couple model of 3D CFD and a 3D finite element solver. The structural aspect of the engine and its implication on the thermal expansion mismatch has been analyzed based on a structural model with boundary conditions set by CFD computations. Reduced order model has been formulated with key physics governing the thermal aspects of the engine system. The reduced order model can be used for trade-off studies, assessing thermal management system design and development, and exploration of a design space.

7.2 Key Findings

The answers to the research questions are enumerated below:

1. A first of a kind of computational model consisting of the use of 3D URANS coupled with conjugate heat transfer and finite element method has been formulated to determine: (1) fluid flow and heat flow in the entire engine system from the engine start-up to the steady-state operation and (2) the corresponding engine component mechanical response that include structural deformation and stress distribution. An unsteady CFD conjugate heat transfer computation of flow and temperature distribution in the entire engine system is first implemented for engine startup to steady state operation; this is then followed by determining the corresponding mechanical deformation of engine components based on finite element analysis.

2. The hypothesis that thermal-induced mechanical deformation of shaft-bearing housing system limiting sustainable operation of the representative micro gas turbine engine is proven. The computed result demonstrates the temporal evolution of the thermal expansion mismatch between the shaft and the bearing housing from the start-up toward the steady-state condition. At the beginning of the engine start-up process, radial expansion of the shaft is larger than that of the bearing housing at any axial location, resulting in a smaller bearing clearance at any axial location. At the end of the start-up process, the computed

trend (in the radial expansion of shaft and bearing housing) reverses so that there is indeed an increase in bearing clearance.

3. A reduced order model consisting of conduction heat transfer and convection heat transfer as set by the solid structures and cooling flow is formulated. Reduced-order model results are in good accord with transient results from the CFD and FE model. The reduced order framework as well as its use for identifying characterizing parameters and formulation of scaling rule can be generalized for assessing thermal-induced mechanical response of other engine components such as turbomachinery tip clearances and mechanical seal system. The reduced order model provides an enabler to determine the critical Fourier number (i.e. the time instant) for the occurrence of minimum bearing clearance and a mean to develop a strategy for controlling bearing clearance under the bearing operating envelope. In addition, the reduced order model is used to formulate an approximate scaling rule of thermal-induced shaft-bearing housing clearance variation in engine of various sizing.

4. The non-dimensional parameters are categorized in 7 groups: (1) 3 non-dimensional temperatures, (2) 2 non-dimensional structural thermal expansions, (3) 2 non-dimensional location parameters, (4) 1 non-dimensional time parameter, (5) 9 non-dimensional geometric parameters, (6) 6 non-dimensional thermal parameters, and (7) 1 non-dimensional structural parameter. The non-dimensional thermal parameters consist of: (1) shaft fin parameter, (2) housing fin parameter, (3) ratio of heat diffusivity of housing to that of shaft, (4) ratio of energy storage in cooling flow to that in shaft, (5) ratio of advection in fluid to heat diffusion in shaft, (6) ratio of heat conduction in housing to that in shaft. The only controlling structural parameter is the ratio of coefficient of thermal expansion of the housing to that of the shaft. The non-dimensional parameters serve as a guideline for selecting shaft and bearing housing materials with appropriate properties as well as tailoring the coolant flow to limit and control the variation in the bearing clearance during the transient process and the steady-state

condition.

5. Proposed solutions for mitigating differential thermal expansion mismatch are discussed. The non-dimensional parameters derived from the reduced order model are used as the basis for suggesting various solutions. Materials with varying thermal conductivity and CTE are shown to be effective in providing small variation in the bearing clearance during the transient process and the steady-state condition. The adjusted CTE essentially mitigates the radial thermal expansion of the housing at the steady-state condition. The adjusted thermal conductivity essentially mitigates the reduced transient bearing clearance by accelerating the radial thermal expansion of the housing during the transient process.

7.3 Future work

1. Mechanical metamaterials could be promising solutions to the thermal expansion mismatch issue in the future. Developments and manufacturability of mechanical metamaterials with properties that are not available in traditional materials (e.g. low volumetric specific heat, coefficient of thermal expansion, etc.) are expected to be feasible in the near future.

2. 3-D stretch-dominated mechanical metamaterials might be used in futuristic gas turbine engines. For their application in a gas turbine, bulk mechanical properties of 3-D Stretch-dominated mechanical metamaterials should be evaluated under non-uniform and elevated temperature conditions, and rotational effects. A novel gas turbine engine design should be investigated based on this mechanical metamaterials to overcome the low effective strength of the materials through their low effective density.

3. The computational framework can be applied to assessment of thermal-mechanical response of a mechanical seal system in micro gas turbine engines. Proper

control of changes in clearances of mechanical seals should reduce seal leakage flow, thus reducing losses in the engine cycle.

Appendix A

Root Cause Analysis on Sources of the Operability Issues

The goal is of this appendix is to provide rationales used in formulating a hypothesis on sources of the operability issues and essential heat transfer processes in the engine. The operability issues are assumed to be caused by the thermal expansion mismatch, which is presented in Chapter 4. The essential heat transfer processes assessed in this analysis are perceived as necessary heat transfer processes that can cause the thermal expansion mismatch in the engine under both transient and steady-state operation.

The approach for assessment of the sources of the operability issues begins with categorizing the operability issues into the transient operability issue and the steady-state operability issue as shown in Figure A-1. As previously discussed in Chapter 4, the transient operability issue is thermal rubbing between the bearing and the shaft. This thermal rubbing occurs when the initial clearance size is set to be too small and the bearing clearance vanishes during the start-up process of the engine. The operability issue during high-speed steady-state operation is whirl instability. The whirl instability can occur when the bearing clearance size is too large. It is shown by the CFD and FE simulation that the bearing clearance size increases from the initial clearance in the representative engine.

The sources of the operability issues are separated into mechanical-induced and

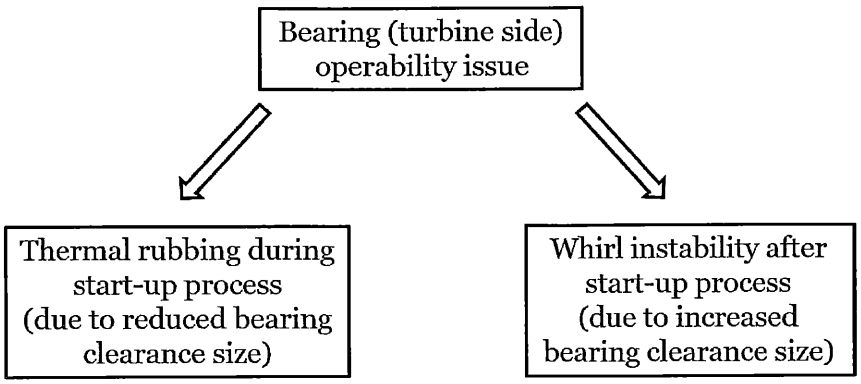

Figure A-1: Transient and steady-state operability due to variation of bearing clearance size.

thermal-induced mechanisms for both transient issue (reduced bearing clearance) and steady-state operability issue (increased bearing clearance). Then mechanisms that could introduce lead to changes in bearing size are listed out. Relative importance of these mechanisms will be discussed and their contribution to the overall problem will be assessed. For thermal-induced mechanics, a control volume analysis is used as a basis for the analysis for estimating temperature change of the component during the transient operation and for estimating steady-state temperature during steady-state operation. The control volume analysis is not meant to provide an exact answer but to rather suggest relative importance of each heat transfer processes. In addition, computed results from CFD and FE and experimental results will be used to provide quantitative supporting data.

The analysis begins on the transient operability issue (thermal rubbing). Figure A-2 shows breakdown of the transient operability issue into mechanical-induced (mechanical strain) and thermal-induced (thermal strain) mechanisms. Under this condition, radial expansion of the shaft outgrows radial expansion of the bearing to the extent that the bearing clearance vanishes. The expansion mismatch between the shaft and the housing could be caused by either mechanical strain or thermal strain. The effect of mechanical strain is discussed first. The shaft can expand radially when it rotates at high speed due to centrifugal body force. Chapter 4 suggests that the radial expansion of the shaft due to the centrifugal effect is estimated to be approximately 10% of the

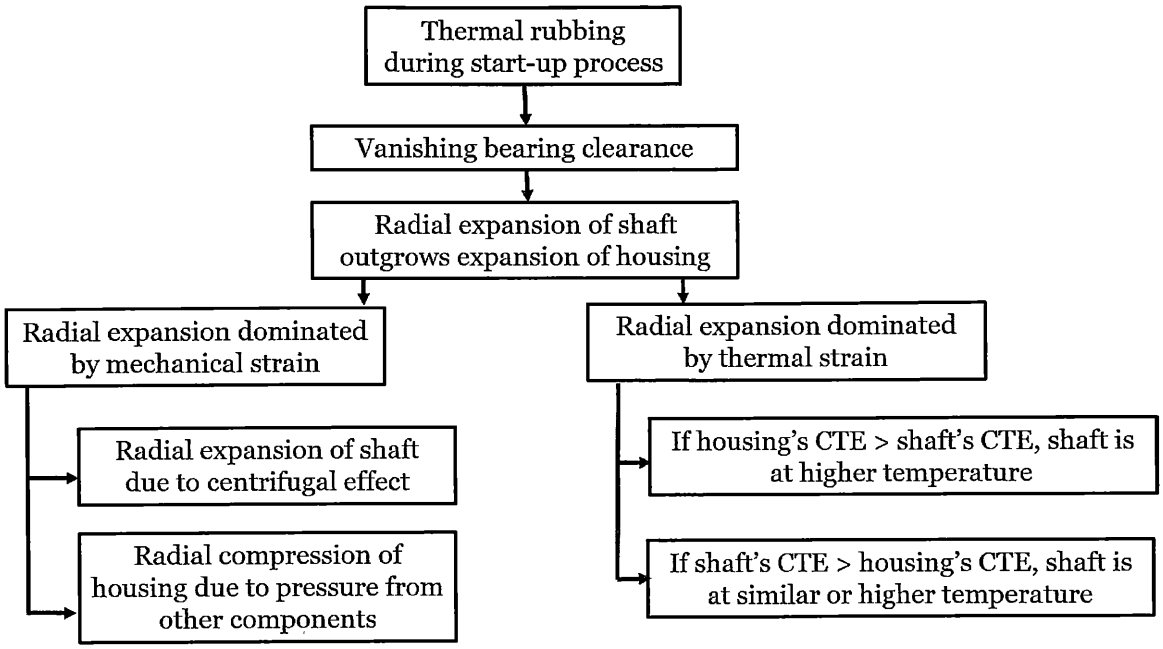

Figure A-2: Breakdown of possible mechanisms introducing transient operability issue into mechanical-induced and thermal-induced mechanisms.

total radial expansion. An order of magnitude analysis (not shown here) that is carried out based on operating speed of the shaft and estimated shaft temperature confirms the finding from Chapter 4 as well. This suggests that the radial expansion of the shaft due to centrifugal effect is less important than the effect of thermal-induced expansion.

The next possible source of the radial expansion mismatch due to mechanical strain is from radial compression of housing due to pressure from other components. There could be pressure of the compressed air in the main flow path, acting on the turbine bearing housing. Quantifying the extent of this effect is challenging as it depends on the load distribution design of the engine. However, it could be argued that if this effect is significant, the bearing clearance should be a function of the pressure in the main flow path as mechanical response is much faster than thermal response of the engine. The pressure of compressed air in the main flow path can build up rapidly when the engine speed increases but the vanishing bearing clearance size does not occur when the pressure builds up. The implication is that the effect of pressure in the main flow path on the bearing housing is not one of the

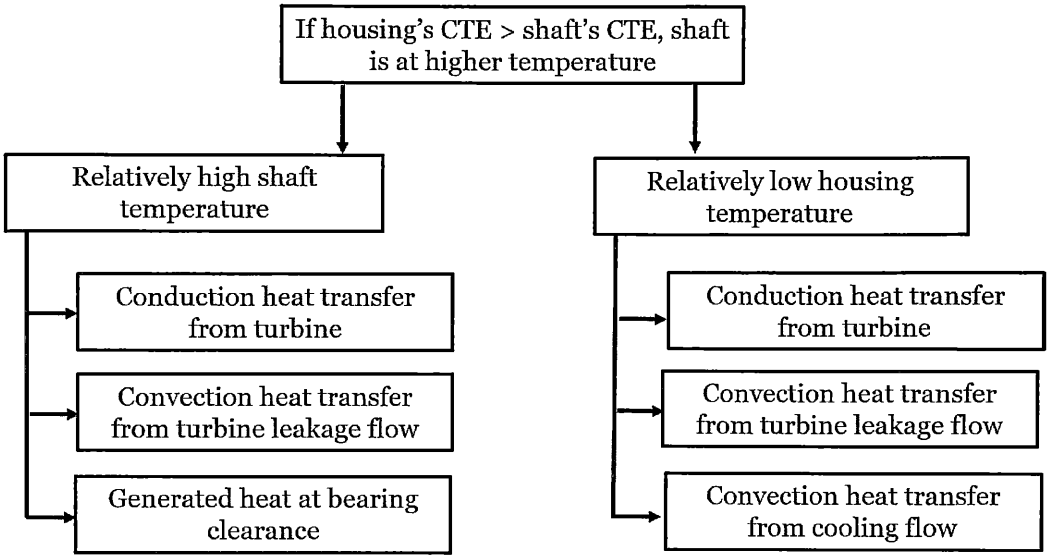

Figure A-3: Breakdown of thermal-induced heat transfer mechanisms that cause shaft temperature to be higher than housing temperature. Several heat transfer process candidates are listed.

key mechanisms, which causes vanishing bearing clearance. As a result, effects of mechanical strain during the transient operation are estimated to be limited and will not be considered in the reduced order model. Thus, it can be inferred that effects of thermal strain or thermal-induced expansion must be the key mechanism for the transient operability issue.

For thermal-induced expansion, coefficient of thermal expansion (CTE) of materials can play a role in setting the thermal expansion. A scenario in which thermal expansion of the shaft is larger than that of the housing is discussed. Based on an assumption that the radius of the shaft and housing is similar at the bearing location, if CTE of the housing material is higher than that of the shaft, the shaft should be at higher temperature than the housing. However, if CTE of the shaft is larger than CTE of the housing, the shaft temperature can be similar or higher than the housing temperature. For the representative engine, CTE of the housing is higher than that of the shaft and this scenario will be explored further.

For this scenario, possible causes of relative high shaft temperature and low housing temperature are discussed. Figure A-3 shows breakdown of thermal-induced

heat transfer mechanisms that could responsible for the scenario. A control volume analysis is applied for a small section of the shaft and the housing near the bearing location. Temperature of the shaft is controlled by conduction heat transfer from the turbine, convection heat transfer from hot turbine leakage flow, and heat transfer generated at bearing clearance. The conservation of energy of the shaft is as follows

$$m_{\text{shaft}} c \frac{dT}{dt} = \dot{Q}_{\text{cond,turbine}} + \dot{Q}_{\text{conv,leakageflow}} + \dot{Q}_{\text{gen,bearing}}.$$

The conduction heat transfer from the turbine is one potential key source of heat transfer to the bearing location on the shaft side as it is demonstrated by the CFD result in Chapter 4. Based on the CFD result, the convection heat transfer from the hot turbine leakage flow is unlikely to have a direct significant effect near the bearing location at the current engine operation condition. The CFD result suggests that the cooling flow able to prevent the leakage flow from reaching the bearing location. The heat transfer generated at the bearing clearance could also be another key source of heat transfer to the bearing location as well. This generated heat is due to viscous heating at the small bearing clearance between the top foil and the shaft surface. The heat transfer path of the generated heat from the small clearance to the housing side includes heat transfer through bump foils, which acts as a fin and helps dissipate generated heat through the cooling flow. Therefore, it is assumed that in the worst case scenario, all the generated heat is absorbed by the shaft. At this stage, the conduction heat transfer from the turbine and the generated heat from the bearing could both be key mechanisms controlling transient thermal-induced expansion.

On the housing side, the temperature of the housing is controlled by conduction heat transfer from the turbine, convection heat transfer from hot turbine leakage flow, and convection heat transfer from the cooling flow. The conservation of energy of the housing is as follows

$$m_{housing} c \frac{dT}{dt} = \dot{Q}_{\text{cond,turbine}} + \dot{Q}_{\text{conv, leakage flow}} - \dot{Q}_{\text{conv,cooling flow}}.$$

The conduction heat transfer from the turbine is one potential key source of

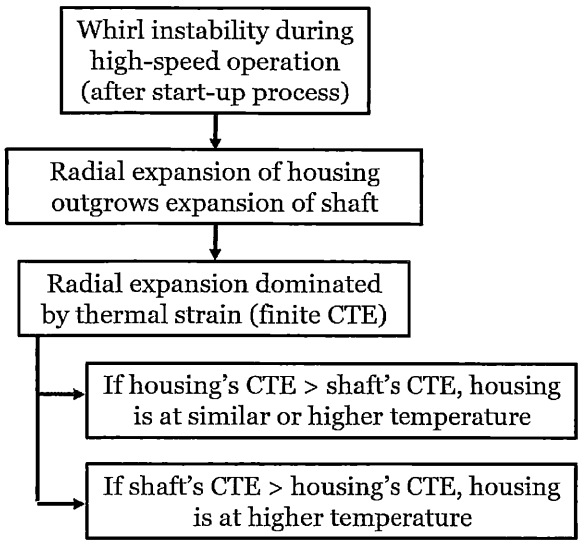

Figure A-4: Breakdown of possible mechanisms introducing stead-state operability issue into thermal-induced mechanisms.

heat transfer to the bearing location on the housing side as it is shown by the CFD simulation result in Chapter 4. Similar to the shaft side, the convection heat transfer from the hot turbine leakage flow is unlikely to have a direct significant impact on the housing due to the same reason. The convection heat transfer from the cooling flow acts to reduce the net heat transfer rate into the housing. It would help retain the temperature of the housing relatively lower than the temperature of the shaft. For this reason, it is proposed as one of the main mechanism controlling the thermal-induced expansion of the housing during the transient operation.

For the steady-state operation, radial expansion of the housing outgrows radial expansion of the shaft to the extent that the bearing clearance vanishes. Figure A-4 shows that the expansion mismatch between the shaft and the housing is proposed to be caused by only thermal strain. Mechanical strain is not considered in this scenario because there could be pressure that push the engine structures radially inward but there appears to be no pressure forces that could pull the engine structures and the bearing housing radially outward. Regarding the thermal-induced effect, a scenario in which thermal expansion of the housing is larger than that of the housing is discussed. Based on the assumption that the radius of the shaft and housing is similar at the

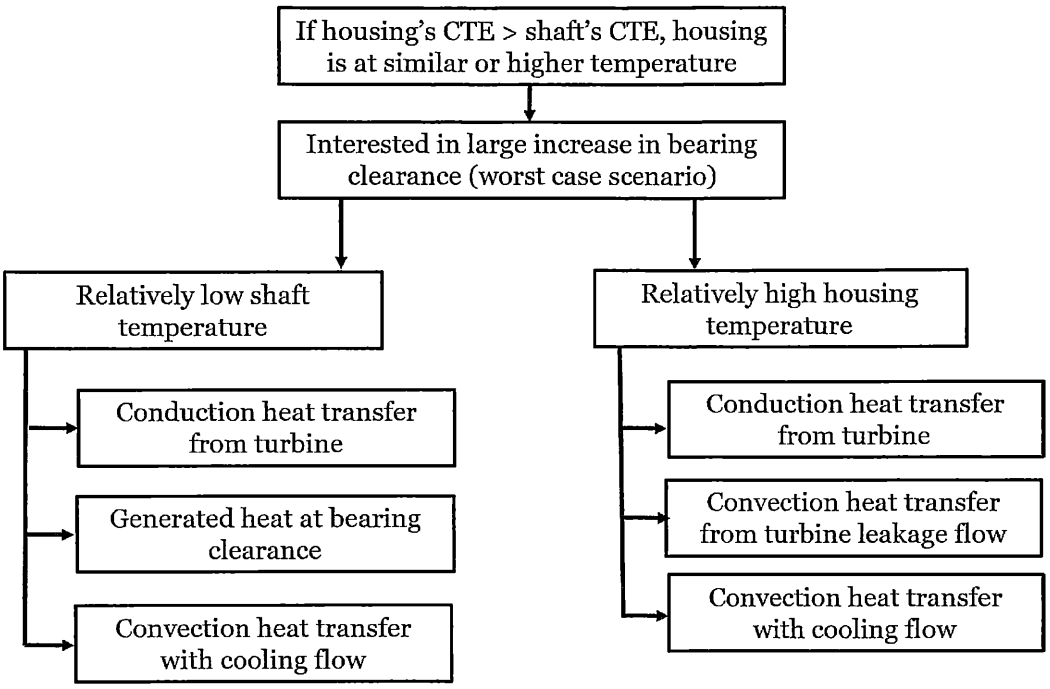

Figure A-5: Breakdown of thermal-induced heat transfer mechanisms that cause shaft temperature to be higher than housing temperature. Several heat transfer process candidates are listed.

bearing location, if CTE of the housing material is higher than that of the shaft, the housing should be at similar or higher temperature than the shaft. However, if CTE of the housing is larger than CTE of the shaft, the housing temperature needs to be higher than the shaft temperature. For the representative engine, CTE of the housing is higher than that of the shaft and this scenario will be explored further.

While it is technically possible that the thermal expansion of the housing is larger than that of the shaft based on similar temperature on the shaft and the housing side, the worst scenario (i.e. largest increase in bearing clearance) occurs when the housing temperature is larger than the shaft temperature. This worst case scenario will be focused in this analysis.

Breakdown of possible heat transfer processes contributing to this scenario is shown in Figure A-5. Under state-state condition, there must be heating and cooling heat transfer processes for energy balance. The conservation of energy of the shaft is

as follows

$$0 = \dot{Q}_{\text{cond,turbine}} + \dot{Q}_{\text{gen,bearing}} - \dot{Q}_{\text{conv,cooling flow}}.$$

The convection heat transfer can be approximated with thermal resistance as

$$0 = \dot{Q}_{\text{cond,turbine}} + \dot{Q}_{\text{gen, bearing}} - \frac{T_{\text{shaft}} - T_{\infty}}{R_{\text{conv}}}.$$

Shaft temperature is estimated from

$$T_{\text{shaft}} = T_{\infty} + \left(\dot{Q}_{\text{cond,turbine}} + \dot{Q}_{\text{gen,bearing}}\right) R_{\text{conv}}.$$

It can be seen that small thermal resistance of convection heat transfer is required in order to have low shaft temperature. Since the convection heat transfer with the cooling flow is the only cooling mechanism, it is proposed as one of the main heat transfer mechanism. The relative importance of conduction heat transfer and generated heat from the bearing as the key heating mechanism is assessed next. The conduction heat transfer rate under steady-state operation can be quantified from the CFD result. The generated heat transfer rate due to viscous heating the bearing clearance is estimated from Coutette flow as

$$\dot{Q}_{\text{gen,bearing}} = \frac{2\pi\omega^2 r_i^3 l}{c},$$

where $\dot{Q}_{\text{gen,bearing}}$ denotes the generated heat, ω the rotating speed, r_i the inner radius of the bearing clearance, l the bearing length, and c the bearing clearance.

The generated heat is estimated under normal operation conditions with the approximate bearing geometry and the engine operating speed. For the representative engine, the ratio of the generated heat to the conduction heat transfer is approximately 0.3. It should be noted that this ratio is obtained under the assumption that all generated heat from the bearing is absorbed by the shaft; this assumption provides the upper limit of the effect of the generated heat. The ratio of the two heat transfer

processes suggests that the generated heat has a smaller impact of temperature of the shaft. As a result, the conduction heat transfer is proposed as the key main heating heat transfer mechanism for the shaft.

The last part of the analysis is the temperature of the housing under steady-state operation, the conservation of energy of the housing is as follows.

$$0 = \dot{Q}_{\text{cond,turbine}} + \dot{Q}_{\text{conv, leakage flow}} - \dot{Q}_{\text{conv,cooling flow}}.$$

While the convection heat transfer due to the hot leakage flow from the turbine acts as a heating process for the housing, it is unlikely to have a significant effect. The CFD result suggests that the cooling flow is able to prevent the hot leakage flow from reaching the bearing housing. As a result, this heat transfer process is deemed to be insignificant at the current operating condition of the engine. The two remaining heat transfers, the conduction heat transfer from the turbine and the convection heat transfer, are heating and cooling mechanisms, respectively. They are both required for controlling steady-state temperature during engine operation and are proposed as key heat transfer mechanisms controlling the housing temperature during steady-state operation.

In summary, the key heat transfer processes are identified for development of the reduced order model. The identification process starts from several heat transfer process candidates. A control volume analysis and the CFD result are used as supplement data for suggesting relative impacts of the candidates. The key heat transfer processes, which govern temperature of the shaft and the housing during both transient and steady-state operation, are the conduction heat transfer from the turbine and the convection heat transfer with the cooling flow. These two key heat transfer processes will serve as the hypothesis on the source of the operability issue for the reduced order model development.

Bibliography

[1] Shuji Tanaka, Kousuke Hikichi, Shinichi Togo, Motohide Murayama, Yasuo Hirose, Takashi Sakurai, Saburo Yuasa, Susumu Teramoto, Takafusa Niino, Takahiro Mori, and Others. World's smallest gas turbine establishing Brayton cycle. *Technical Digest PowerMEMS 2007*, pages 359–362, 2007.

[2] Donghyun Lee, Hyungsoo Lim, Bumseog Choi, Byungok Kim, Junyoung Park, and Jesung Bang. Thermal Behavior of Radial Foil Bearings Supporting an Oil-Free Gas Turbine: Design of the Cooling Flow Passage and Modeling of the Thermal System. *Journal of Engineering for Gas Turbines and Power*, 139(6):061902, jun 2017.

[3] Michael Ashby. *Materials selection in mechanical design: Fourth edition.* 2010.

[4] Hang Xu and Damiano Pasini. Structurally Efficient Three-dimensional Metamaterials with Controllable Thermal Expansion. *Scientific Reports*, 6(1):34924, dec 2016.

[5] Mingming Ma, Xin Yu, and Tao Chen. New progress of high-efficiency and low-emission 9HA combine cycle gas turbine power generation demonstration project. *Journal of Renewable and Sustainable Energy*, 7(4):041514, jul 2015.

[6] Alan H Epstein. Millimeter-Scale, Micro-Electro-Mechanical Systems Gas Turbine Engines. *Journal of Engineering for Gas Turbines and Power*, 126(2):205–226, apr 2004.

[7] Michael Vick, Trent Young, Matthew Kelly, Steven Tuttle, and Katherine Hinnant. A Simple Recuperated Ceramic Microturbine: Design Concept, Cycle Analysis, and Recuperator Component Prototype Tests. In *Volume 8: Microturbines, Turbochargers and Small Turbomachines; Steam Turbines*, page V008T23A030. American Society of Mechanical Engineers, jun 2016.

[8] Marco Antnio Rosa do Nascimento, Lucilene De, Eraldo Cruz dos Santos, Eli Eber Batista Gomes, Fagner Luis Goulart, Elkin Ivn Gutirrez Velsques, and Rubn Alexis Miranda. Micro Gas Turbine Engine: A Review. In *Progress in Gas Turbine Performance*, pages 107–142. InTech, jun 2013.

[9] Jeffrey Armstrong, Christopher Bolin, Mohammed Ebrahim, and Michael Carney. Development and Testing of a 333 Kilowatt Industrial Gas Turbine.

In *Volume 8: Microturbines, Turbochargers and Small Turbomachines; Steam Turbines*, page V008T23A032. American Society of Mechanical Engineers, jun 2016.

[10] Yoji Okita and Shigemichi Yamawaki. Conjugate Heat Transfer Analysis of Turbine Rotor-Stator System. In *Volume 3: Turbo Expo 2002, Parts A and B*, volume 221, pages 1103–1113. ASMEDC, jan 2002.

[11] Jeong Min Seo, Jun Young Park, and Bum Seog Choi. Start-up and Self-sustain Test of 500 W Ultra-Micro Gas Turbine Generator. *Journal of Physics: Conference Series*, 476(1):012060, dec 2013.

[12] W. P. J. Visser, S. Shakariyants, M. T. L. de Later, A. Haj Ayed, and K Kusterer. Performance Optimization of a 3kW Microturbine for CHP Applications. In *Volume 5: Manufacturing Materials and Metallurgy; Marine; Microturbines and Small Turbomachinery; Supercritical CO2 Power Cycles*, pages 619–628. American Society of Mechanical Engineers, jun 2012.

[13] Elliott Bryner, David Ransom, John Bishop, Shane Coogan, and Grant Musgrove. Design of a Small Scale Gas Turbine for a Hybrid Propulsion System. In *Volume 8: Microturbines, Turbochargers and Small Turbomachines; Steam Turbines*, page V008T23A011. American Society of Mechanical Engineers, jun 2015.

[14] Aki Grönman, Juha Honkatukia, Petri Sallinen, Jari Backman, Antti Uusitalo, Teemu Turunen-Saaresti, and Ahti Jaatinen-Värri. Design and Performance Measurements of a 6 kW High-Speed Micro Gas Turbine Prototype. In *Volume 8: Microturbines, Turbochargers and Small Turbomachines; Steam Turbines*, page V008T23A005. American Society of Mechanical Engineers, jun 2015.

[15] Kousuke Isomura, Motohide Murayama, Hiroshi Yamaguchi, Nobuaki Ijichi, Nobuyoshi Saji, Osamu Shiga, Katsuyoshi Takahashi, Shuji Tanaka, Takashi Genda, and Masayoshi Esashi. Development of Micro-Turbo Charger and Micro-Combustor as Feasibility Studies of Three-Dimensional Gas Turbine at Micro-Scale. In *Volume 3: Turbo Expo 2003*, pages 685–690. ASMEDC, jan 2003.

[16] O. Dessornes, S. Landais, R. Valle, A. Fourmaux, S. Burguburu, C. Zwyssig, and Z. Kozanecki. Advances in the Development of a Microturbine Engine. *Journal of Engineering for Gas Turbines and Power*, 136(7):071201, jul 2014.

[17] Jeong Min Seo, Jun Young Park, and Bum Seog Choi. Start-up and Self-sustain Test of 500 W Ultra-Micro Gas Turbine Generator. *Journal of Physics: Conference Series*, 476(9):012060, dec 2013.

[18] Michael Branagan, David Griffin, Christopher Goyne, and Alexandrina Untaroiu. Compliant Gas Foil Bearings and Analysis Tools. *Journal of Engineering for Gas Turbines and Power*, 138(5):054001, may 2016.

[19] Kevin Radil, Samuel Howard, and Brian Dykas. The Role of Radial Clearance on the Performance of Foil Air Bearings. *Tribology Transactions*, 45(4):485–490, jan 2002.

[20] Kousuke Isomura, Shuji Tanaka, Shin-ichi Togo, and Masayoshi Esashi. Development of high-speed micro-gas bearings for three-dimensional micro-turbo machines. *Journal of Micromechanics and Microengineering*, 15(9):S222–S227, sep 2005.

[21] Shinji Tanaka, Jürg Schiffmann, and Zoltán Spakovszky. Technical Report Phase III. Technical report, Massachusetts Institute of Technology, Cambridge, 2010.

[22] Andrei Tisarev, Sergey Falaleev, Christian Koch, Matthias Nagorski, and Stephan Staudacher. Natural Cooling Affecting the Restart of Micro Gas Turbine. In *Volume 8: Microturbines, Turbochargers and Small Turbomachines; Steam Turbines*, page V008T23A019. American Society of Mechanical Engineers, jun 2016.

[23] Yoji Okita. Transient Thermal and Flow Field in a Turbine Disk Rotor-Stator System. In *Volume 3: Heat Transfer, Parts A and B*, volume 2006, pages 1271–1282. ASMEDC, jan 2006.

[24] D Brillert, H J Dohmen, F.-K. Benra, O Schneider, and A V Mirzamoghadam. Application of Conjugate CFD to the Internal Cooling Air Flow System of Gas Turbines. In *Volume 5: Turbo Expo 2003, Parts A and B*, volume 2003, pages 1051–1060. ASMEDC, jan 2003.

[25] A Montenay, L. Paté, and J. M. Duboué. Conjugate Heat Transfer Analysis of an Engine Internal Cavity. In *Volume 3: Heat Transfer; Electric Power; Industrial and Cogeneration*, number C, page V003T01A086. ASME, may 2000.

[26] T. Verstraete, Z. Alsalihi, and R. A. Van den Braembussche. Numerical Study of the Heat Transfer in Micro Gas Turbines. *Journal of Turbomachinery*, 129(4):835–841, oct 2007.

[27] N. V. Suryanarayana. Transient Response of Straight Fins. *Journal of Heat Transfer*, 97(2):417–423, aug 1975.

[28] Craig A. Steeves, Sergio L. dos Santos e Lucato, Ming He, Emilio Antinucci, John W. Hutchinson, and Anthony G. Evans. Concepts for structurally robust materials that combine low thermal expansion with high stiffness. *Journal of the Mechanics and Physics of Solids*, 55(9):1803–1822, sep 2007.

[29] Jonathan Berger, Chris Mercer, Robert M. McMeeking, and Anthony G. Evans. The Design of Bonded Bimaterial Lattices that Combine Low Thermal Expansion with High Stiffness. *Journal of the American Ceramic Society*, 94(SUPPL. 1):s42–s54, jun 2011.